THESIS FOR THE DEGREE OF DOCTOR OF PHILOSOPHY

Runaway-electron model development and validation in tokamaks

MATHIAS HOPPE

Department of Physics
CHALMERS UNIVERSITY OF TECHNOLOGY
Göteborg, Sweden, 2021

Runaway-electron model development and validation in tokamaks
MATHIAS HOPPE
ISBN 978-91-7905-598-1

Doktorsavhandlingar vid Chalmers tekniska högskola
Ny serie nr 5065
ISSN 0346-718X

Department of Physics
Chalmers University of Technology
SE–412 96 Göteborg
Sweden
Telephone +46 (0)31 772 1000

Cover:
Synchrotron radiation pattern from runaway electrons with energy 24 MeV and pitch angle 0.6 rad simulated with SOFT.

Printed in Sweden by
Chalmers Digitaltryck
Chalmers Tekniska Högskola
Göteborg, Sweden, 2021

Runaway-electron model development and validation in tokamaks
MATHIAS HOPPE
Department of Physics
Chalmers University of Technology

Abstract

Magnetic confinement fusion (MCF), in which a hot plasma at more than 100 million kelvin is confined using magnetic fields, is the most successful fusion energy concept developed to date. After decades of research, MCF devices designed to demonstrate a positive net energy output are being constructed, completing a crucial milestone on the path to making fusion a commercially viable energy source. Several hurdles remain on this path, however, and one of the most pressing issues concerns the sudden and rapid loss of confinement of the fusion plasma, known as a disruption. An undesirable consequence of disruptions is the acceleration of a fraction of the plasma electrons to relativistic energies which—if the electrons were to strike the device wall—could deposit a significant portion of the plasma energy on a small area, causing severe and potentially irreparable damage.

The aim of this thesis is to develop a robust simulation tool capable of accurately predicting the number of runaway electrons produced in different disruption scenarios. Since the evolution of the runaway electrons affects the background plasma, it is important to also allow quantities such as electron temperature, ion density, and electric field to evolve self-consistently in the simulation. This leads to a tightly coupled system of non-linear equations, and to solve it we have developed the numerical tool DREAM.

The complexity of the models used to simulate runaway electrons demands that the validity of the models is carefully evaluated by comparing predictions with existing experimental data. One of the most informative techniques for studying the dynamics of runaway electrons in MCF experiments utilises synchrotron radiation, and to facilitate direct comparison of runaway electron simulations with experiments we have developed the synthetic diagnostic framework SOFT. Using SOFT, we study runaway electrons in the ASDEX Upgrade and TCV fusion devices, and develop powerful techniques for accurately extracting information about the location and momentum of runaway electrons.

Keywords: plasma physics, Fokker–Planck equation, magnetic confinement fusion, tokamaks, runaway-electrons, synchrotron radiation

Publications

A M. Hoppe, O. Embréus, R. A. Tinguely, R. S. Granetz, A. Stahl, and T. Fülöp,
SOFT: a synthetic synchrotron diagnostic for runaway electrons,
Nuclear Fusion **58**, 026032 (2018).
`https://doi.org/10.1088/1741-4326/aa9abb`

B M. Hoppe, O. Embréus, C. Paz-Soldan, R. A. Moyer, and T. Fülöp,
Interpretation of runaway electron synchrotron and bremsstrahlung images,
Nuclear Fusion **58**, 082001 (2018).
`https://doi.org/10.1088/1741-4326/aaae15`

C R. A. Tinguely, M. Hoppe, R. S. Granetz, R. T. Mumgaard, and S. Scott,
Experimental and synthetic measurements of polarized synchrotron emission from runaway electrons in Alcator C-Mod,
Nuclear Fusion **59**, 096029 (2019).
`https://doi.org/10.1088/1741-4326/ab2d1d`

D M. Hoppe, G. Papp, T. Wijkamp, A. Perek, J. Decker, B. Duval, O. Embreus, T. Fülöp, U. A. Sheikh, the TCV team, and the EUROfusion MST1 team,
Runaway electron synchrotron radiation in a vertically translated plasma,
Nuclear Fusion **60**, 094002 (2020).
`https://doi.org/10.1088/1741-4326/aba371`

E M. Hoppe, L. Hesslow, O. Embreus, L. Unnerfelt, G. Papp, I. Pusztai, T. Fülöp, O. Lexell, T. Lunt, E. Macusova, P. J. McCarthy, G. Pautasso, G. I. Pokol, G. Por, P. Svensson, the ASDEX Upgrade team, and the EUROfusion MST1 team,
Spatiotemporal analysis of the runaway distribution function from synchrotron images in an ASDEX Upgrade disruption,
Journal of Plasma Physics **87**, 855870102 (2021).
`https://doi.org/10.1017/S002237782000152X`

F I. Svenningsson, O. Embreus, M. Hoppe, S. L. Newton, and T. Fülöp,
Hot-tail runaway seed landscape during the thermal quench in tokamaks,
Physical Review Letters **127**, 035001 (2021).
`https://doi.org/10.1103/PhysRevLett.127.035001`

G M. Hoppe, O. Embreus, and T. Fülöp,
DREAM: A fluid-kinetic framework for tokamak disruption runaway electron simulations,
Computer Physics Communications **268**, 108098 (2021).
`https://doi.org/10.1016/j.cpc.2021.108098`

Related publications, not included in the thesis

H R. A. Tinguely, R. S. Granetz, M. Hoppe, and O. Embréus,
Measurements of runaway electron synchrotron spectra at high magnetic fields in Alcator C-Mod,
Nuclear Fusion **58**, 076019 (2018).
`https://doi.org/10.1088/1741-4326/aac444`

I R. A. Tinguely, R. S. Granetz, M. Hoppe, and O. Embréus,
Spatiotemporal evolution of runaway electrons from synchrotron images in Alcator C-Mod,
Plasma Physics and Controlled Fusion **60**, 124001 (2018).
`https://doi.org/10.1088/1741-4326/aac444`

J L. Hesslow, O. Embréus, M. Hoppe, T. C. DuBois, G. Papp, and T. Fülöp,
Generalized collision operator for fast electrons interacting with partially ionized impurities,
Journal of Plasma Physics **84**, 905840605 (2018).
`https://doi.org/10.1017/S0022377818001113`

K O. Embréus, L. Hesslow, M. Hoppe, G. Papp, K. Richards, and T. Fülöp,
Dynamics of positrons during relativistic electron runaway,
Journal of Plasma Physics **84**, 905840506 (2018).
`https://doi.org/10.1017/S0022377818001010`

L C. Paz-Soldan et al.,
Recent DIII-D advances in runaway electron measurement and model validation,
Nuclear Fusion **59**, 066025 (2019).
`https://doi.org/10.1088/1741-4326/ab1769`

M G. I. Pokol, S. Olasz, B. Erdos, G. Papp, M. Aradi, M. Hoppe, T. Johnson, J. Ferreira, D. Coster, Y. Peysson, J. Decker, P. Strand, D. Yadikin, D. Kalupin, and the EUROfusion-IM Team,
Runaway electron modelling in the self-consistent core European Transport Simulator,
Nuclear Fusion **59**, 076024 (2019).
`https://doi.org/10.1088/1741-4326/ab13da`

N L. Hesslow, L. Unnerfelt, O. Vallhagen, O. Embreus, M. Hoppe, G. Papp, and T. Fülöp,
Evaluation of the Dreicer runaway generation rate in the presence of high-Z impurities using a neural network,
Journal of Plasma Physics **85**, 475850601 (2019).
`https://doi.org/10.1017/S0022377819000874`

O B. Labit et al.,
Dependence on plasma shape and plasma fueling for small edge-localized mode regimes in TCV and ASDEX Upgrade,
Nuclear Fusion **59**, 086020 (2019).
`https://doi.org/10.1088/1741-4326/ab2211`

P S. Coda et al.,
Physics research on the TCV tokamak facility: from conventional to alternative scenarios and beyond,
Nuclear Fusion **59**, 112023 (2019).
`https://doi.org/10.1088/1741-4326/ab25cb`

Q T. A. Wijkamp, A. Perek, J. Decker, B. Duval, M. Hoppe, G. Papp, U. A. Sheikh, I. G. J. Classen, R. J. E. Jaspers, the TCV team, and the EUROfusion MST1 team,
Tomographic reconstruction of the runaway distribution function in TCV using multispectral synchrotron images,
Nuclear Fusion **61**, 046044 (2021).
`https://doi.org/10.1088/1741-4326/abe8af`

R S. Olasz, O. Embreus, M. Hoppe, M. Aradi, D. Por, T. Jonsson, D. Yadikin, G. I. Pokol, and the EU-IM Team,
Validity of models for Dreicer generation of runaway electrons in dynamic scenarios,
Nuclear Fusion **61**, 066010 (2021).
`https://doi.org/10.1088/1741-4326/abf0de`

S E. M. Hollmann, M. Austin, I. Bykov, N. W. Eidietis, O. Embreus, J. L. Herfindal, M. Hoppe, A. Lvovskiy, P. B. Parks, C. Paz-Soldan, D. Shiraki, and I. Svenningsson,
Estimate of pre-thermal quench non-thermal electron density profile during Ar pellet shutdowns of low-density target plasmas in DIII-D,
Physics of Plasmas **28**, 072501 (2021).
`https://doi.org/10.1063/5.0050903`

T R. A. Tinguely, V. A. Izzo, D. T. Garnier, A. Sundström, K. Särkimäki, O. Embreus, T. Fülöp, R. S. Granetz, M. Hoppe, I. Pusztai, and R. Sweeney,
Complete prevention of runaway electron beam formation with a passive 3D coil,
Nuclear Fusion **61**, 124003 (2021).
`https://doi.org/10.1088/1741-4326/ac31d7`

Conference contributions

U M. Hoppe, O. Embréus, A. Tinguely, R. Granetz, A. Stahl, and T. Fülöp,
Synthetic synchrotron diagnostics for runaway electrons,
Proceedings of the 44th EPS Conference on Plasma Physics, Belfast, P5.151 (2017).
`http://ocs.ciemat.es/EPS2017PAP/pdf/P5.151.pdf`

V O. Embréus, K. Richards, G. Papp, L. Hesslow, M. Hoppe, and T. Fülöp,
Dynamics of positrons during relativistic electron runaway,
Proceedings of the 45th EPS Conference on Plasma Physics, Prague, P5.4011 (2018).
`http://ocs.ciemat.es/EPS2018PAP/pdf/P5.4011.pdf`

W M. Hoppe, O. Embréus, P. Svensson, L. Unnerfelt, and T. Fülöp,
Simulations of bremsstrahlung and synchrotron radiation from runaway electrons,
Proceedings of the 45th EPS Conference on Plasma Physics, Prague, O5.J603 (2018).
`http://ocs.ciemat.es/EPS2018PAP/pdf/O5.J603.pdf`

X M. Hoppe, O. Embreus, and T. Fülöp,
DREAM: a fluid-kinetic framework for tokamak disruption runaway electron simulations,
Proceedings of the 47th EPS Conference on Plasma Physics, P3.1041 (2021).
`http://ocs.ciemat.es/EPS2021PAP/pdf/P3.1041.pdf`

Y M. Hoppe, R. A. Tinguely, B. Brandström, O. Embreus, N. C. Hawkes, E. Rachlew, T. Fülöp, and JET contributors,
Polarized synchrotron radiation as a tool for studying runaway electrons,
28th IAEA Fusion Energy Conference, TH/P1-623 (2021).
`https://conferences.iaea.org/event/214/papers/17178/files/6678-hoppe_IAEA2020_8page.pdf`

Statement of contribution

Paper A: I implemented the Soft code, performed the simulations and created all figures. Theory development and simulation analysis was done in close collaboration with O. Embreus. I wrote the manuscript together with the co-authors.

Paper B: I was the main person responsible for simulations and analysis in the paper. I was also responsible for the theory in sections 2.1-2.3. I created all figures. The manuscript was written jointly by me and the other co-authors.

Paper C: I wrote section 3.3, and derived and implemented in Soft the polarization filter model described in that section. I also contributed to the analysis and intepretation of results in the paper.

Paper D: I was responsible for simulations and interpretation of synchrotron radiation patterns. I created all figures. The manuscript was written jointly by me and the other co-authors.

Paper E: I was chiefly responsible for section 2, synchrotron simulations and interpretation of simulation results in section 3. I supervised the student who implemented the inversion algorithm described in section 4.1 and applied in section 4.2, and supervised/contributed to the derivation in appendix A. I also contributed to discussions about and interpretation of Go+Code simulations, and set up and ran the refined simulations ultimately used in the paper. I wrote the manuscript together with the co-authors.

Paper F: I implemented the particle and heat transport models used in the paper. I was also involved in analysis of the simulations.

Paper G: I developed the code Dream together with O. Embreus. I contributed to parts of the theoretical basis of the code described in sections 2, 3 and appendices B and C, and was mainly responsible for the content of sections 4-6 (with major contributions from O. Embreus). I created all figures. The manuscript was written by me and the co-authors.

Acknowledgments

I feel exceptionally fortunate to have pursued my PhD under the supervision of Tünde Fülöp. Not only is Tünde passionate about plasma physics, but she also deeply cares for and nurtures her students in a way which most PhD students can only dream of (as several of them have told me after comparing experiences), building an excellent foundation for our future careers. I am also very grateful to my co-supervisor, István, for always being available to help with physics as well as general life questions.

Although not formally my supervisor, Ola has taken on that role by himself with remarkable dedication. Aside from being a living encyclopedia of runaway electron physics, his patience and passion for physics has made it a true pleasure to work with him.

Working in Tünde's group also means that you get to interact with a number of very interesting people. I am very grateful to have worked with someone as inspiring as Linnea and will always remember our many adventures when travelling to various fusion labs and conferences; to Geri for always helping out with things, be it physics, IT or carrying guitar amplifiers, and for his generous hospitality; and to Sarah for always improving my texts, both by checking my grammars and providing the broader fusion physics perspective.

Thanks go out to my frequent collaborators around the world for their selfless help and warm companionship: Alex Tinguely, Elisabeth Rachlew, Gergő Pokol and Tijs Wijkamp. Special thanks also go to Joan Decker and Yves Peysson for our many interesting physics discussions and for sharing their vast knowledge about the bounce average.

Finally, I would like to thank all members of the Plasma Theory group—past and present—for contributing to the very warm and nurturing environment which has allowed me to complete this thesis.

Mathias Hoppe, Göteborg, December 2021

Contents

Abstract iii

Publications v

Acknowledgements xii

1 Introduction 1

2 Bounce-averaged Fokker–Planck theory 7
- 2.1 Particle motion in tokamaks 8
- 2.2 Collisions and the Fokker–Planck equation 11
  - 2.2.1 Fokker–Planck equation 12
  - 2.2.2 Phase-space coordinates for tokamak plasmas . . . 13
- 2.3 Bounce averaging 16
  - 2.3.1 Gyro average 17
  - 2.3.2 Poloidal angle average 18
  - 2.3.3 Validity of bounce average in tokamak disruptions 24

3 Theory of runaway electrons 27
- 3.1 Criteria for runaway 28
- 3.2 Tokamak disruptions 31
  - 3.2.1 Runaway generation mechanisms 34
  - 3.2.2 Runaway electron losses 39
- 3.3 Electron kinetics in the plateau phase 41

4 Radiation from runaway electrons 45
- 4.1 Radiation diagnostic integral 47
  - 4.1.1 Tokamak geometry 48
- 4.2 Cone approximation 49
- 4.3 Properties of the radiation integral 53

4.3.1 Dominant particles 54
4.4 Radiation spot shape taxonomy 56
4.4.1 Magnetic field and detector placement 59
4.4.2 Runaway electron properties 61

5 Concluding remarks **69**
5.1 Summary of papers 70
5.2 Outlook 74

References **77**

Included papers A–G **93**

Chapter 1

Introduction

The threat of global climate change is making itself more apparent by the day at the same time as continued economic development and industrialisation increases the world's demand for energy [1, 2]. It is clear that the use of fossil fuels must be drastically reduced over the coming years, but the debate remains open regarding which energy sources to replace them with. Renewable energy sources, such as wind and solar power, are able to produce electricity with minimal greenhouse gas emissions, but their inherent dependence on local weather conditions could lead to an unreliable supply of electricity on the grid [3, 4]. A more predictable energy source is nuclear fission, which minimises the emission of greenhouse gases while also providing the most energy per unit area of all the energy sources today. Concerns have however been raised about the safety of nuclear fission, both in terms of accidents, which could spread highly radioactive material over large areas, and the long-lived radioactive waste resulting from fission.

A technology which has the potential to offer both the reliability and energy density of fission, while being free from greenhouse gas emissions and only produces some intermediate level waste, is *nuclear fusion* [5]. Fusion combines two atomic nuclei into one heavier nucleus, releasing a significant amount of energy in the process, and it is the mechanism which powers all the stars of the universe. To achieve fusion on earth, temperatures of more than 200 million kelvin and pressures of around ten atmospheres must be attained. The currently most promising technology for achieving fusion on earth is *magnetic confinement fusion*, whereby a hot ionised gas known as a *plasma* is held in place in a toroidal shape using strong magnetic fields of several teslas. Of the magnetic confine-

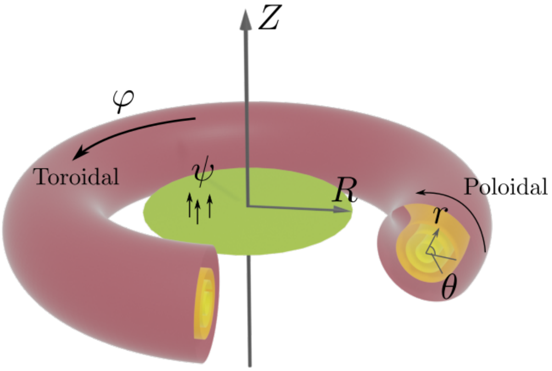

Figure 1.1: An illustration of a tokamak geometry with nested flux surfaces (coloured inside torus). The green circle indicates the surface over which to integrate to obtain the poloidal magnetic flux ψ at any given distance R from the symmetry axis. The three coordinates used in this thesis are also indicated: minor radius r, poloidal angle θ, and toroidal angle φ.

ment fusion devices currently being researched, the *tokamak* has achieved both the highest energy and power output to date [6]. The major international fusion device ITER, which is currently under construction in Cadarache, France, is a tokamak and aims to prove the feasibility of fusion power as a large-scale source of energy [7, 8].

To successfully confine particles inside the fusion device, the magnetic field must be twisted. In the tokamak, this is achieved by driving a strong current of several mega-amperes through the plasma. The magnetic field generated from the plasma current is in the poloidal direction, as shown in figure 1.1, perpendicular to that generated by the external coils and thus gives the total magnetic field a helical structure. Although the plasma current is essential for providing adequate confinement of the fusion fuel, as we shall see, it also comes with some risks.

On rare occasions, plasma instabilities may be triggered which spiral out of control and cause the plasma to lose much of its thermal energy in less than a millisecond [9], in an event known as a *disruption*. Much of the heat may be lost through radiation emission, but a significant portion of the heat may also be deposited on the plasma facing components of the tokamak wall. As the plasma cools down, its conductivity falls, and the plasma current is forced to decrease, which will both induce currents in the tokamak wall leading to strong structural forces acting on the device [10], as well as an electric field in the plasma. If this electric field is sufficiently strong, it may accelerate a fraction of the electron population to relativistic energies which—if they were to strike the wall—may cause significant localised and deep burn damage to the plasma facing components. This would both be costly to repair and, more importantly, require extended shutdown of the device [11].

The acceleration of electrons to relativistic energies is made possible by a plasma phenomenon known as *electron runaway* [12]. It can be shown that the friction force experienced by a fast electron due to collisions with other particles in a plasma is approximately proportional to the inverse of its velocity squared. Thus, if the electron was to also experience an accelerating force, such as from an electric field induced during a tokamak disruption, the net acceleration of the electron would increase the faster it travels, causing the electron to "run away" until radiation losses balance the acceleration, usually at energies on the order of tens of MeV. What makes the production of runaway electrons in tokamak disruptions all the more concerning is the fact that collisions allow runaway electrons to multiply exponentially once a few electrons have become runaways [13]. This mechanism, known as *avalanche multiplication*, is exponentially sensitive to the plasma current of the tokamak, and will therefore be able to multiply the number of runaway electrons by an astounding factor of 10^{20} in ITER [14], assuming all losses of runaways are neglected.

In ITER, the first line of defence against disruptions will be to actively control the plasma in such a way as to avoid them [15]. By using algorithms which are able to give warnings ahead of time when the plasma is about to disrupt, plasma steering should be able to prevent most disruptions [16]. Disruption avoidance will not be guaranteed to work in all situations, and so a system for mitigating the effects of a disruption is also under development, which could be triggered by the disruption prediction algorithms. The system involves firing pellets of hydrogen isotopes and noble gases, such as neon, into the plasma in order to prematurely trigger or mitigate the disruption and uniformly radiate away as much of the plasma energy as possible [15]. Allowing a natural disruption to proceed without mitigation could lead to excessive energy losses via radial transport onto the plasma facing components, as well as large currents being induced in the wall and giving rise to devastating structural forces. The injection of pellets into the plasma can also affect the generation and survival of runaway electrons [17]. Initially, the high charge of the injected noble gas was expected to provide increased collisional friction and thereby quickly suppress the production of runaway electrons [15]. Later studies have however nuanced this view and even predict that the use of heavy atoms may result in enhanced avalanche multiplication [18].

If the injection of heavy atoms in the plasma is not sufficient to mitigate the runaway electrons, other suppression mechanisms are required. One such mechanism which provides an attractive route to runaway suppression is radial transport of fast electrons. This transport is caused by magnetic perturbations in the plasma which gradually deposit the relativistic electrons on the plasma facing components at a slow enough rate and with a broad enough distribution as to avoid excessive heat loads. A method to induce such perturbations is using active, so called resonant magnetic perturbation (RMP), coils [19]. While initially successful in mitigating runaway electrons in smaller devices, it is now generally believed that the perturbations produced by RMP coils will not be able to penetrate deep enough into the plasmas of larger tokamaks to have sufficient effect on the runaways [20, 21]. An alternative to the active RMP coils—which have to be activated in time for runaways to be mitigated—is to use passive coils [22], as has been proposed as a mitigation method for the compact SPARC tokamak, currently under development [23]. The passive coils were predicted in Paper T to provide full suppression of the runaway electrons in SPARC. Yet another method to cause radial transport of runaway electrons, which is predicted to be effective also in larger tokamaks, is to trigger an instability which benignly expels the electrons [24].

More advanced pellet injection schemes have also been proposed to provide robust suppression of runaway electrons. In Refs. [17, 25], a two-stage injection scheme was considered theoretically in which the temperature is first decreased by diluting the plasma with an injection of only deuterium without causing the plasma to become unstable. This is followed by a secondary injection of neon to trigger the final thermal collapse. The first injection could prevent the survival of fast electrons, minimising the number of runaway electrons available for avalanche multiplication.

In today's tokamaks, runaway electrons are not of great concern as their plasma currents are not sufficiently large to give appreciable avalanche multiplication. However, in the next generation reactor scale tokamaks which are currently being designed and built, the avalanche multiplication factor is expected to be orders of magnitude larger. This gap in avalanche multiplication factor between current and future experiments means that it is not possible to fully verify the robustness of any runaway mitigation scheme before a reactor scale device is available. If the mitigation system turns out not to be effective, however, even a single disruption could be sufficient to cause devastating damage and take the device out of operation for an unacceptably long time. It is therefore crucial that the mitigation techniques are carefully evaluated using theoretical models prior to commissioning. Further, it is important that the models used have been validated against existing experiments to ensure that they accurately represent reality. This thesis considers both model development and validation in order to contribute to robust runaway electron mitigation schemes for future tokamaks.

Reliable runaway electron model validation requires the comparison of as many physical observables as possible with experimental measurements. A problem during tokamak disruptions is however that detailed experimental measurements can be incredibly difficult. While the theoretical models can give detailed information about the motion of particles, it is often difficult to obtain measurements other than spatially and/or temporally integrated observables, such as the total plasma current (rather than current density profile) or the total number of heavy atoms injected in the plasma (rather than the density profile of such atoms after injection). The large variation in plasma parameter values occurring during disruptions further complicates measurements, as some diagnostics are designed to operate in certain parameter regimes only or do not have the time resolution required.

Radiation diagnostics, which measure electromagnetic radiation emitted by runaway electrons, stand out from other diagnostics by being able to provide detailed information about both the position and momentum of the electrons. Any charged particle will emit electromagnetic radiation when accelerated [26], and in a tokamak plasma, runaway electrons emit radiation primarily due to two types of acceleration. The first type of acceleration comes from the circular motion that all charged particles execute around magnetic field lines, and the corresponding radiation is referred to as *cyclotron emission* or, if the particle is moving at relativistic speeds, as *synchrotron emission*. The second type of acceleration results from collisions with other particles and is called *bremsstrahlung*. At relativistic particle speeds, both types of radiation are emitted primarily along the velocity vector of the particle. As such, if an observer detects radiation from the relativistic particle, they can conclude that the particle must be travelling directly towards them. Since the origin of the radiation and its intensity provide information about the location and energy of the particle, this means that bremsstrahlung and synchrotron radiation can, in principle, be used to extract information about the three main parameters for runaway electrons: their position, energy and direction of motion.

In this thesis we present the two numerical frameworks DREAM (for *Disruption Runaway Electron Analysis Model*) and SOFT (for *Synchrotron-detecting Orbit Following Toolkit*), which can be used to run simulations both of how runaway electrons are generated and evolve, as well as of what signals they should give rise to in bremsstrahlung and synchrotron radiation detectors. We begin in chapter 2 by describing the motion of charged particles in tokamak magnetic fields and how it can be represented mathematically. The highlight of the chapter is the derivation of the bounce-averaged Fokker–Planck equation, on which the DREAM code is based, as are many other runaway electron and plasma transport models. In chapter 3, we turn our attention to runaway electrons and review in detail the various physical mechanisms by which they are generated and lost. The chapter ends with a description of the runaway dynamics in the later stages of a tokamak disruption, which is usually better diagnosed than the earlier stages. Chapter 4 first reviews the theory underlying synthetic radiation diagnostics within the framework established earlier in the thesis and then proceeds with summarising the key properties of solutions to the radiation diagnostic integral. The appended papers are summarised in chapter 5, and the current state of the research topic, along with its future prospects, are discussed.

Chapter 2

Bounce-averaged Fokker–Planck theory

Plasmas are complex physical systems that can exhibit a wide range of phenomena under different circumstances. It should therefore be no surprise that no single physical model can be efficiently applied to study all imaginable properties observed in plasmas—the more comprehensive models tend to be both analytically and computationally intractable for certain phenomena, while the simpler models utilise approximations which neglect details important to other phenomena. One of the most fundamental equations in plasma theory is the kinetic equation which governs the evolution of any plasma and, if solved, provides information about the plasma in remarkable detail. Solving the kinetic equation in its full glory for a tokamak is however a profoundly difficult task.

To make the kinetic equation more manageable, one can average it over time scales which are short compared to the time scales on which the dynamics of interest play out. One particular such averaging formalism is the *bounce-average*, which assumes that the collisional time scale is slower than the time scale for a particle to transit the tokamak and return to the same poloidal angle, allowing averages over the periodic motion to be carried out, effectively halving the dimensionality of the problem. The bounce-average was first developed by Soviet scientists in the 1950s, and numerical solvers utilising the technique were first introduced in the 1970s, in order to study radio frequency heating and current drive in magnetic mirror machines [27–29]. Towards the end of the decade the technique had been adapted for tokamaks [30] and can today be found in a number of different codes which study the dynamics of low-collisionality plasma populations, such as CQL3D [31] or LUKE [32].

In this thesis, the bounce-averaging theory plays an important role in Paper G, where a solver of the bounce-averaged Fokker–Planck equation is developed as part of the tokamak disruption simulation framework DREAM. To complete the presentation given in Paper G, we will in this chapter review the background theory and derive the main results. However, before outlining the bounce-average framework, we will briefly introduce the reader to a number of concepts central to kinetic theory for tokamaks.

2.1 Particle motion in tokamaks

A tokamak is a toroidal device which confines plasma using magnetic fields. An externally generated *toroidal* magnetic field generates the familiar torus shape, while a *poloidal* magnetic field, produced by an electrical current running through the plasma, twists the magnetic field to counteract loss of particles due to drifts in the non-uniform toroidal magnetic field. The twist of the magnetic field causes magnetic field lines to envelop torus-shaped surfaces as in figure 1.1, and these surfaces are conveniently labelled using a magnetic flux. In this thesis we will use the poloidal magnetic flux ψ, defined as the magnetic flux through the green horizontal circle in figure 1.1, to label such surfaces, commonly referred to as *flux surfaces.*

The tokamak magnetic field affects the motion of the charged particles comprising the plasma via the Lorentz force

$$\boldsymbol{F} = q\left(\boldsymbol{E} + \boldsymbol{v}\times\boldsymbol{B}\right), \tag{2.1}$$

where q is the particle charge, $\boldsymbol{v}$ is the particle velocity, $\boldsymbol{E}$ is the electric field and $\boldsymbol{B}$ is the magnetic field. This force guides the particles into helical orbits around the magnetic field lines, which in turn wrap around the torus as illustrated in figure 2.1. The circular motion around magnetic field lines has an angular frequency $\Omega = qB/\gamma m$ and radius $r_\mathrm{L} = v_\perp/\Omega = p_\perp/qB$, known as the cyclotron frequency and Larmor radius respectively, with m the mass of the particle, $\gamma = 1/\sqrt{1-|\boldsymbol{v}|^2/c^2}$ the relativistic factor, $v_\perp$ the speed perpendicular to $\boldsymbol{B}$, and $p_\perp = \gamma m v_\perp$. The toroidal geometry causes the magnetic field to be stronger closer to the centre of the torus, which has important implications for the charged particle orbits.

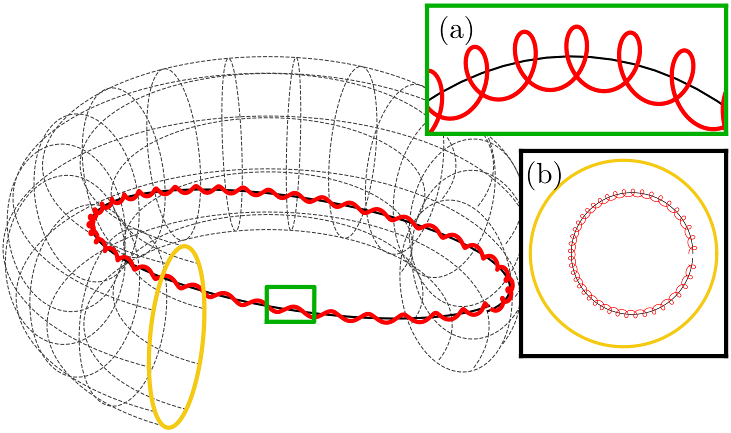

Figure 2.1: Charged particles follow helical orbits in a tokamak magnetic field. The twisted magnetic field lines cause the particle to traverse the device both toroidally and poloidally. (a) Magnification of the orbit, revealing the helical motion around magnetic field lines. (b) Orbit projected into a poloidal plane, emphasising the poloidal motion of the particle.

It can be shown that the magnetic moment $\mu \equiv p_\perp^2/2mB$ of a charged particle is an adiabatic invariant [33], which changes only slightly during the course of many transits by the particle along its orbit and can practically be taken as a constant of motion. If the kinetic energy of the particle is conserved, the following relation holds (for simplicity taken in the non-relativistic limit):

$$W_{\mathrm{kin}} = \frac{mv_\parallel^2}{2} + \mu B = \mathrm{const.} \tag{2.2}$$

When a particle travels from the outside of the tokamak to the inside along its orbit, as in figure 2.1, the magnetic field strength increases. As μ cannot change, the conservation of energy forces $v_\parallel$ to decrease. If a particle starts with initial speeds $v_\parallel = v_{\parallel,0}$ and $v_\perp = v_{\perp,0}$ at a point with a magnetic field strength $B = B_0$, equation (2.2) implies that $v_\parallel$ will eventually be depleted if

$$\frac{v_{\perp,0}^2}{v_{\parallel,0}^2 + v_{\perp,0}^2} \geq \frac{B_0}{B_{\mathrm{max}}}, \tag{2.3}$$

with B_{max} denoting the maximum magnetic field strength experienced by the particle along its orbit. If this happens, $v_\parallel$ is forced to change sign,

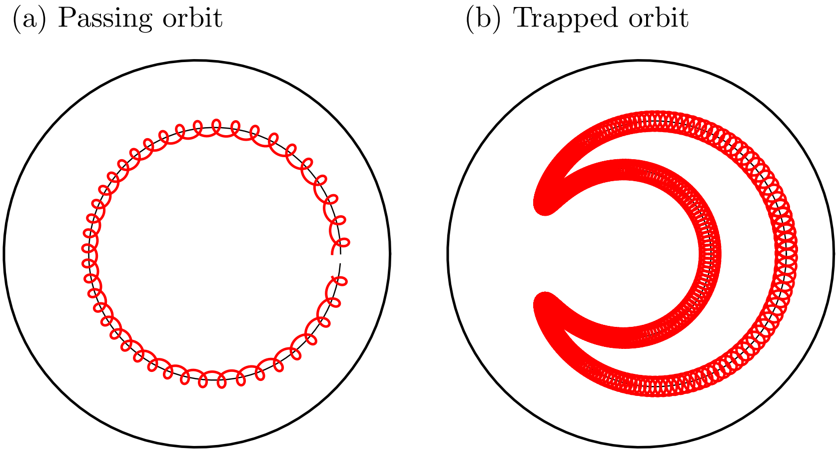

Figure 2.2: Particle orbits projected onto a poloidal cross section. (a) Passing (or circulating) orbit, in which the particle can move unobstructed through the magnetic field. (b) Trapped orbit, where the particle is eventually forced to bounce back when the magnetic field becomes too strong, as a result of the adiabatic invariance of the magnetic moment.

causing the particle to bounce and travel back in the opposite direction. This leads to an orbit which, when projected onto a poloidal cross-section, takes the shape of a banana, as shown in figure 2.2b. Such orbits are referred to as *trapped orbits* (or less formally as banana orbits in tokamaks) since the particle is effectively trapped between two poloidal angles in the magnetic field, forced to bounce back and forth. Particles which start with smaller ratios $v_{\perp,0}/v_{\|,0}$ will be able to complete an orbit without turning around and instead follow *passing* or *circulating* orbits, shown in a poloidal cross-section in figure 2.2a. Later, when developing the bounce-average in section 2.3 we will need to pay special attention to which of these two types of orbits a particle is following.

Although the Lorentz force (2.1) locally confines a particle to the vicinity of a magnetic field line, inhomogeneities in the magnetic field and perpendicular forces will lead the particle to gradually deviate from the path designated by the field line. Such gradual deviations are called *drifts* and they arise in a number of situations. For tokamak plasmas, two of the most important drifts are curvature and ∇B drifts. The curvature drift arises since a particle moving along a curved magnetic field line experiences a centrifugal force $\boldsymbol{F}_{\mathrm{c}} = mv_{\parallel}^2\boldsymbol{R}_{\mathrm{c}}/R_{\mathrm{c}}$, where $\boldsymbol{R}_{\mathrm{c}}$ denotes the radius of curvature of the field line. The resulting drift velocity will be perpendicular to this force, and to the magnetic field:

$$\boldsymbol{v}_{\mathrm{curv}} = mv_{\parallel}^2\frac{\boldsymbol{R}_{\mathrm{c}}\times\boldsymbol{B}}{qR_{\mathrm{c}}^2B^2}. \tag{2.4}$$

The ∇B drift arises, as the name suggests, from variations in the magnetic field strength, and introduces a drift velocity

$$\boldsymbol{v}_{\nabla\mathrm{B}} = \operatorname{sgn} q\frac{v_{\perp}r_{\mathrm{L}}}{2}\frac{\boldsymbol{B}\times\nabla B}{B^2}, \tag{2.5}$$

where $\operatorname{sgn} q$ denotes the sign of the particle charge.

To counteract drifts and keep particles confined in the magnetic field, tokamaks have a poloidal magnetic field component which twists the field lines and causes the particles to circulate poloidally, in addition to their toroidal circulation. Since the direction of the curvature and ∇B drifts are roughly the same in all points of the tokamak (nearly vertical), the poloidal circulation causes the particle to drift an equal distance into and out from the centre of the plasma during a poloidal transit. This effectively cancels the net displacement from the magnetic flux surface caused by the drifts and keeps the particles confined.

The curvature and ∇B drifts just described are responsible for giving the banana its width in figure 2.2. On one side of the orbit, the particle will drift either in towards or out from the centre of the plasma, and then in the opposite direction after bouncing. Often in magnetic confinement fusion devices the particle drifts are small compared to the typical length scales of the system, allowing us to simplify our calculations by neglecting them, as will be done in the next section.

2.2 Collisions and the Fokker–Planck equation

The magnetic field of a tokamak is essential for confining charged particles and preventing them from being lost to the walls, however it is far from the only force influencing the particle motion. As for any plasma, inter-particle collisions and electric fields play important roles in the particle dynamics. Due to the large number of particles present in a tokamak, it is not possible to solve the equations of motion for each individual particle separately, especially as these must be coupled to Maxwell's equations in order to determine the electric and magnetic fields generated by each particle. Instead, the plasma can be studied from the perspective of statistical physics, in which the individual particles of a given species are replaced with a continuous *distribution function*, here denoted $f(\boldsymbol{x}, \boldsymbol{p})$, representing the density of particles in the phase space constituted by the position and momentum coordinates $\boldsymbol{x}$ and $\boldsymbol{p}$. In this thesis we normalise the distribution function such that

$$N = \int f(\boldsymbol{x}, \boldsymbol{p})\,\mathrm{d}\boldsymbol{x}\mathrm{d}\boldsymbol{p}, \tag{2.6}$$

is the total number of particles in the system.

2.2.1 Fokker–Planck equation

The distribution function of any plasma satisfies the Liouville equation [34, 35]

$$\frac{\mathrm{d}f}{\mathrm{d}t} \equiv \frac{\partial f}{\partial t} + \dot{\boldsymbol{x}} \cdot \frac{\partial f}{\partial \boldsymbol{x}} + \dot{\boldsymbol{p}} \cdot \frac{\partial f}{\partial \boldsymbol{p}} = 0, \tag{2.7}$$

with $\dot{\boldsymbol{x}} \equiv \mathrm{d}\boldsymbol{x}/\mathrm{d}t$ and $\dot{\boldsymbol{p}} \equiv \mathrm{d}\boldsymbol{p}/\mathrm{d}t$. The Liouville equation is a fundamental equation in statistical physics which states that in a closed system without external sources, the distribution function remains constant along trajectories in phase space.

In a plasma, the force $\dot{\boldsymbol{p}}$ acting on particles is the Lorentz force (2.1). It is important to note that the electric and magnetic fields included in this force are comprised of both (macroscopic) fields governing the collective behaviour of the particles, as well as (microscopic) fields generated by the charged particles themselves. By separating the macroscopic from the microscopic fields, and gathering the latter into an operator $C[f]$, we obtain the kinetic equation

$$\frac{\partial f}{\partial t} + \dot{\boldsymbol{x}} \cdot \frac{\partial f}{\partial \boldsymbol{x}} + q\left(\boldsymbol{E} + \boldsymbol{v} \times \boldsymbol{B}\right) \cdot \frac{\partial f}{\partial \boldsymbol{p}} = C\left[f\right]. \tag{2.8}$$

The operator $C[f]$, which represents the effect of Coulomb interactions between particles, i.e. collisions, is known as the *collision operator*. The direct evaluation of $C[f]$ from the microscopic fields generated by all particles is in most cases intractable, and instead various approximate models for the collision operator are used. In this thesis we use a Fokker–Planck collision operator, which is derived under the assumption that collisions are dominated by long range Coulomb interactions, so that the momentum transfer in each collision is small. The collision operator can then be written in an advection-diffusion form,

$$C[f] = \frac{\partial}{\partial \boldsymbol{p}} \cdot \left[-\boldsymbol{A} f + \mathbb{D} \cdot \frac{\partial f}{\partial \boldsymbol{p}} \right], \tag{2.9}$$

where the dynamical friction coefficient $\boldsymbol{A} = \sum_j \boldsymbol{A}_{ij}$ and diffusion coefficient $\mathbb{D} = \sum_j \mathbb{D}_{ij}$ are given by [36, 37]

$$\begin{aligned} \boldsymbol{A}_{ij}\left(\boldsymbol{x}, \boldsymbol{p}\right) &= -\frac{q_i^2 q_j^2}{8\pi\varepsilon_0^2 m_i m_j} \ln\Lambda_{ij} \int f_j\left(\boldsymbol{x}, \boldsymbol{p}'\right) \frac{\partial}{\partial \boldsymbol{p}'} \cdot \mathbb{U}\left(\boldsymbol{p}, \boldsymbol{p}'\right)\, \mathrm{d}\boldsymbol{p}', \\ \mathbb{D}_{ij}\left(\boldsymbol{x}, \boldsymbol{p}\right) &= \frac{q_i^2 q_j^2}{8\pi\varepsilon_0^2 m_i^2} \ln\Lambda_{ij} \int f_j\left(\boldsymbol{x}, \boldsymbol{p}'\right) \mathbb{U}\left(\boldsymbol{p}, \boldsymbol{p}'\right)\, \mathrm{d}\boldsymbol{p}'. \end{aligned} \tag{2.10}$$

Here, indices denote the particle species (ij is for a particle of species i colliding with particles of species j), ε_0 the permittivity of free space, and $\ln\Lambda_{ij}$ is the Coulomb logarithm for collisions between species i and j [38]. The integration kernel $\mathbb{U}(\boldsymbol{p}, \boldsymbol{p}')$ is a matrix which in the relativistic case is given by

$$\mathbb{U}\left(\boldsymbol{p}, \boldsymbol{p}'\right) = \frac{r^2/\gamma\gamma'}{\left(r^2-1\right)^{3/2}} \left[m^2c^2\left(r^2-1\right)\mathbb{I} - \boldsymbol{p}\boldsymbol{p} - \boldsymbol{p}'\boldsymbol{p}' + r\left(\boldsymbol{p}\boldsymbol{p}' + \boldsymbol{p}'\boldsymbol{p}\right) \right], \tag{2.11}$$

where $\mathbb{I}$ is the identity matrix, $r = \gamma\gamma' - \boldsymbol{p}\cdot\boldsymbol{p}'/m^2c^2$, $\gamma = \sqrt{1 + \boldsymbol{p}\cdot\boldsymbol{p}/m^2c^2}$, and $\gamma' = \sqrt{1 + \boldsymbol{p}'\cdot\boldsymbol{p}'/m^2c^2}$. The form (2.10) of the collision coefficients is known as the (relativistic) Landau form. Due to the appearance of integrals over the distribution function, this particular formulation is difficult to work with numerically. In order to solve the Fokker–Planck equation numerically, it is instead more common to express the collision coefficients in terms of a set of potential functions, each satisfying a Poisson-type differential equation [37, 39]. The various collision operators implemented in the DREAM code, described in Paper G, are all based on the linearised coefficients derived by Pike and Rose [40], which are in turn based on the non-linear differential formulation of the collision coefficients given by Braams and Karney [37].

2.2.2 Phase-space coordinates for tokamak plasmas

The key to efficiently solving equation sets describing complex systems is to select an appropriate set of phase space coordinates which reveal any underlying symmetries and enable simplifications and approximations.

For the Fokker–Planck equation in a tokamak, a number of coordinate sets may be suitable depending on which approximations are made. In what follows here we will introduce the set of coordinates used in the DREAM code, described in Paper G, which is similar and for the most part equivalent to that used in the SOFT code, described in Paper A. For brevity, we will here only mention the approximations used as the coordinates are introduced and leave the motivation and details of the approximations for section 2.3.

A desired quality of the set of coordinates to use for the tokamak plasma is that they allow us to succinctly describe the motion of particles. We should therefore select a set of coordinates which parameterise particle orbits. In the next section we will neglect orbit drifts and assume that the Larmor radius is small, implying that the same set of spatial coordinates which parameterise the particle orbits will also parameterise magnetic field lines. Since the archetypal tokamak magnetic field takes the shape of a circular cross-section torus, a set of toroidal coordinates consisting of a minor radius, poloidal and toroidal angle may be suitable. Modern tokamaks however usually have advanced capabilities for shaping the poloidal cross section of the magnetic field, requiring us to define our coordinates with some care.

For configuration space, we can use the poloidal magnetic flux ψ, poloidal angle θ and toroidal angle φ as coordinates. Since, in our approximation, particles follow magnetic field lines exactly, they move on surfaces of constant ψ, meaning that ψ is a constant of motion. The position along the flux surface in the poloidal plane is labelled with the poloidal angle θ, which is defined as the angle in the poloidal plane between the outer midplane and the particle position, with the origin at the magnetic axis. This is the definition used for numerically provided magnetic fields in DREAM. The toroidal angle is the angle between some reference position in the tokamak and the position of the particle, in the toroidal direction. Figure 2.3a indicates the definition of the configuration space coordinates.

In momentum space, it is convenient to use a spherical coordinate system, which separates the magnitude and direction of the momentum. By aligning the z axis of the coordinate system locally with the magnetic field, we can introduce the magnitude $p = |\boldsymbol{p}|$, the pitch $\xi = \boldsymbol{p}\cdot\boldsymbol{B}/(pB)$ and the azimuthal angle ζ. Alternatively, we could replace p and ξ with the momentum components $p_\parallel = p\xi$ and $p_\perp = p\sqrt{1-\xi^2}$, parallel and perpendicular to the magnetic field, respectively. Both these coordi-

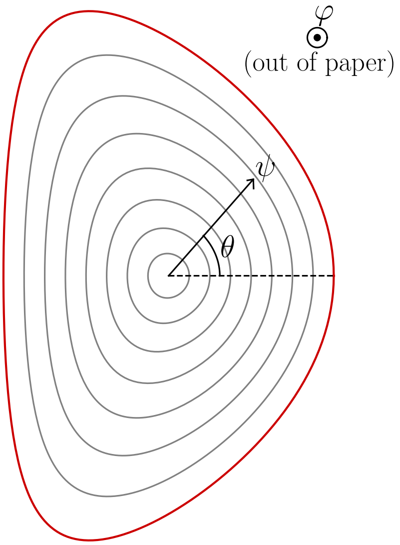

Figure 2.3: Illustration of the three configuration space coordinates in a shaped tokamak magnetic geometry. Any point in the plasma is parameterised by the poloidal magnetic flux ψ, the poloidal angle θ and the toroidal angle φ (directed out of the paper).

nate systems have one disadvantage though: as described in section 2.1, because of the adiabatic invariance of the magnetic moment, the pitch varies along the orbit. It would be more desirable to associate the orbit with a single set of momentum space coordinates which uniquely identifies it. One possibility is to replace ξ with the adiabatic invariant μ, but in DREAM (and SOFT) we instead opt for using the value of the pitch ξ at a clearly defined point along the orbit, and denote the pitch at this point by ξ_0. The point chosen is that at which the magnetic field attains its minimum value along the orbit, B_{min}, as this is the only point which allows us to sample all possible orbits. If we were to instead choose to give ξ_0 at a point with $B = B_0 > B_{\text{min}}$, then our phase space parameterisation would not allow us to describe those particles with $|\xi| < \sqrt{1 - B_{\text{min}}/B_0}$ when at B_{min}, which due to the trapping effect will bounce back before reaching the reference point.

2.3 Bounce averaging

Our goal in this section is to derive a Fokker–Planck equation which can describe the evolution of a distribution function due to collisions in a typical tokamak plasma (exactly what “typical” means in this context will be clarified shortly). It is important for the equation to account for the geometry of the tokamak, not least the bounce motion executed by trapped particles. In addition to these qualities, we would also like the equation to be as simple as possible to solve numerically, in practice meaning that it should be as far reduced in dimensionality as possible. Our procedure will follow that of Killeen *et al.* [29].

To begin with, let us order the various time and length scales of the system. In symbols, we assume for the time scales that

$$\tau_\Omega \ll \tau_\mathrm{b} \ll \tau_\mathrm{c}, \tau_\mathrm{acc}, \tau_\mathrm{rad}. \tag{2.12}$$

The fastest time scale that we will be concerned with is the gyration time scale $\tau_\Omega = \Omega^{-1}$, where $\Omega = qB/\gamma m$ is the cyclotron frequency, corresponding to the time it takes for a charged particle to circle a magnetic field line. We assume that this time scale is much faster than the *transit* or *bounce* time scale τ_b, which is the time it takes for a particle to complete a poloidal transit of its orbit and return to its starting point in the poloidal plane,

$$\tau_\mathrm{b} = \oint \frac{\mathrm{d}s}{v_\parallel}, \tag{2.13}$$

where the path integral is taken over the particle orbit. This time scale is in turn assumed to be much faster than the collision, acceleration and energy loss (via radiation) time scales τ_c, τ_acc and τ_rad respectively. This ensures that the energy of a particle is approximately constant during the orbit and allows us to associate each orbit with exactly one set of momentum coordinates.

For the length scales, we will work in the so-called zero orbit width (ZOW) limit, where the Larmor radius and the orbit width due to the magnetic drifts are much smaller than the length scale over which the magnetic field varies significantly,

$$r_\mathrm{L}, \rho_\mathrm{drift} \ll \frac{B}{|\nabla B|}, \tag{2.14}$$

where ρ_drift denotes the gyro averaged distance by which the particle deviates from the flux surface. In practice, this means that particles will follow a single field line throughout their orbit, so that the “banana” orbit illustrated in figure 2.2 loses its width and the particle bounces back and forth along the same path. The smallness of the Larmor radius r_{L} also implies that the particle does not experience any field variation during a gyration around the magnetic field line which, as we shall see, makes f isotropic in the gyro angle ζ.

2.3.1 Gyro average

Starting from the Fokker–Planck equation (2.8), which can also be written

$$\frac{\partial f}{\partial t}+\dot{\boldsymbol{x}}\cdot\frac{\partial f}{\partial \boldsymbol{x}}+\dot{p}\frac{\partial f}{\partial p}+\dot{\xi}\frac{\partial f}{\partial \xi}+\dot{\zeta}\frac{\partial f}{\partial \zeta}=C\left[f\right], \tag{2.15}$$

we will successively average over the fastest time scales of the system. As assumed in (2.12), the fastest is the time it takes for a particle to travel 2π radians in the gyro angle ζ. We therefore proceed with an asymptotic expansion of the distribution function in the small parameter ϵ_Ω which corresponds to the ratio of the gyro to the transit time scale:

$$f=\tilde{f}_0+\tilde{f}_1+\dots \tag{2.16}$$

where subsequent terms are smaller by a factor of ϵ_Ω. By substituting equation (2.16) into the Fokker–Planck equation (2.15) and matching the orders in ϵ_Ω, we first find that to lowest order

$$\dot{\zeta}\frac{\partial \tilde{f}_0}{\partial \zeta}=0, \tag{2.17a}$$

implying that $\tilde{f}_0$ is independent of the gyro angle ζ. In the next order, we obtain

$$\frac{\partial \tilde{f}_0}{\partial t}+\dot{\boldsymbol{x}}\cdot\frac{\partial \tilde{f}_0}{\partial \boldsymbol{x}}+\dot{p}\frac{\partial \tilde{f}_0}{\partial p}+\dot{\xi}\frac{\partial \tilde{f}_0}{\partial \xi}+\frac{\partial \tilde{f}_1}{\partial \zeta}=C\left[\tilde{f}_0\right], \tag{2.17b}$$

with the last term on the left hand side including a higher order component of the distribution function since $\dot{\zeta}=\Omega=\tau_\Omega^{-1}\sim\mathcal{O}(\epsilon_\Omega^{-1}\tau_{\mathrm{b}}^{-1})$. Equation (2.17b) can now be averaged over the gyro angle using

$$\langle\cdots\rangle_\zeta=\frac{1}{2\pi}\int_0^{2\pi}\cdots\,\mathrm{d}\zeta. \tag{2.18}$$

Since the first term of equation (2.17b) is independent of ζ, the gyro average results in the identity operation. Further, since $\tilde{f}_1$ must be 2π-periodic in ζ, the term $\partial\tilde{f}_1/\partial\zeta$ must vanish. In the remaining terms, the only dependence on ζ is found in the coefficients. To evaluate their gyro averages, let us first decompose the direction of motion $\hat{\boldsymbol{v}}$ of the particle into

$$\hat{\boldsymbol{v}} = \hat{\boldsymbol{b}}\xi + \sqrt{1-\xi^2}\left(\hat{\boldsymbol{e}}_1\cos\zeta + \hat{\boldsymbol{e}}_2\sin\zeta\right), \tag{2.19}$$

where the orientation of $\hat{\boldsymbol{e}}_1$ and $\hat{\boldsymbol{e}}_2$ is arbitrary, beyond the requirement that they form an orthonormal basis together with the magnetic field direction $\hat{\boldsymbol{b}}$. Since $\dot{\boldsymbol{x}} = \boldsymbol{v}$, we first have that

$$\left\langle\dot{\boldsymbol{x}}\right\rangle_\zeta = \left\langle v\hat{\boldsymbol{v}}\right\rangle_\zeta = v\left\langle\hat{\boldsymbol{b}}\xi + \sqrt{1-\xi^2}\left(\hat{\boldsymbol{e}}_1\cos\zeta + \hat{\boldsymbol{e}}_2\sin\zeta\right)\right\rangle_\zeta = v_\parallel\hat{\boldsymbol{b}}. \tag{2.20}$$

For $\langle\dot{p}\rangle_\zeta$ we can similarly utilise (2.19) and find

$$\left\langle\dot{p}\right\rangle_\zeta = \left\langle q\left(\boldsymbol{E} + \boldsymbol{v}\times\boldsymbol{B}\right)\cdot\hat{\boldsymbol{v}}\right\rangle_\zeta = q\xi E_\parallel, \tag{2.21}$$

where we introduced $E_\parallel = \boldsymbol{E}\cdot\hat{\boldsymbol{b}}$. The evaluation of the term involving $\langle\dot{\xi}\rangle_\zeta$ is lengthy, and we only state here the result:

$$\left\langle\dot{\xi}\right\rangle_\zeta = \left(1-\xi^2\right)\left[\frac{v\nabla\cdot\hat{\boldsymbol{b}}}{2} + \frac{qE_\parallel}{p}\right]. \tag{2.22}$$

The resulting equation, known as the gyro-averaged kinetic equation, is

$$\frac{\partial f}{\partial t} + v_\parallel\hat{\boldsymbol{b}}\cdot\frac{\partial f}{\partial\boldsymbol{x}} + q\xi E_\parallel\frac{\partial f}{\partial p} + \left(1-\xi^2\right)\left[\frac{v\nabla\cdot\hat{\boldsymbol{b}}}{2} + \frac{qE_\parallel}{p}\right]\frac{\partial f}{\partial\xi} = \left\langle C\left[f\right]\right\rangle_\zeta, \tag{2.23}$$

where we have re-labelled the gyro angle independent $\tilde{f}_0 \to f$.

2.3.2 Poloidal angle average

The next fastest time scale, according to our ordering (2.12), is the bounce time scale τ_b. This is the time scale on which particles transit and return to their initial position in the poloidal plane, thus suggesting that we should average over the poloidal angle θ. However, due to the adiabatic invariance of the magnetic moment, there is an implicit coupling between the poloidal angle θ and the pitch ξ. This significantly complicates integration over the poloidal angle, requiring us to first introduce an alternative to the pitch ξ which is constant during a poloidal transit. A valid option is the magnetic moment $\mu = p_\perp^2/2mB$, although in this work, as described in section 2.2.2 we prefer to use the value ξ_0

of the particle pitch at the point of minimum magnetic field $B = B_{\mathrm{min}}$ along the orbit. From the conservation of μ, we thus have that

$$\frac{p^2\left(1-\xi^2\right)}{2mB} = \frac{p^2\left(1-\xi_0^2\right)}{2mB_{\mathrm{min}}}, \tag{2.24}$$

allowing us to solve for ξ and obtain

$$\xi = \sigma\sqrt{1-\frac{B}{B_{\mathrm{min}}}\left(1-\xi_0^2\right)}. \tag{2.25}$$

Here, $\sigma = \pm 1$ is a parameter which indicates the direction along the field line in which the particle is currently moving. An integration in phase space will thus involve an integration over ξ_0 *and* a sum over the two possible values of σ. From equation (2.25) we can deduce that the correct differential element to use when integrating over ξ_0 is

$$\mathrm{d}\xi = \frac{\xi_0 B}{\xi B_{\mathrm{min}}}\mathrm{d}\xi_0. \tag{2.26}$$

This also allows us to write the last term on the left hand side of equation (2.23) as

$$\left(1-\xi^2\right)\left[\frac{v\nabla\cdot\hat{\boldsymbol{b}}}{2}+\frac{qE_\parallel}{p}\right]\frac{\partial f}{\partial\xi} = \left(1-\xi_0^2\right)\left[\frac{v\boldsymbol{B}\cdot\nabla(1/B)}{2}+\frac{qE_\parallel}{p}\right]\frac{\xi}{\xi_0}\frac{\partial f}{\partial\xi_0}, \tag{2.27}$$

where we also used that $\nabla\cdot\hat{\boldsymbol{b}} = B^{-1}\nabla\cdot\boldsymbol{B} + \boldsymbol{B}\cdot\nabla(1/B) = \boldsymbol{B}\cdot\nabla(1/B)$, with the last equality resulting from the fact that $\nabla\cdot\boldsymbol{B} = 0$. The operator $\boldsymbol{B}\cdot\nabla$ also appears in the term $v_\parallel\hat{\boldsymbol{b}}\cdot\partial f/\partial\boldsymbol{x}$ and can be further simplified. This operator can generally be written

$$\hat{\boldsymbol{b}}\cdot\frac{\partial f}{\partial\boldsymbol{x}} = \hat{\boldsymbol{b}}\cdot\left(\nabla\psi\frac{\partial f}{\partial\psi}+\nabla\theta\frac{\partial f}{\partial\theta}+\nabla\varphi\frac{\partial f}{\partial\varphi}\right). \tag{2.28}$$

Since the magnetic field of a tokamak is symmetric in the toroidal angle φ, and since we do not consider fluctuations in the toroidal direction, it follows that $\partial f/\partial\varphi = 0$. Since flux surfaces are nested and do not intersect, it also follows from the definition of our coordinate system that $\hat{\boldsymbol{b}}\cdot\nabla\psi = 0$. The only remaining term in equation (2.28) is therefore the one involving $\nabla\theta$:

$$\hat{\boldsymbol{b}}\cdot\frac{\partial f}{\partial\boldsymbol{x}} = \hat{\boldsymbol{b}}\cdot\nabla\theta\frac{\partial f}{\partial\theta}. \tag{2.29}$$

This allows us to write the gyro-averaged kinetic equation (2.23) as

$$\begin{gathered}\frac{\partial f}{\partial t}+v_{\|}\hat{\boldsymbol{b}}\cdot\nabla\theta\frac{\partial f}{\partial\theta}+q\xi E_{\|}\frac{\partial f}{\partial p}+\\ \frac{\xi}{\xi_0}\left(1-\xi_0^2\right)\left[\frac{v\boldsymbol{B}\cdot\nabla\theta}{2}\frac{\partial(1/B)}{\partial\theta}+\frac{qE_{\|}}{p}\right]\frac{\partial f}{\partial\xi_0}=\left\langle C\left[f\right]\right\rangle_{\zeta}.\end{gathered}\tag{2.30}$$

Now, expanding f in a series $f=\bar{f}_0+\bar{f}_1+\ldots$, using a parameter ϵ_{b} corresponding to the ratio of transit to the collisional time scale, we substitute this series into the gyro-averaged kinetic equation (2.30) and group the terms by order. The definition of τ_{b}, as an integral over $v_{\|}^{-1}$, mandates that we order $v_{\|}\sim\mathcal{O}(\epsilon_{\mathrm{b}}^{-1}\tau_{\mathrm{c}}^{-1})$. The leading order term in the gyro-averaged kinetic equation after substitution is therefore

$$v_{\|}\hat{\boldsymbol{b}}\cdot\nabla\theta\frac{\partial\bar{f}_0}{\partial\theta}=0,\tag{2.31}$$

implying that $\bar{f}_0$ is independent of the poloidal angle. The next order equation is

$$\begin{gathered}\frac{\partial\bar{f}_0}{\partial t}+v_{\|}\hat{\boldsymbol{b}}\cdot\nabla\theta\frac{\partial\bar{f}_1}{\partial\theta}+q\xi E_{\|}\frac{\partial\bar{f}_0}{\partial p}+\\ \frac{\xi}{\xi_0}\left(1-\xi_0^2\right)\left[\frac{v\boldsymbol{B}\cdot\nabla\theta}{2}\frac{\partial B}{\partial\theta}+\frac{qE_{\|}}{p}\right]\frac{\partial\bar{f}_0}{\partial\xi_0}=\left\langle C\left[\bar{f}_0\right]\right\rangle_{\zeta}.\end{gathered}\tag{2.32}$$

This is the equation we will now average using the operator

$$\langle\cdots\rangle_{\theta}=\frac{4\pi^2}{\mathcal{V}'}\oint\cdots\left|p^2\frac{\xi_0 B}{\xi B_{\min}}\right|\mathcal{J}\,\mathrm{d}\theta.\tag{2.33}$$

with the factor p^2 resulting from the spherical coordinate transformation made in momentum space, $\mathrm{d}\boldsymbol{p}=p^2\,\mathrm{d}p\mathrm{d}\xi\mathrm{d}\zeta$. Here we have introduced

$$\mathcal{V}'=4\pi^2\int_0^{2\pi}\left|p^2\frac{\xi_0 B}{\xi B_{\min}}\right|\mathcal{J}\,\mathrm{d}\theta.\tag{2.34}$$

as well as the configuration space Jacobian $\mathcal{J}$, which accounts for the coordinate transformation $\boldsymbol{x}\to(\psi,\theta,\varphi)$, and is generally given by

$$\mathcal{J}=\frac{1}{|\nabla\psi\cdot(\nabla\theta\times\nabla\varphi)|}.\tag{2.35}$$

A toroidally symmetric magnetic field can be written as

$$\boldsymbol{B}=G(\psi)\nabla\varphi+\frac{1}{2\pi}\nabla\varphi\times\nabla\psi,\tag{2.36}$$

for some function $G(\psi)$ describing the toroidal magnetic field variation, so the Jacobian takes the form

$$\mathcal{J} = \frac{1}{2\pi \left|\boldsymbol{B} \cdot \nabla\theta\right|}. \tag{2.37}$$

The limits of integration in (2.33) depend on whether the particle is trapped. If the particle follows a circulating orbit, then we integrate between $\theta = 0$ and $\theta = 2\pi$, exactly one poloidal transit. If, however, the particle is trapped, having

$$\xi_0^2 \leq 1 - \frac{B_{\mathrm{min}}}{B}, \tag{2.38}$$

we instead let

$$\langle \cdots \rangle_\theta = \frac{4\pi^2}{\mathcal{V}'} \sum_{\sigma=\pm 1} \int_{-\theta_{\mathrm{b}}}^{\theta_{\mathrm{b}}} \cdots \left| p^2 \frac{\xi_0 B}{\xi B_{\mathrm{min}}} \right| \mathcal{J}\, \mathrm{d}\theta, \tag{2.39}$$

where θ_{b} is the poloidal angle at which the particle bounces, characterised by $B(\theta_{\mathrm{b}}) = B_{\mathrm{min}}/(1-\xi_0^2)$. The sum in equation (2.39) runs over the two possible values of the parameter σ, introduced in equation (2.25).

Since $\bar{f}_0$ is independent of θ, the only terms with a non-trivial dependence on θ in equation (2.32) are those involving $\hat{\boldsymbol{b}} \cdot \nabla$, $\boldsymbol{B} \cdot \nabla$ and ξ. Starting with the $\partial \bar{f}_1/\partial\theta$ term, we obtain the integral

$$\begin{aligned} \left\langle v_\parallel \hat{\boldsymbol{b}} \cdot \nabla\theta \frac{\partial \bar{f}_1}{\partial\theta} \right\rangle_\theta &= \frac{2\pi\sigma v \left|\xi_0\right|}{B_{\mathrm{min}}\mathcal{V}'} \oint \frac{\boldsymbol{B} \cdot \nabla\theta}{\left|\boldsymbol{B} \cdot \nabla\theta\right|} \frac{\partial \bar{f}_1}{\partial\theta}\, \mathrm{d}\theta = \\ &= \frac{2\pi\sigma v \left|\xi_0\right|}{B_{\mathrm{min}}\mathcal{V}'} \operatorname{sgn}\left(\boldsymbol{B} \cdot \nabla\theta\right) \oint \frac{\partial \bar{f}_1}{\partial\theta}\, \mathrm{d}\theta. \end{aligned} \tag{2.40}$$

By definition, the poloidal flux is independent of θ, meaning that the only θ dependence appearing in the integrand of equation (2.40) is in $\bar{f}_1$. This component of the distribution function must however be 2π-periodic in θ, causing the term to vanish by the fundamental theorem of calculus.

The $\partial\bar{f}_0/\partial\xi_0$ term also has a non-trivial θ dependence. Applying the averaging operator to it, we obtain

$$\begin{aligned}
&\left\langle \frac{\xi}{\xi_0}\left(1-\xi_0^2\right)\left[\frac{v\boldsymbol{B}\cdot\nabla\theta}{2}\frac{\partial(1/B)}{\partial\theta}+\frac{qE_\parallel}{p}\right]\frac{\partial\bar{f}_0}{\partial\xi_0}\right\rangle_\theta = \\
&= 2\pi\frac{1-\xi_0^2}{B_{\min}\mathcal{V}'}\left(\oint\frac{\sigma vB}{2}\frac{\partial(1/B)}{\partial\theta}\frac{\partial\bar{f}_0}{\partial\xi_0}\frac{\boldsymbol{B}\cdot\nabla\theta}{|\boldsymbol{B}\cdot\nabla\theta|}\,\mathrm{d}\theta+\oint\sigma B\frac{qE_\parallel}{p}\frac{\partial\bar{f}_0}{\partial\xi_0}\mathcal{J}\,\mathrm{d}\theta\right) = \\
&= -2\pi\frac{1-\xi_0^2}{B_{\min}\mathcal{V}'}\frac{\partial\bar{f}_0}{\partial\xi_0}\oint\sigma v\frac{\partial\ln B}{\partial\theta}\,\mathrm{d}\theta+\frac{1-\xi_0^2}{\xi_0}\left\langle\frac{q\xi E_\parallel}{p}\frac{\partial\bar{f}_0}{\partial\xi_0}\right\rangle_\theta = \\
&= q\frac{1-\xi_0^2}{p\xi_0}\left\langle\xi E_\parallel\right\rangle_\theta\frac{\partial\bar{f}_0}{\partial\xi_0}.
\end{aligned} \tag{2.41}$$

Finally, we must average the $\partial\bar{f}_0/\partial p$ term. This term contains a θ dependence in ξ, as well as in $E_\parallel$:

$$\left\langle q\xi E_\parallel\frac{\partial\bar{f}_0}{\partial p}\right\rangle_\theta = q\left\langle\xi E_\parallel\right\rangle_\theta\frac{\partial\bar{f}_0}{\partial p} = \frac{4\pi^2 q\,|\xi_0|}{\mathcal{V}'B_{\min}}\frac{\partial\bar{f}_0}{\partial p}\oint\sigma\left(\boldsymbol{B}\cdot\boldsymbol{E}\right)\mathcal{J}\,\mathrm{d}\theta. \tag{2.42}$$

Here we should note two important things. Firstly, the same poloidal angle average of $\xi E_\parallel$ appears in both equations (2.41) and (2.42). Secondly, the integrand in the resulting integral, given explicitly in equation (2.42), changes sign in the bounce points when ξ_0 corresponds to a trapped orbit, due to the sign $\sigma = \xi/|\xi|$ which we sum over. This average therefore vanishes for trapped orbits, representing the fact that trapped particles will be accelerated in one direction along their orbit, and equally decelerated when bouncing back in the other direction.

After averaging the gyro-averaged kinetic equation over the poloidal angle we now arrive at the bounce averaged Fokker-Planck equation

$$\frac{\partial f}{\partial t}+q\left\langle\xi E_\parallel\right\rangle_\theta\frac{\partial f}{\partial p}+q\frac{1-\xi_0^2}{p\xi_0}\left\langle\xi E_\parallel\right\rangle_\theta\frac{\partial f}{\partial\xi_0} = \left\langle\left\langle C\left[f\right]\right\rangle_\zeta\right\rangle_\theta \tag{2.43}$$

where, again, for convenience we have re-labelled $\bar{f}_0 \to f$.

General procedure

The steps taken above illustrate in detail the assumptions needed to reach a bounce-averaged Fokker–Planck equation. The essential steps can now be summarised into a single operation which is needed whenever a new term is to be introduced.

Given an operator $X[f]$, assumed to vary on a time scale much slower than the bounce time scale τ_b, we define the *bounce average of* X as

$$\begin{aligned}\{X[f]\} &\equiv \frac{1}{\mathcal{V}'}\int_0^{2\pi}\left\langle\langle X[f]\rangle_\zeta\right\rangle_\theta \mathrm{d}\varphi = \\ &= \frac{1}{\mathcal{V}'}\int_0^{2\pi}\oint\int_0^{2\pi} X[f]\left|p^2\frac{\xi_0 B}{\xi B_\mathrm{min}}\right|\mathcal{J}\,\mathrm{d}\zeta\mathrm{d}\theta\mathrm{d}\varphi\end{aligned} \tag{2.44}$$

with $\mathcal{V}'$ defined in equation (2.34). The integral over the poloidal angle θ is different depending on whether or not the ξ_0 considered represents a passing or trapped orbit. Specifically,

$$\oint X\,\mathrm{d}\theta = \begin{cases}\int_0^{2\pi} X\,\mathrm{d}\theta, & \text{if } |\xi_0| > \xi_T,\\ \sum_{\sigma=\pm1}\int_{-\theta_\mathrm{b}}^{\theta_\mathrm{b}} X\,\mathrm{d}\theta, & \text{if } |\xi_0| \le \xi_T,\end{cases} \tag{2.45}$$

where the trapped-passing boundary $\xi_T = \sqrt{1 - B_\mathrm{min}/B_\mathrm{max}}$ and θ_b was defined along with the poloidal angle average in equation (2.39)

An average which is closely related to the bounce average is the *flux-surface average*, which is analogous to the bounce average but for quantities which vary only spatially (i.e. independent of momentum coordinates). The average value of such a quantity on a given flux surface is

$$\langle X\rangle = \frac{1}{V'}\int_0^{2\pi}\int_0^{2\pi} X\,\mathcal{J}\,\mathrm{d}\theta\mathrm{d}\varphi, \tag{2.46}$$

with

$$V' = \int_0^{2\pi}\int_0^{2\pi}\mathcal{J}\,\mathrm{d}\theta\mathrm{d}\varphi, \tag{2.47}$$

which, along passing orbits, can be related to $\mathcal{V}'$ via

$$\mathcal{V}' = 2\pi p^2\left\langle\frac{\xi_0 B}{\xi B_\mathrm{min}}\right\rangle V'. \tag{2.48}$$

Such averages often appear when bounce averaging operators for the Fokker–Planck equation. In fact, equation (2.42) can be written in terms of the flux-surface average of the electric field as

$$q\left\langle\xi E_\parallel\right\rangle_\theta\frac{\partial f}{\partial p} = q\Theta(\xi_0)\frac{\langle\boldsymbol{E}\cdot\boldsymbol{B}\rangle}{\langle\xi_0 B/\xi B_\mathrm{min}\rangle}\frac{\partial f}{\partial p}, \tag{2.49}$$

where the step function $\Theta(\xi_0)$ is

$$\Theta\left(\xi_0\right) = \begin{cases}1, & \text{if } |\xi_0| > \xi_T,\\ 0, & \text{otherwise.}\end{cases} \tag{2.50}$$

2.3.3 Validity of bounce average in tokamak disruptions

The validity of the bounce average hinges on the time scale ordering (2.12). Disruptions are however characterised by a wide variation in many plasma parameters, which will also affect the time scales of various phenomena. In particular, one could question the ordering

$$\tau_\mathrm{b} \ll \tau_\mathrm{c}, \tau_\mathrm{acc}, \tag{2.51}$$

i.e. that the poloidal transit time τ_b is much shorter than the collision and acceleration times. The transit time is longer for trapped particles, and so for τ_b we consider the transit time of a trapped particle with speed v travelling along a flux surface with radius r [41]:

$$\tau_\mathrm{b} = \frac{qR}{v\sqrt{r/R}}, \tag{2.52}$$

where q is the safety factor and R is the plasma major radius.

The shortest collisional time scale is that for electrons to deflect off of ions, and it is given by [40, 42]

$$\tau_\mathrm{c} \approx 200\,\mathrm{s}\frac{p^3\,[\mathrm{MeV}/c]}{\gamma Z_\mathrm{eff}\left(n_\mathrm{e}\,[10^{20}\,\mathrm{m}^{-3}]\right)} \tag{2.53}$$

where n_e is the density of electrons and Z_eff the effective charge number of the plasma. In a disruption, the temperature drops by several orders of magnitude while a large amount of highly charged ions are injected. Both lead to a dramatic drop in the collision time, and for $T_\mathrm{e} = 5\,\mathrm{eV}$ and $Z_\mathrm{eff} = 2$, the collision time for a thermal particle is only $\tau_\mathrm{c} \sim 10^{-6}\,\mathrm{s}$. If the collision time is shorter, or even comparable to the transit time, particles will deviate from their orbit before they can return to their original point in the poloidal plane, invalidating the assumption that f depends weakly on the poloidal angle θ made in the bounce-average theory.

Similarly, the relevant electric field acceleration time scale can be estimated by considering the time it takes for a fast electron to double its momentum from $p = p_0$ to $p = 2p_0$. Using results which will be derived in section 3.1, the force balance for an electron with momentum p can be written

$$\frac{\mathrm{d}p}{\mathrm{d}t} = eE_\parallel - eE_\mathrm{c}\frac{m_\mathrm{e}^2c^2 + p^2}{p^2}, \tag{2.54}$$

where E_c is the threshold electric field required for runaway, derived in section 3.1, and $p \gg p_\mathrm{th}$ was assumed in order to simplify the collisional friction force. By integrating equation (2.54) in time, we can solve for the acceleration time and find

$$\tau_{\mathrm{acc}} = \frac{p_{\mathrm{c}}^3}{m_{\mathrm{e}}^2 c^2 e E_{\mathrm{c}}} \left[\frac{p_0}{p_{\mathrm{c}}} - \frac{1}{2} \ln \left(1 - \frac{2p_0/p_{\mathrm{c}}}{\frac{2p_0^2}{p_{\mathrm{c}}^2} + \frac{p_0}{p_{\mathrm{c}}} - 1} \right) \right], \tag{2.55}$$

where the critical momentum for runaway $p_{\mathrm{c}} = m_{\mathrm{e}} c / \sqrt{E_\parallel / E_{\mathrm{c}} - 1}$, as derived in section 3.1. In strong electric fields ($E_\parallel \gg E_{\mathrm{c}}$), the acceleration time for fast particles ($p_0 \gtrsim m_{\mathrm{e}} c \gg p_{\mathrm{c}}$) scales with electron momentum and electric field strength as

$$\tau_{\mathrm{acc}} \propto \frac{p_0}{E_\parallel}. \tag{2.56}$$

Close to $p_0 = p_{\mathrm{c}}$, the acceleration time approaches infinity logarithmically, meaning that τ_{acc} must attain a minimum for some $p_0 > p_{\mathrm{c}}$. An approximate analysis yields that the minimum acceleration time is

$$\tau_{\mathrm{acc}}^{\mathrm{min}} \approx \sqrt{\frac{n_{\mathrm{e}}\,[10^{20}\,\mathrm{m}^{-3}]}{\left(E_\parallel\,[\mathrm{V/m}]\right)^3}}\,\mathrm{ms}, \tag{2.57}$$

which is the acceleration time of an electron with $p_0 \approx m_{\mathrm{e}} c \sqrt{3E_{\mathrm{c}}/E_\parallel}$.

The dependence of the various time scales on the particle energy requires examination of the time scales at the relevant energies for the validity of the theory to be established. The three time scales discussed here are plotted in figure 2.4 for typical ITER-like plasma parameters. To reconcile the effects captured by the bounce-average theory on some energy scales with the lack of these effects on other time scales, the DREAM code, introduced in Paper G, separates electrons into three subpopulations based on their energies, allowing different methods to be applied to electrons in different energy ranges.

As shown in figure 2.4, the slowest electrons, with momentum $p \sim p_{\mathrm{th}}$, have transit times $\tau_{\mathrm{b}} \sim 10^{-4}\,\mathrm{s}$ after the TQ, while the collision time may be as low as $10^{-6}\,\mathrm{s}$. The dynamics of these particles will therefore be dominated by collisions and the bounce-average theory is not valid. Collisions will however quickly drive the particles to thermal equilibrium and cause them to be distributed according to a Maxwellian. In DREAM, the thermal particles can therefore be modelled as a fluid.

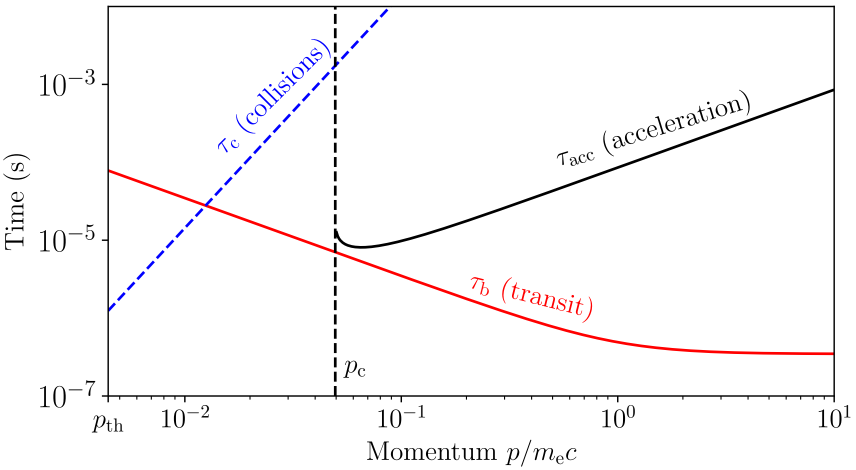

Figure 2.4: Comparison of the important time scales for the bounce average theory at different electron energies. The plasma parameters assumed are $n_e = 10^{20}\,\mathrm{m}^{-3}$, $T_e = 5\,\mathrm{eV}$, $Z_{\mathrm{eff}} = 2$, $E_{\|} = 20\,\mathrm{V/m}$, $R = 6\,\mathrm{m}$, $r = 0.5\,\mathrm{m}$ and $q = 5$.

For the faster electrons, collisions are not as important and the assumption $\tau_b \ll \tau_c$ will generally be satisfied. However, the rapid acceleration by the electric field may void the result (2.49) and detrap bouncing particles. The fastest electrons will have acceleration times on the order of milliseconds, while their transit times are counted in nanoseconds in ITER, satisfying the bounce-average assumptions by a clear margin. Of more concern are the moderately energetic particles with the shortest acceleration times. For these particles, the acceleration time in the ITER disruption considered in figure 2.4 is approximately 10^{-5} s, only slightly longer than the transit time for the trapped electrons. In this momentum region, the assumption $\tau_b \gg \tau_{acc}$ may therefore break down, invalidating the bounce average theory, as demonstrated in Ref. [41].

It is important to point out that the discussion of this section has concerned the validity of the bounce average for studying the generation of runaway electrons in tokamak disruptions. Runaway electrons may however be generated in other scenarios, such as during tokamak startup or during the quiescent phase of operation (if a sufficiently strong electric field is applied), in which the assumptions of the bounce average theory are typically well satisfied.

Chapter 3

Theory of runaway electrons

A peculiar feature of a plasma, first pointed out by Wilson in 1924 [43], is that the friction force due to collisions felt by the fastest electrons is inversely proportional to the square of the electrons' speeds. Since collisional friction is often the dominant braking force felt by most electrons, a constant accelerating force of sufficient strength would increase the energy of the electrons indefinitely and cause them to "run away". Such runaway electrons are however far from a peripheral curiosity in plasma physics—their presence is of crucial importance in the initiation of thunderstorms [44], and they occur in solar flares [45] as well as during startup [46] and shut-down [13] of tokamak discharges. In this thesis we are primarily concerned with circumstances pertaining to the latter, making many of our results specific to the conditions of a tokamak. Nonetheless, most of the fundamental principles outlined in this chapter apply to runaway generation in any plasma.

Over recent years, runaway electrons occurring in tokamaks have received much attention due to the potentially devastating impact they may have on future reactor-scale tokamaks [47]. If a plasma instability grows too large, a so-called *disruption* may occur, converting a significant fraction of the plasma magnetic energy into kinetic energy of runaway electrons. The resulting beam of relativistic electrons can be difficult to control and may itself trigger further plasma instabilities which deform the toroidal plasma column [11]. If the beam comes in contact with the tokamak wall, or any of its plasma facing components, significant energy can be deposited in a localised region, leading to severe damage to the device.

In this chapter we will review the theory of runaway electrons in tokamaks. We begin by introducing some fundamental considerations, such as what a runaway electron is and what circumstances are necessary for an electron to run away. We then proceed to discuss the topic of tokamak disruptions, which is the main type of runaway generation event we are concerned with in this thesis. After giving an overview of tokamak disruptions, we discuss specifically the runaway generation during the disruption and the subsequent evolution of the electrons.

3.1 Criteria for runaway

Runaway acceleration occurs whenever the force exerted on an electron by a macroscopic electric field is stronger than the braking force resulting from collisions with other particles in the plasma. The first detailed account of electron runaway was given by Dreicer [12, 48], who considered a uniform plasma in which electrons and ions are in thermal equilibrium. By multiplying the Fokker–Planck equation (2.43) with the parallel momentum $p_\parallel$ and integrating over all of momentum space, he obtained the parallel force balance equation

$$\frac{\partial p_\parallel}{\partial t} + eE_\parallel = -p_{\mathrm{th}}\nu_{ee}\Psi(p), \tag{3.1}$$

with the thermal electron-electron collision frequency

$$\nu_{ee} = \frac{e^4 m_{\mathrm{e}} n_{\mathrm{e}} \ln\Lambda}{4\pi\varepsilon_0^2 p_{\mathrm{th}}^3}, \tag{3.2}$$

m_{e} the electron rest mass, n_{e} the electron density, $\ln\Lambda$ the Coulomb logarithm, and $p_{\mathrm{th}} = \sqrt{2m_{\mathrm{e}}T_{\mathrm{e}}}$ the thermal momentum, with T_{e} the electron temperature. Equation (3.1) describes the evolution of the mean momentum of the plasma electrons when influenced by an applied electric field $E_\parallel$ and collisions. The right hand side of equation (3.1) results from the integration of a linearised version of the collision operator, specifically from the dynamic friction component $\boldsymbol{p}\cdot\boldsymbol{A}$ in equation (2.9), where the function $\Psi(p)$ describes the energy-dependence of the collisional friction, plotted in figure 3.1. The function $\Psi(p)$ grows with p until the thermal momentum p_{th}, after which it decreases. As $p \to \infty$, $\Psi(p) \approx p_{\mathrm{th}}^2/(mv)^2$, thus decreasing with the inverse square of the speed v and approaching a small but finite value in the limit.

It is customary to normalise all terms in equation (3.1) to $2p_{\mathrm{th}}\nu_{ee}$. Doing so allows us to write the electric field term as $E_\parallel/E_{\mathrm{D}}$, with

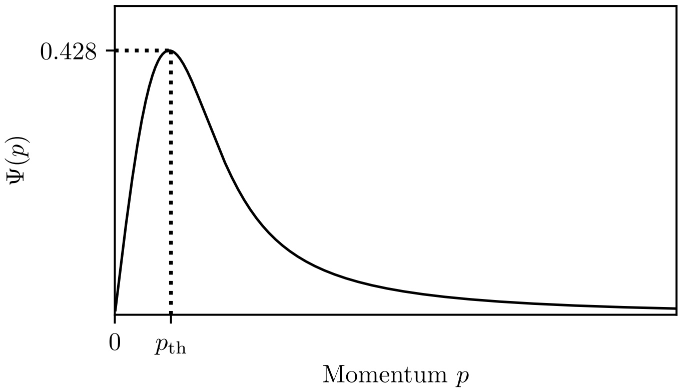

Figure 3.1: Plot of the dimensionless function $\Psi(p)$ describing the momentum dependence of the collisional friction force experienced by an electron in a plasma.

$E_{\mathrm{D}} = 2p_{\mathrm{th}}\nu_{ee}/e$. The *Dreicer field* E_{D} is one of the essential reference parameters in the theory of runaway electrons which shows up frequently.

Equation (3.1) allows us to draw a number of important conclusions about what will happen to electrons when a sufficiently strong electric field $E_{\|}$ is applied. Due to the decreasing behaviour of $\Psi(p)$ for $p > p_{\mathrm{th}}$, any electron which is sufficiently fast for the electric field to overcome the collisional friction will continue to accelerate indefinitely. An electron with $v \gg v_{\mathrm{th}} = p_{\mathrm{th}}/m_{\mathrm{e}}$ will thus run away if the electric field is

$$eE_{\|} \geq p_{\mathrm{th}}\nu_{ee}\Psi(p) \approx \nu_{ee}\frac{p_{\mathrm{th}}^3}{m_{\mathrm{e}}^2 v^2} = \frac{e^4 n_{\mathrm{e}} \ln\Lambda}{4\pi\varepsilon_0^2 m_{\mathrm{e}} v^2}. \tag{3.3}$$

Notably, since no electron can move faster than the speed of light c, no electrons will run away if the electric field is below the threshold value [49]

$$E_{\mathrm{c}} = \frac{e^3 n_{\mathrm{e}} \ln\Lambda}{4\pi\varepsilon_0^2 m_{\mathrm{e}} c^2} = \frac{T_{\mathrm{e}}}{mc^2}E_{\mathrm{D}}. \tag{3.4}$$

For a given electric field $E_{\|}$, equation (3.3) can be solved for the speed v_{c} of the slowest electrons to run away. This critical speed can be expressed succinctly as

$$\frac{v_{\mathrm{c}}}{c} = \sqrt{\frac{E_{\mathrm{c}}}{E_{\|}}} \quad \Leftrightarrow \quad \frac{p_{\mathrm{c}}}{m_{\mathrm{e}}c} = \frac{1}{\sqrt{E_{\|}/E_{\mathrm{c}} - 1}}, \tag{3.5}$$

where the relativistic relation between velocity and momentum was used.

The maximum of $\Psi(p)$ also yields a value of $E_\|$ above which all electrons will immediately run away:

$$eE_\| \geq p_{\rm th}\nu_{ee} \max_p \Psi(p) \approx 0.428 p_{\rm th}\nu_{ee} = 0.214 eE_{\rm D}. \tag{3.6}$$

For any values of $E_\|$ between $E_{\rm c}$ and $0.214E_{\rm D}$, only a fraction of electrons will be immediately runaway accelerated.

Collisions will however strive to maintain the electron distribution at thermal equilibrium, meaning that collisional diffusion processes will fill in any "gaps" in the electron distribution left by runaway electrons, and thus refill the velocity space region above $v_{\rm c}$. This will lead to a diffusive leaking of particles into the $v > v_{\rm c}$ region, and the thermal bulk component of the distribution will gradually be drained of particles. It is therefore possible to convert all electrons to runaways even at values of E lower than that in equation (3.6); one just has to wait for sufficiently many collision times.

The diffusive leaking of particles into the runaway region is now commonly referred to as the *Dreicer* runaway generation mechanism [12, 48]. It is however far from the only mechanism by which new runaway electrons can be generated. By the nature of the runaway region, any particle that finds itself with $v > v_{\rm c}$ will be continuously accelerated and run away, regardless of its past. Any interaction leading to an electron gaining sufficient energy—or, as we shall see, not losing too much energy—to enter the runaway region will gain net energy from the electric field and run away. This includes electron-electron knock-on collisions, radioactive β-decay of elements producing sufficiently energetic electrons, and collisions with cosmic radiation. In the next section we will consider runaway acceleration in tokamaks specifically and will then become acquainted with some of these alternative runaway generation mechanisms which are the cause of much concern for future reactor-scale tokamaks.

Runaway threshold in experiment

The theoretically predicted threshold field (3.3) was derived by considering only a balance between the electric field and collisional friction. In an experimental setting, several other effects also play a role, effectively enhancing the threshold. Several experiments [50–53] have measured the "effective" threshold field $E_{\rm c,eff}$ and have found that it sometimes differs from the theoretical value (3.3) by as much as an order of magnitude. This difference is usually accredited to a number of effects which enhance the braking force acting on the electron. In particular, synchrotron radiation [54, 55], bremsstrahlung and collisions with partially ionised atoms [56] have been shown to significantly influence the threshold field.

3.2 Tokamak disruptions

Tokamak plasmas are inherently very sensitive to a number of operating conditions. For example, if the electron density or plasma current is too high, or if too many heavy impurity atoms accumulate in the plasma, the energy confinement may decline drastically, leading to a *disruption* [9, 57]. The exact cause of a tokamak disruption may differ between different discharges and devices, but the evolution of the disruption, after being triggered, generally follows the same overall steps. First, the plasma temperature decreases significantly on a short (typically $\lesssim 1\,\mathrm{ms}$) time scale, during what is known as the *thermal quench* (TQ). This temperature drop is usually due to excessive radiation by impurities, heat transport resulting from magnetic perturbations, or, perhaps most commonly, a combination of both. The resulting low temperature causes inter-particle collisions to increase, leading to a significantly increased plasma resistivity which severely limits the ability of the plasma to carry a toroidal current.

In the second step, called the *current quench* (CQ), the plasma current then decays, typically on a time scale which is much longer than that of the TQ ($\sim 10\,\mathrm{ms}$). According to Faraday's law, the decaying plasma current must induce an electric field which is proportional to the current decay rate. Due to the usually fast current decay rate, often on the order of a few milliseconds, the induced electric field reaches values well above the threshold field E_c, allowing for significant runaway acceleration of electrons. During the CQ, a significant fraction of the pre-disruption plasma current may therefore be converted into current carried by runaway electrons, leading into the third and final phase of the disruption, known as the *runaway plateau.* Figure 3.2 gives a schematic overview of the major phases of a typical tokamak disruption.

As illustrated by figure 3.2, tokamak disruptions involve large variations in several physical quantities, with the exact behaviour of each depending on the variation of the others. To reliably calculate how many runaway electrons are generated in a disruption, and thus guide the design of any disruption avoidance or mitigation scheme, one must there-

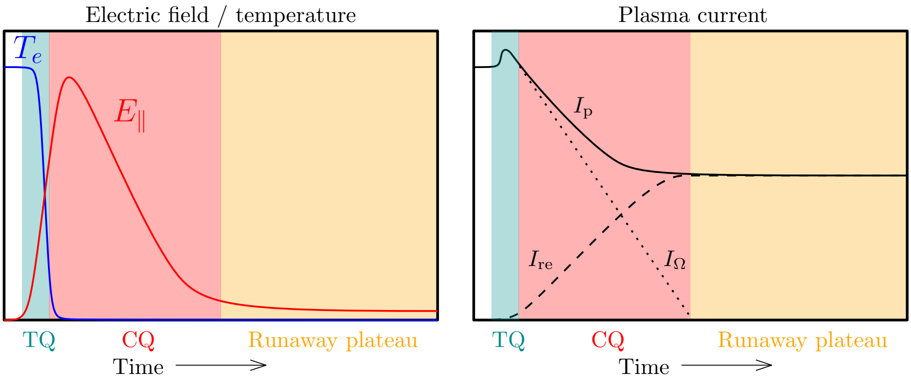

Figure 3.2: In the first phase of a disruption, the thermal quench (TQ), the temperature T_e rapidly drops. As a result of the increased electrical resistivity of the plasma, the ohmically driven current I_Ω is forced to decay in the current quench (CQ) phase. This induces a parallel electric field $E_\parallel$ which generates a current I_re carried by runaway electrons and eventually leads to the runaway plateau, where all remaining plasma current is carried by runaway electrons.

fore use a self-consistent model which evolves the background plasma as well as the runaway electrons simultaneously. Such a model was first developed for a cylindrical plasma in Ref. [58], which considered the effect of injecting large amounts of noble gases into the plasma on the runaway electron generation. Similar models have been used later [59–63], and in Paper G a generalised model was introduced, accounting for toroidal geometry and using the most recent and accurate generation rates for runaway electrons.

At the core of the aforementioned models for disruption-generated runaway electrons is the combined Ampère-Faraday equation, which describes the diffusion of the electric field $\boldsymbol{E}$ through the plasma and its interaction with the plasma current density $\boldsymbol{j}$:

$$\nabla^2 \boldsymbol{E} = \mu_0 \frac{\partial \boldsymbol{j}}{\partial t}. \tag{3.7}$$

The current density is assumed to consist of an ohmic and a runaway component, j_Ω and j_re respectively, and we neglect the plasma pressure,

$$\boldsymbol{j} = \hat{\boldsymbol{b}} j_\parallel = \hat{\boldsymbol{b}} \left(j_\Omega + j_\mathrm{re} \right), \tag{3.8}$$

where $\hat{\boldsymbol{b}}$ denotes the magnetic field direction. The ohmic current density is calculated from the generalised Ohm's law $j_\Omega/B = \sigma\langle\boldsymbol{E}\cdot\boldsymbol{B}\rangle/\langle B^2\rangle$, with $\sigma = \sigma(n_\mathrm{e}, T_\mathrm{e}, Z_\mathrm{eff})$ denoting the plasma conductivity [64, 65], while the runaway current density is obtained by assuming that runaway electrons travel at the speed of light parallel to the magnetic field

$$\boldsymbol{j}_\mathrm{re} = ecn_\mathrm{re}\hat{\boldsymbol{b}}, \tag{3.9}$$

where n_re is the density of runaway electrons. The runaway density n_re is in turn determined either from known formulas for the generation rate $\partial n_\mathrm{re}/\partial t$, or by solving the Fokker–Planck equation (2.43), both of which depend sensitively on the parallel electric field $E_\parallel$. If the runaway electron distribution function f_re is known, the current density (3.9) may also be obtained as the $e\boldsymbol{v}$ moment of f_re.

In addition to $E_\parallel$, $j_\parallel$ and n_re, a self-consistent disruption model must also account for the evolution of the plasma temperature and ion densities [66]. At the onset of the TQ, the temperature evolution is mainly determined by the diluting effect of adding cold electrons to the plasma, as well as the rate at which atoms radiate when they are excited, ionised and collide with each other and electrons to produce bremsstrahlung. Turbulent transport due to magnetic field stochastization can also play a prominent role in reducing the heat content of the plasma. Towards the end of the TQ, heating provided by the induced electric field becomes sufficient to balance the heat losses, leading to a stable final temperature of typically a few electronvolts. The energy balance during a disruption can therefore be modelled with

$$\frac{\partial W_e}{\partial t} = \boldsymbol{j}_\Omega\cdot\boldsymbol{E} - P_\mathrm{rad} + \frac{1}{V'}\frac{\partial}{\partial r}\left[V'D\frac{\partial W_e}{\partial r}\right], \tag{3.10}$$

where the radiated power P_rad depends on the electron temperature and density. The purely diffusive form of the heat transport operator given here does not necessarily represent the circumstances in a disruption perfectly, but is adequate for the case of a fully stochastic magnetic field.

For the ions, we are interested not only in the densities of the various species, but also in the density of ions in the various charge states of different species. This is for two main reasons: firstly, the power radiated by an ion depends sensitively on how many electrons remain bound to its nucleus, leading to a sensitive dependence in P_rad of equation (3.10) on the ion charge state densities. Secondly, collisions between ions and thermal electrons depend on the net charge of the ions, but fast electrons may be able to penetrate the electron cloud and probe the internal structure of the atom [67]. Assuming that electrons are in thermal equilibrium at a density n_e and temperature T_e, the rate of change of the density $n_i^{(j)}$ for ions in charge state j of species i evolves in the collisional radiative model as

$$\frac{\partial n_i^{(j)}}{\partial t} = I_i^{(j-1)} n_\mathrm{e} n_i^{(j-1)} - I_i^{(j)} n_\mathrm{e} n_i^{(j)} + R_i^{(j+1)} n_\mathrm{e} n_i^{(j+1)} - R_i^{(j)} n_\mathrm{e} n_i^{(j)}, \quad (3.11)$$

where $I_i^{(j)} = I_i^{(j)}(n_\mathrm{e}, T_\mathrm{e})$ is the rate of ionisation from the charge state $j \to j+1$, and $R_i^{(j)} = R_i^{(j)}(n_\mathrm{e}, T_\mathrm{e})$ is the rate of recombination from the charge state $j \to j-1$, both of which can be evaluated using numerical tables. It has been shown that the ionisation cross-section is enhanced for relativistic electrons [68], and so if the electron population contains a relativistic component it may significantly alter the ionisation rate calculated for thermal equilibrium. In such cases where runaways are present it may therefore be advisable to either replace or complement the ionisation rates in equation (3.11) with rate coefficients accounting for the non-thermal component of the distribution function, as described in Ref. [68].

3.2.1 Runaway generation mechanisms

Runaway electron generation in tokamak disruptions generally occurs in two phases. First, a population of fast “seed” electrons are generated, typically at the onset of the CQ, during the TQ, or in some cases even before the disruption initiates. In the second phase, knock-on collisions between runaway and thermal electrons transfer a significant amount of energy to the slow electrons and kick them into the runaway region, where they can be further accelerated. Denoted as “primary” are the generation mechanisms that do not require any runaway electrons to be present for more runaways to be produced. The primary generation mechanisms do however tend to only generate a small number of runaways. It is when the primary generation mechanisms are combined with the “secondary” mechanism of the second phase—which will exponentially multiply the number of runaway electrons in the plasma—that the great threat runaway electrons pose to future tokamak reactors is fully realised.

Primary generation

Among the primary runaway generation mechanisms we find the Dreicer mechanism, described in section 3.1, by which electrons diffusively leak into the runaway region. We also count in this category the production of fast electrons via tritium β-decay and Compton scattering with photons from the neutron-activated wall [59]. Of particular concern is however the generation of fast electrons occurring when the plasma cools during the TQ, known as “hot-tail” generation [69, 70]. Since fast electrons are less affected by collisions than slow electrons, they will form a high-energy (or hot) “tail” in the electron distribution function, and take longer to cool down. If the electric field rises before the fast electrons have been able to lose their energy through collisions, the fast electrons may suddenly find themselves in the runaway region.

In contrast to the other primary generation mechanisms, for which accurate analytical expressions exist, the transient nature of the hot-tail mechanism has made it difficult to model both accurately and efficiently. The first analytical expressions describing hot-tail generation assumed that the collision rate is faster than the plasma cooling rate [71, 72], so that the bulk of the electrons remain in thermal equilibrium throughout the cooling. This is however not necessarily appropriate for a disrupting tokamak plasma, for which the cooling can occur very rapidly when a large amount of cold impurities are deposited in the plasma [73]. When the impurities ionise, the electrons they contribute will almost instantaneously form a cold background population with which the hotter electrons can interact, as illustrated in figure 3.3. The sudden appearance of a cold electron population implies two things which makes even a traditional [70, 74] linearised kinetic model inappropriate: (i) the great separation in energy between the particles of the cold and hot populations (typically three or four orders of magnitude) causes the physics of interest to play out on two separate energy scales, putting greater demand on the simulation resolution; (ii) the occurrence of two electron populations may violate the linearisation of the collision operator.

A possible remedy addressing both issues was developed in Ref. [63]. The model presented there makes a number of key assumptions, generally thought to hold during tokamak disruptions:

- The initial (hot) plasma electrons make up a population of their own, initially in thermal equilibrium at the high pre-disruption temperature.

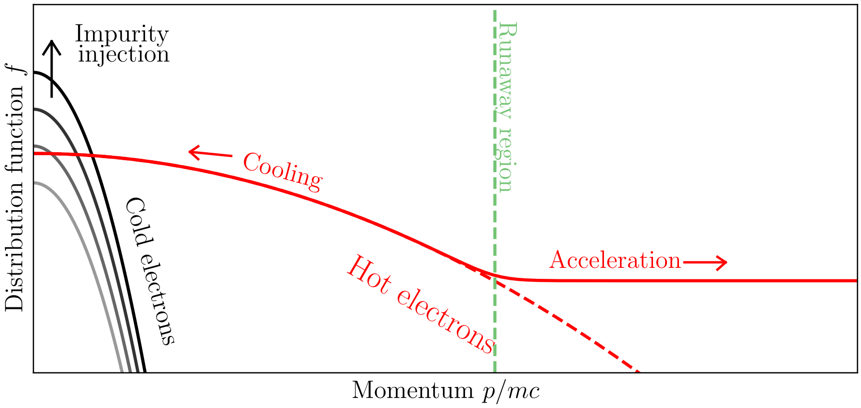

Figure 3.3: Illustration of the typical situation in the early phases of a tokamak disruption where a population of “cold”, injected electrons collide with the original “hot” electrons of the plasma, momentarily giving rise to two distinct near-Maxwellian electron populations. As the hot electrons cool down, an electric field is induced which can accelerate the fastest electrons into the runaway region.

- A large number of (cold) impurities are deposited in the plasma.
- The ionising impurities rapidly release a large number of electrons which form their own low-temperature population. Due to the short collision time of the cold electrons, they will almost instantaneously reach thermal equilibrium amongst themselves.
- The injected impurities are assumed to rapidly release a sufficient number of electrons for the condition $n_{\text{cold}} \gg n_{\text{hot}}$ to be satisfied. This allows the hot electron population to be treated as a perturbation to the otherwise Maxwellian cold electron population.

The cold population is subsequently treated as a fluid, with temperature determined by equation (3.10). The hot population, on the other hand, is treated kinetically by solving the Fokker–Planck equation. Since the cold population is in thermal equilibrium throughout the disruption, and since the cold electrons are significantly less energetic than the hot electrons, one can linearise the collision operator around the cold electron Maxwellian and assume that all hot electrons move at speeds much greater than the cold electron thermal speed, i.e. taking the electron-

electron collision operator in the superthermal limit. This avoids having to resolve the cold electron population kinetically and can significantly reduce the computational expense.

A further simplification of the hot-tail model was introduced in Paper G. There, it is also assumed that collisions dominate the hot electron dynamics, or specifically that the electric field is relatively weak compared to the pitch angle-scattering term in the collision operator. With this assumption, the hot electron distribution function becomes isotropic to leading order, allowing the corresponding Fokker–Planck equation to be averaged over ξ_0 using the same techniques originally developed to account for knock-on collisions in Ref. [14]. The reduced dimensionality in this model makes it computationally an even more efficient option than just taking the superthermal limit of the collision operator.

Secondary generation

Once a seed of runaway electrons has been established through the primary generation mechanisms, the runaway population can multiply through large-angle, or knock-on, collisions [75, 76]. Large-angle collisions are typically rare in tokamak plasmas, and are in fact altogether neglected in the usual Fokker–Planck collisional theory. Nonetheless, they turn out to play a dominant role when the electrons occupy a wide range of energies. Since the condition for runaway is that an electron has $p > p_\mathrm{c}$, a highly energetic electron colliding with a thermal electron may transfer sufficient energy for the thermal electron to cross this energy threshold, while still retaining a significant portion of its energy. The rate of large-angle collisions is proportional to the number of highly energetic electrons that are present,

$$\frac{\mathrm{d}n_\mathrm{re}}{\mathrm{d}t} = \Gamma n_\mathrm{re}. \tag{3.12}$$

This leads to an exponential growth in the number of runaway electrons, with an e-folding time of Γ^{-1}, and in a uniform and fully ionised plasma, the growth rate Γ is given by [14]

$$\Gamma = \frac{e}{m_\mathrm{e}c\ln\Lambda}\frac{E_\parallel - E_\mathrm{c}}{\sqrt{5+Z_\mathrm{eff}}}, \tag{3.13}$$

where Z_eff denotes the effective charge of the plasma. By assuming that $E_\parallel \gg E_\mathrm{c}$, integrating equation (3.12) in time, and utilising the relation

$2\pi R E_\parallel = \partial\psi/\partial t$ between the electric field and the poloidal magnetic flux, with R denoting the major radius, one obtains

$$\ln\frac{n_{\rm re}}{n_{\rm seed}} = \frac{e}{m_{\rm e}c\ln\Lambda}\frac{\Delta\psi/(2\pi R)}{\sqrt{5+Z_{\rm eff}}}, \tag{3.14}$$

where $\Delta\psi$ is the change in poloidal flux during the disruption. The change in poloidal flux is proportional to the plasma current $I_{\rm p}$, meaning that the gain factor (3.14) is also proportional to the plasma current. In future reactor-scale tokamaks, which are foreseen to have about ten times as large plasma currents as the medium-size tokamaks of today, the avalanche gain will be roughly e^{10} times stronger than in experiments today. Estimates put the total amplification of a population of seed electrons (neglecting any losses) in ITER to around 10^{20} [14]. In other words, if even a single runaway electron was to be present at the beginning of the CQ, this would be sufficient to convert a significant fraction of the plasma current to runaway current.

As previously mentioned, the Fokker–Planck theory explicitly neglects large-angle collisions, causing the avalanche effect to be absent from the usual Fokker–Planck equation (2.43). The first avalanche operator introduced in the Fokker–Planck equation was therefore a source term, taking the form [14]

$$S(p,\xi_0,\zeta) = \frac{n_{\rm re}}{4\pi\tau_{\rm c}\ln\Lambda}\delta\left(\xi_0-\xi_\star\right)\frac{m_{\rm e}^3c^3}{p^2}\frac{\partial}{\partial p}\left(\frac{1}{1-\gamma}\right), \tag{3.15}$$

where $\tau_{\rm c} = v_{\rm th}^2/(c^2\nu_{\rm ee})$ is the relativistic electron collision time, $\gamma = \sqrt{p^2+1}$, and $\xi_\star = \sqrt{(\gamma-1)/(\gamma+1)}$. While being convenient to work with, this operator assumes infinite runaway energies, zero pitch angle, and *creates* electrons in the runaway region, rather than accelerating already existing electrons. An improved operator, which accounts for the finite energy of runaways, was presented in Ref. [69], but it still treated the avalanche operator as a source term, rather than as a true collision operator. This was finally remedied in Ref. [77], where a fully conservative large-angle collision operator was derived from the Boltzmann collision integral. The collision operator of Ref. [77] has a number of attractive properties, and was shown to behave differently from the operator (3.15) when $E_\parallel \approx E_{\rm c}$, leading to fewer runaways. In a self-consistent disruption simulation, the difference between the two operators is expected to be small, motivating the implementation of the numerically simpler operator (3.15) in DREAM.

Although large-angle collisions can transfer much of the runaway energy to the target electron, most such collisions only result in sufficient energy being transferred to the target electron for it to enter the runaway region. Once in the runaway region, the target electron will be further accelerated by the electric field and will be able to transfer a fraction of its energy to another slow electron. As a result, most runaways produced via the avalanche mechanism are found at relatively low energies, close to the critical momentum for runaway p_c, and the runaway energy distribution will therefore take the shape of an exponential function. In Ref. [78], an analytical expression for the distribution function of runaway electrons produced via the avalanche mechanism was derived, assuming $E_\| \gg E_\mathrm{c}$ and a quasi-steady state. The formula obtained there was later generalised in Paper K to also capture the near-critical limit $E_\| \to E_\mathrm{c}$, which is often relevant in the runaway plateau, taking the form

$$f_\mathrm{re}(t,p,\xi_0) = \frac{n_\mathrm{re}(t)A(p)}{2\pi m_\mathrm{e}c\gamma_0 p^2}\frac{\exp\left[-\frac{\gamma}{\gamma_0} - A(p)\left(1+\xi\right)\right]}{1-\mathrm{e}^{-2A}}, \tag{3.16}$$

with

$$\begin{aligned}
A(p) &= \frac{E/E_\mathrm{c}+1}{Z_\mathrm{tot}+1}\gamma,\\
n_\mathrm{re}(t) &= n_\mathrm{seed}\mathrm{e}^{\Gamma t} = \int f_\mathrm{re}(t,p,\xi_0)\,p^2\mathrm{d}\xi_0\mathrm{d}p,\\
\gamma_0 &= \sqrt{5+Z_\mathrm{eff}}\ln\Lambda\\
Z_\mathrm{tot} &= \frac{1}{n_\mathrm{tot}}\sum_i n_i Z_i^2.
\end{aligned}$$

The total plasma charge Z_tot accounts for the density of both free and bound electrons, $n_\mathrm{tot} = n_\mathrm{e,free} + n_\mathrm{e,bound}$, and is therefore independent of the charge state of the ions of the plasma. Equation (3.16) exhibits the anticipated exponential dependence on the electron energy ($\sim\gamma$ in the relativistic limit), with a characteristic energy scale γ_0 which is set entirely by the collisional properties of the plasma. The electric field sets the shape of the pitch distribution as well as the rate at which new runaways are produced.

3.2.2 Runaway electron losses

A number of physical mechanisms act to reduce the energy of runaway electrons, or even remove them from the plasma altogether. In addition to elastic collisions, which only redistribute some of the energy from the runaway electrons to thermal electrons, inelastic collisions also result in the production of bremsstrahlung photons [79, 80].

The helical motion around magnetic field lines results in radiation emission by all particles in the plasma. For non-relativistic particles, this radiation is known as cyclotron emission, whereas for relativistic particles such as runaway electrons, it is referred to as synchrotron radiation. Much of the cyclotron radiation emitted by thermal electrons is reabsorbed by the plasma, preventing all heat from rapidly being radiated away during normal operation [81]. Synchrotron radiation, however, shines through the plasma without any appreciable reabsorption occurring, making it an effective energy loss channel for runaways. The synchrotron radiation loss can be modelled via a radiation reaction force, taking the form [82, 83]

$$\boldsymbol{F}_{\mathrm{synch}} = -\frac{1}{\gamma\tau_{\mathrm{synch}}}\left(\boldsymbol{p}_{\perp} + p_{\perp}^{2}\boldsymbol{p}\right), \tag{3.17}$$

with the radiation reaction time scale

$$\frac{1}{\tau_{\mathrm{synch}}} = \frac{e^{4}B^{2}}{6\pi\varepsilon_{0}m_{\mathrm{e}}^{3}c^{3}}. \tag{3.18}$$

The magnitude of the force is mainly set by the perpendicular momentum of the electron, $p_{\perp}$, as well as the magnetic field strength B, both of which determine the acceleration of the particle due to the gyration. Due to the strong dependence on $p_{\perp}$, the synchrotron radiation force has a considerably larger impact on runaways with large pitch angles, causing those electrons to lose their energy faster and leading to a more beam-like distribution function.

In addition to radiation losses, runaway electrons can also lose their energy when colliding with the wall. While loss of runaway confinement may occur in a number of different ways, the mechanism that is of most interest in models of runaway dynamics is radial transport due to magnetic field stochastisation. For example, during the TQ of a disruption, the magnetic flux surfaces break up and magnetic field lines fluctuate turbulently. An electron travelling along such a magnetic field line will therefore eventually be led out of the plasma and onto the surrounding wall. Since the magnetic field line fluctuation is effectively random, the electrons undergo a random walk process. The drift velocity of the random walk will be approximately $v_r \sim (\delta B/B)v_{\|}$, where $\delta B/B$

denotes the relative magnitude of the magnetic perturbation, and the decorrelation time can be estimated as $\tau_\| = L_\|/v_\|$, with decorrelation length $L_\| \sim \pi q R_\mathrm{m}$, i.e. on the order of a poloidal transit scale length. The resulting diffusion coefficient takes the form [84]

$$D_\| \sim v_r^2 \tau_\| = \pi q R_\mathrm{m} \left(\frac{\delta B}{B}\right)^2 v_\|. \tag{3.19}$$

Experimentally, it is found that this coefficient overestimates the transport of runaway electrons, and that the transport can decrease with energy [85, 86]. To address this possibly non-trivial energy dependence, a method to evaluate advection and diffusion coefficients was developed in Ref. [87] for use in integrated runaway modelling tools, such as Dream. Knowing that the runaway electron distribution function is well described by equation (3.16) whenever the avalanche mechanism dominates runaway generation, a reduced fluid transport model can be derived with the help of these advection and diffusion coefficients [88], as was done in Paper T.

3.3 Electron kinetics in the plateau phase

After the runaway electrons have been generated in the TQ and CQ phases of the disruption, they will gradually slow down during the plateau phase. As the runaways are only weakly collisional, the slowing down occurs over a much longer time than the generation, leading to a phase in which the plasma current appears to be almost constant, hence the name “plateau phase”. Understanding the electron dynamics during the plateau phase is crucial, both for predicting the dissipation of runaway electrons, but also the duration and relative stability of the phase makes it easier to conduct measurements on the runaway electrons in current experiments, therefore allowing our models of runaway electrons to be tested and validated.

The strong dependence of the avalanche growth rate (3.13) on the electric field implies that the electric field must rapidly decrease during the CQ to keep the runaways from overtaking more energy than what is available in the system. At the same time, the electric field cannot settle at exactly zero since collisions and radiation losses will gradually dissipate the runaway current, leading the current decay to induce a compensating electric field. The electric field therefore settles close to the effective threshold value, $E_\mathrm{c,eff}$, which allows for a sufficiently slow decay of the runaway current, and remains near this value throughout the plateau [89].

Due to the relatively weak electric field $E \sim E_{\mathrm{c,eff}}$ during the plateau, the runaway electron distribution function is primarily evolving via pitch angle relaxation, the rate of which is set by the balance of the collisional pitch angle scattering and electric field acceleration. The pitch distribution of the runaways can therefore be described by the Fokker–Planck equation [55]

$$\frac{\partial f_{\mathrm{re}}}{\partial t} = \frac{\partial}{\partial \xi_0}\left[\left(1-\xi_0^2\right)\left(-\frac{m_{\mathrm{e}}cE_\parallel}{p}f_{\mathrm{re}} + \frac{\nu_{\mathrm{D}}(p)}{2}\frac{\partial f_{\mathrm{re}}}{\partial \xi_0}\right)\right], \tag{3.20}$$

where ν_{D} is the pitch angle deflection frequency. In the steady-state limit, this equation reduces to

$$\frac{\partial f_{\mathrm{re}}}{\partial \xi_0} = \frac{2m_{\mathrm{e}}cE_\parallel}{p\nu_{\mathrm{D}}}f_{\mathrm{re}}, \tag{3.21}$$

which is solved by an exponential function

$$f_{\mathrm{re}}(t,r,p,\xi_0) = F_{\mathrm{re}}(t,r,p)\frac{A}{2\sinh A}\mathrm{e}^{A\xi}, \tag{3.22}$$

where $F_{\mathrm{re}}(t,p)$ is the (undetermined) energy distribution of the runaways and $A = 2m_{\mathrm{e}}cE_\parallel/(p\nu_{\mathrm{D}})$. From numerical solutions of the Fokker–Planck equation, it is found that the pitch distribution of the runaways often follows the form (3.22) even before a steady state is reached. As shown in appendix B of Paper E, the coefficient A is in that case not a simple function of the electric field and collision frequency, but approximately approaches its steady state value as t^{-1}.

This result has proven highly useful in the interpretation of experimental synchrotron radiation measurements, both in ASDEX Upgrade (see Paper E) and JET [90, 91]. The reason for this is that synchrotron radiation is particularly sensitive to the runaway pitch distribution, while it depends to only a lesser extent on the energy distribution. Equation (3.22) is therefore in effect a theoretically well-motivated one-parameter model for the runaway pitch distribution, making it feasible to infer both the pitch and radial distributions of the runaways from experimental measurements.

A special case for which the distribution function (3.22) appears particularly well-motivated was studied in Paper E. There, a deliberately induced disruption on ASDEX Upgrade was considered, and the subsequent runaway electron beam analysed using synchrotron radiation camera images. From self-consistent simulations of the disruption, it was found that the runaway electron energy distribution function consisted of two components. Most electrons, and thus most of the runaway current, was carried by electrons in an exponentially decaying avalanche distribution. However, many of the seed runaways were merely accelerated to high energies by the induced electric field, forming a narrow and nearly Gaussian distribution at the highest electron energies. Because of their high energies, these electrons dominated the synchrotron emission, motivating the approximation of the energy distribution as a delta function in momentum, and the coefficient A as independent of energy. With this particularly simple model for the distribution function, the radial distribution of runaways could then be inferred from experimental measurements and its evolution in time studied.

Chapter 4

Radiation from runaway electrons

In present-day tokamaks, runaway electrons are usually not a major concern. In fact, the smaller plasma currents of today's tokamaks often demand significant effort if runaway electrons are to be generated and studied. However, all evidence points to the fact that runaways will be far more prevalent—and carry far greater risk—in future tokamaks. A key purpose of the mathematical models of runaway electrons is therefore to allow for predictions of their generation in future, reactor-scale tokamaks. Before the models can be applied with any confidence, they must however be thoroughly tested and validated against today's experiments to ensure that the underlying physics is adequately understood. Validation is complicated by the fact that the orders-of-magnitude variation in many observables during a disruption makes their measurement very difficult, if at all possible. Often, only a few diagnostic signals for integrated plasma parameters, such as the total plasma current, are available for comparison to the far more detailed models.

One way of obtaining more detailed information about the dynamics of runaway electrons is to measure the radiation that they emit. For example, when a runaway electron interacts with other electrons and ions, there is a chance that bremsstrahlung is emitted in the form of a highly energetic photon [92]. The measurement of hard X-rays are routinely used as an indicator of the presence of runaway electrons, as well as for probing the spatial [93, 94] and energy [95–97] distributions of the runaways. Charged particles gyrating around magnetic field lines also emit radiation, and if the particle is travelling at relativistic speeds, as run-

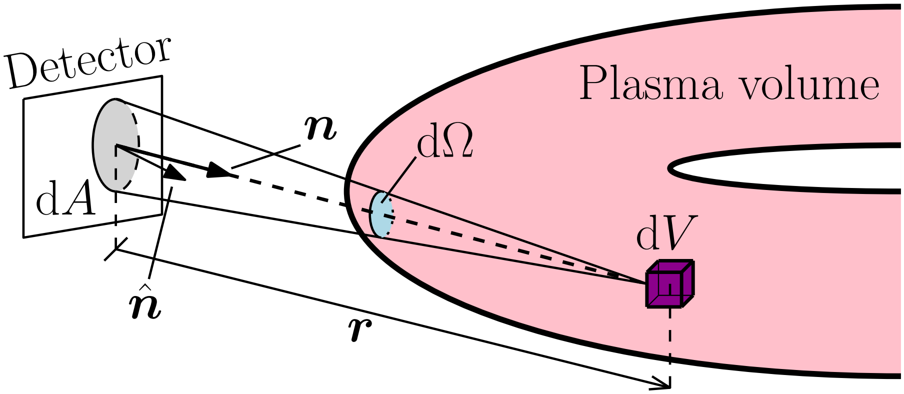

Figure 4.1: Illustration of the synthetic diagnostic setup described in Section 4.1. The synthetic diagnostic sums up the radiation coming from all volume elements dV in the plasma

away electrons usually are, this radiation is referred to as synchrotron radiation. Such radiation is routinely measured using visible- and infrared light cameras and spectrometers on tokamaks, giving information about the spatial, pitch and energy distributions of the runaways [98, 99].

The radiation emitted by runaway electrons therefore contains a wealth of information which can be used to validate models of the runaway dynamics. In this chapter we will describe the model used to simulate a bremsstrahlung or synchrotron radiation detector in the synthetic diagnostic framework SOFT, which was introduced in Paper A. We begin with a derivation of the radiation diagnostic integral, which describes the power received by a detector from a distribution of electrons, and follow this with a description of the cone approximation, which is useful for directed radiation such as bremsstrahlung and synchrotron radiation from runaway electrons. The remainder of the chapter reviews important implications of the radiation diagnostic integral, first by analysing the Green's function of a representative system, and then by studying typical radiation patterns which could be observed and their dependence on the runaway electron parameters.

4.1 Radiation diagnostic integral

The principle of a general radiation diagnostic, measuring some quantity I (which can be, for example, radiated power or number of photons), is illustrated in Fig. 4.1. Assuming that the plasma is optically thin to the radiation, we can write the total received radiation from the plasma volume V, along the line-of-sight specified by the unit vector $\boldsymbol{n}$, as

$$I_{\boldsymbol{n}}(\boldsymbol{x}_0, t) = \int_V \delta^2\left(\frac{\bar{\boldsymbol{r}}}{\bar{r}} - \boldsymbol{n}\right) \frac{\mathrm{d}I(\boldsymbol{x}, \boldsymbol{n}, t)}{\mathrm{d}V}\,\mathrm{d}V, \tag{4.1}$$

where $\delta^2(\boldsymbol{x})$ is a two-dimensional Dirac delta function, and $\bar{\boldsymbol{r}} = \boldsymbol{x}_0 - \boldsymbol{x}$ is a vector between the detector at $\boldsymbol{x}_0$ and the point $\boldsymbol{x}$ in space where radiation originates.

Typically, we are interested in the radiation seen in the entire field-of-view of the detector, or the field-of-view corresponding to a particular camera pixel, and then we must integrate over the set $\Omega_{\boldsymbol{n}}$ of all line-of-sight directions $\boldsymbol{n}$ in the field-of-view. If we integrate Eq. (4.1) over $\Omega_{\boldsymbol{n}}$ we find that

$$I = \int I_{\boldsymbol{n}}\,\mathrm{d}\Omega_{\boldsymbol{n}} = \int_V \Theta\left(\frac{\bar{\boldsymbol{r}}}{\bar{r}}\right) \frac{\mathrm{d}I\left(\boldsymbol{x}, \bar{\boldsymbol{r}}, t\right)}{\mathrm{d}V}\mathrm{d}V, \tag{4.2}$$

where the delta function has substituted $\bar{\boldsymbol{r}}/\bar{r}$ for $\boldsymbol{n}$ and given rise to a function $\Theta(\bar{\boldsymbol{r}}/\bar{r})$ that is one when $\bar{\boldsymbol{r}}/\bar{r} \in \Omega_{\boldsymbol{n}}$, and zero otherwise. In other words, the integration over $\Omega_{\boldsymbol{n}}$ makes explicit the fact that only particles situated in the detector's field-of-view can contribute to the measurement.

The amount of radiation received from an infinitesimal volume element $\mathrm{d}V$ in the plasma, by a detector with area A, occupying a solid angle Ω as seen from the emitter, is

$$\frac{\mathrm{d}I}{\mathrm{d}V} = \int_\Omega \frac{\mathrm{d}^2 I}{\mathrm{d}V\mathrm{d}\Omega}\,\mathrm{d}\Omega. \tag{4.3a}$$

Often, it is more convenient to express Eq. (4.3a) as an integral over the detector surface instead of the solid angle subtended by the detector. The surface area taken up by the solid angle $\mathrm{d}\Omega$ a distance $\bar{r}$ from the emission source is $\mathrm{d}S = \bar{r}^2\mathrm{d}\Omega$, and the normal vector of this surface is $\bar{\boldsymbol{r}}/\bar{r}$. If we let $\mathrm{d}A$ be the corresponding area of $\mathrm{d}S$ when projected onto the detector surface, with normal $\hat{\boldsymbol{n}}$, then $\mathrm{d}S = (\hat{\boldsymbol{n}} \cdot \bar{\boldsymbol{r}}/\bar{r})\mathrm{d}A$ and

$$\frac{\mathrm{d}I}{\mathrm{d}V} = \int_A \frac{\hat{\boldsymbol{n}} \cdot \bar{\boldsymbol{r}}}{\bar{r}^3} \frac{\mathrm{d}^2 I}{\mathrm{d}V\mathrm{d}\Omega}\,\mathrm{d}A. \tag{4.3b}$$

The radiation emitted from the volume element $\mathrm{d}V$, into the infinitesimal solid angle $\mathrm{d}\Omega$, is now given by the number of particles in $\mathrm{d}V$, times the amount of radiation emitted by each particle into $\mathrm{d}\Omega$:

$$\frac{\mathrm{d}^2 I}{\mathrm{d}V\mathrm{d}\Omega} = \int \frac{\mathrm{d}I(\boldsymbol{x},\boldsymbol{p},\bar{\boldsymbol{r}})}{\mathrm{d}\Omega} f\left(\boldsymbol{x},\boldsymbol{p}\right)\,\mathrm{d}\boldsymbol{p}. \tag{4.4}$$

Here, $f(\boldsymbol{x},\boldsymbol{p})$ is the electron distribution function and $\mathrm{d}I/\mathrm{d}\Omega$ describes the angular distribution of radiation emitted by each particle. Depending on which type of radiation we would like to model, we pick a suitable form for the angular distribution of radiation. For synchrotron radiation we would take it to be the total received power per unit solid angle $\mathrm{d}P/\mathrm{d}\Omega$, while for bremsstrahlung we would take it to be the differential cross-section of photon production, multiplied by the electron speed and local plasma density, to get the number of detected photons.

For completeness, we also give the combined form of the radiation diagnostic integral. Combining Eqs. (4.1)-(4.4), we obtain

$$I = \int \Theta\left(\frac{\bar{\boldsymbol{r}}}{\bar{r}}\right) \frac{\bar{\boldsymbol{r}}\cdot\hat{\boldsymbol{n}}}{\bar{r}^3}\frac{\mathrm{d}I(\boldsymbol{x},\boldsymbol{p},\bar{\boldsymbol{r}})}{\mathrm{d}\Omega} f(\boldsymbol{x},\boldsymbol{p})\,\mathrm{d}\boldsymbol{p}\,\mathrm{d}V\,\mathrm{d}A. \tag{4.5}$$

This is, in essence, the integral that the simulation tool SOFT evaluates. It serves as the starting point of the theory developed in Paper A, which transforms the set of coordinates used in Eq. (4.5) to a set more suitable for integrating along runaway orbits.

4.1.1 Tokamak geometry

Evaluation of the radiation integral (4.5) can be greatly simplified by an appropriate choice of coordinates. In this thesis, we are interested in evaluating equation (4.5) with a distribution function $f(\boldsymbol{x},\boldsymbol{p})$ satisfying the bounce-averaged Fokker–Planck equation (2.43), and the “appropriate” set of coordinates to use is therefore the same set used in chapter 2, since this will allow us to keep the approximations consistent between both equations. Just as when deriving the bounce-averaged Fokker–Planck equation in chapter 2, we therefore make three key assumptions, each of which makes the distribution function independent of one coordinate:

(i) the gyration time τ_Ω is much shorter than the transit time τ_b,

(ii) the transit time τ_b is much shorter than all other time scales over which the electron distribution evolves,

(iii) the magnetic field is axisymmetric.

In addition to these assumptions, the derivation of the bounce-averaged Fokker–Planck equation was made in the zero orbit width (ZOW) limit, assuming negligible orbit drifts and gyro radius, which we will also make here for simplicity. The ZOW limit is usually a good approximation for kinetic calculations, since the deviations from magnetic field lines are usually small, so that the errors incurred by averaging background plasma parameters over flux surfaces rather than orbits are also small. For radiation measurements, the situation may however be different. If the field-of-view of a radiation detector is small compared to the solid angle subtended by a particle orbit for the detector, even small displacements of the particles due to drifts could lead to significantly different radiation signals. For example, the radial distribution of runaways often features sharp variations, not least near the edge of the plasma. In a camera image, if the particle location is shifted due to drifts, this could cause the observed radiation pattern to be shifted by many pixels compared to the ZOW prediction, making direct comparisons between theory and experiment difficult. The fact that drifts are generally negligible in kinetic simulations, but not in radiation simulations, motivates the use of ZOW calculations of the distribution function f together with finite orbit width (FOW) calculations of the radiation the electrons emit. In the remainder of this chapter we will mainly consider the ZOW limit for the radiation, and only briefly discuss the implications of the FOW limit.

After substitution of the appropriate coordinates, equation (4.5) takes the form

$$\begin{aligned} I = \int \Theta\left(\frac{\bar{\boldsymbol{r}}}{\bar{r}}\right) \frac{\bar{\boldsymbol{r}}\cdot\hat{\boldsymbol{n}}}{\bar{r}^3} \left\langle \frac{\mathrm{d}I\left(\boldsymbol{x},\boldsymbol{p},\bar{\boldsymbol{r}}\right)}{\mathrm{d}\Omega} \right\rangle_{\zeta} f\left(r, p, \xi_0\right) \\ \times \left| p^2 \frac{\xi_0 B}{\xi B_{\mathrm{min}}} \right| \mathcal{J}\,\mathrm{d}p\,\mathrm{d}\xi_0\,\mathrm{d}r\,\mathrm{d}\theta\,\mathrm{d}\varphi\,\mathrm{d}A, \end{aligned} \tag{4.6}$$

where the gyro average $\langle\cdot\rangle_\zeta$ was defined in equation (2.18) and the configuration space Jacobian $\mathcal{J}$ in equation (2.35).

4.2 Cone approximation

One particular form of the radiation function $\mathrm{d}I/\mathrm{d}\Omega$ in equation (4.4) is found to be especially useful for the radiation emitted by relativistic runaway electrons. As illustrated in figure 4.2(a), the relativistic beaming effect will direct radiation along the velocity vector of the particle, with an angular spread that is $\sim \gamma^{-1}$, i.e. the inverse of the relativistic factor of the particle. For highly relativistic particles, which runaways often are, this means that the radiation is emitted almost exclusively along the velocity vector, motivating us to take this as an approximation. The corresponding radiation function is

$$\frac{\mathrm{d}P}{\mathrm{d}\Omega} = \frac{P\left(p,\xi\right)}{2\pi}\delta\left(\hat{\boldsymbol{v}}\cdot\boldsymbol{n}-1\right), \tag{4.7}$$

where $P(p,\xi)$ represents the total radiation emitted by the particle.

The delta function in equation (4.7) ensures that radiation will only be emitted exactly along the direction of motion $\hat{\boldsymbol{v}}$ of the particle, which must be aligned with the line-of-sight $\boldsymbol{n}$ under consideration. After applying a coordinate transformation to equation (4.7) and integrating over the gyro angle, a corresponding expression is obtained which describes the emission of the so-called guiding-centre, i.e. the centre of gyration of the particle:

$$\int_0^{2\pi}\frac{\mathrm{d}P}{\mathrm{d}\Omega}\,\mathrm{d}\zeta = P\left(p,\xi\right)\,\delta\left(\hat{\boldsymbol{V}}\cdot\boldsymbol{n}-\cos\theta_{\mathrm{p}}\right), \tag{4.8}$$

where $\hat{\boldsymbol{V}}$ denotes a unit vector in the direction of motion of the guiding-centre and $\theta_{\mathrm{p}} \equiv \arccos\xi$. The geometric interpretation of equation (4.8) is illustrated in figure 4.2(b): the guiding-centre emits radiation along the surface of a circular cone with half opening angle θ_{p}, centred on its direction of motion $\hat{\boldsymbol{V}}$; hence the name "cone approximation."

As a result of the forward-beaming of the radiation, radiation emitted by relativistic runaway electrons tends to form light patterns or *spots* in camera images. Equation (4.8) enables us to build some physical intuition about the shapes of these radiation spots. It asserts that radiation will be detected whenever

$$\hat{\boldsymbol{V}}\cdot\frac{\boldsymbol{x}-\boldsymbol{x}_0}{\left|\boldsymbol{x}-\boldsymbol{x}_0\right|} = \cos\theta_{\mathrm{p}}. \tag{4.9}$$

where $\boldsymbol{x}$ denotes the particle position and $\boldsymbol{x}_0$ the observer's position. In the ZOW limit, $\hat{\boldsymbol{V}}$ is directed along the magnetic field unit vector $\hat{\boldsymbol{b}}$, and hence the cone will sweep past the detector, roughly following magnetic field lines. Whenever the cone overlaps with the detector, radiation is registered.

If we consider a mono-velocity distribution function, with particles distributed uniformly in the radius coordinate r, then the points of space

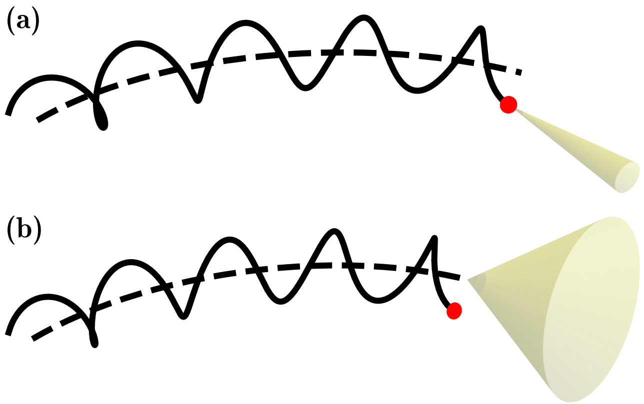

Figure 4.2: Illustration of relativistic (a) *particle* emission versus (b) *guiding-centre* emission. Several particles can share the same guiding-centre, and when the radiation of all of those particles is considered, that guiding-centre can be considered as emitting radiation in a larger cone with opening angle θ_{p} (the pitch angle of the particles). In general, the guiding-centre cone of radiation is hollow with a side thickness corresponding to the $\sim \gamma^{-1}$ angular spread of the radiation from the particle. In the cone approximation, we assume $\gamma^{-1} \ll 1$ so that the particle radiation in (a) becomes a line and the guiding-centre radiation in (b) a conical shell.

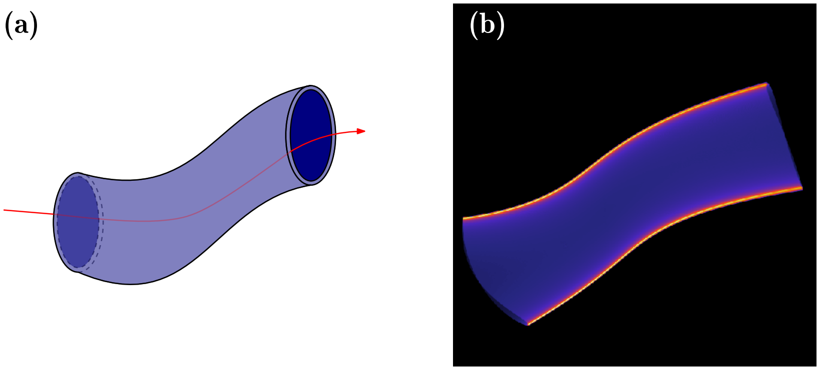

Figure 4.3: (a) Sketch of a surface-of-visibility, emphasising how it takes the shape of a twisted, hollow cylindrical shell. (b) Camera image projection of a simulated SoV. The projection shows how the edges of the observed radiation spot tend to appear brighter to an observer than the rest of the spot. This is due to the cylindrical shape of the SoV which causes lines-of-sight that are tangential to the SoV to receive much more radiation than other lines-of-sight.

satisfying equation (4.9) form a surface. This surface, which we refer to as a *surface-of-visibility* or SoV, usually takes the shape of a bent and twisted cylinder at small θ_p, and splits into two parts at larger θ_p. Figure 4.3 illustrates the appearance of a hollow, cylinder-shaped SoV. Note that it is only possible to look at the SoV from different perspectives in simulation, due to the dependence on the detector position $\boldsymbol{x}_0$ in equation (4.9). Using a camera in an experiment, it is only possible to observe the projection in figure 4.3(b).

Although a camera will always see a two-dimensional projection of the SoV, the fact that it has a three-dimensional structure has important consequences for the observed radiation pattern. In particular, this can be observed in figure 4.3(b), which shows the projection of a SoV. As is shown there, the upper and lower edges of the projection have brighter colours, corresponding to higher radiation intensity. In these points, the lines-of-sight are tangential to the cylindrical shell that constitutes the SoV, and it can be shown that if the shell is thin, those lines-of-sight will receive the most radiation. From a single point of momentum space—that is, from particles with the same energy and pitch angle—it is therefore primarily the edges of the SoV that contribute to the total detected radiation.

The basic idea behind the cone approximation—that all radiation is emitted exactly along the velocity vector of the particle—has been known and utilised since the early days of runaway synchrotron measurements. It has served as, arguably, the most important approximation for synchrotron radiation, and is the source of many of the fundamental results within the topic [100–102]. In simulations, use of the cone approximation can substantially reduce computation times, while maintaining good agreement with more complete models of the radiation, as we demonstrate in Paper A. For this reason, the cone approximation has been used in most synchrotron simulations of this thesis.

As mentioned in section 4.1.1, finite orbit width (FOW) effects are generally not negligible in synchrotron diagnostic calculations. This could be concerning for the validity of the cone approximation at higher electron energies, since, as we demonstrate in Paper E, the higher-order corrections introduced in the FOW limit can cause the gyro orbit to deviate from a perfect circle, which should similarly cause the emission cone to deviate from perfectly circular. Fortunately, the deviation of the gyro orbit from circular is small in the limit $p_{\|} \gg p_{\perp}$, which is typically satisfied by runaway electrons [103]. In the FOW limit, the cone approximation is therefore still valid, with the cone of emission being directed around the guiding-centre velocity (rather than the magnetic field line as in the zero orbit width limit). A test for the validity of the cone approximation in the FOW limit was devised and presented in Appendix A of Paper E, showing good agreement for typical values of the runaway electron momentum.

4.3 Properties of the radiation integral

In the integrand of the radiation integral (4.6), the distribution function $f(r, p, \xi_0)$ can be seen as a "source" function which describes a population that emits radiation, and which only depends on three of the seven variables to be integrated over. The other terms of the integrand may therefore be collected into a Green's function

$$G(r, p, \xi_0) = \int \Theta\left(\frac{\bar{\boldsymbol{r}}}{\bar{r}}\right) \frac{\bar{\boldsymbol{r}} \cdot \hat{\boldsymbol{n}}}{\bar{r}^3} \left\langle \frac{\mathrm{d}I\left(\boldsymbol{x}, \boldsymbol{p}, \bar{\boldsymbol{r}}\right)}{\mathrm{d}\Omega} \right\rangle_{\zeta} \left| p^2 \frac{\xi_0 B}{\xi B_{\mathrm{min}}} \right| \mathcal{J}\, \mathrm{d}\theta \mathrm{d}\varphi \mathrm{d}A, \tag{4.10}$$

so that equation (4.6) may be written

$$I = \int G(r, p, \xi_0) f(r, p, \xi_0)\, \mathrm{d}r \mathrm{d}p \mathrm{d}\xi_0. \tag{4.11}$$

Table 4.1: Simulation parameters used to generate figure 4.4 using the Soft code.

Parameter	**Value**
Magnetic field strength (on-axis)	$5\,\mathrm{T}$
Tokamak major (R_m) / minor (r_m) radius	$1.7\,\mathrm{m}$ / $0.5\,\mathrm{m}$
Radial distribution of runaways	Uniform, $f(r) = \mathrm{const}$
Safety factor	Constant, $q = 1$
Detector vertical position	$Z = 0$

The Green's function encodes the momentum dependence of the emitted radiation, as well as the geometry of the tokamak, and is a useful tool for studying the sensitivity of the measured radiation to variations in the distribution function. It is also a powerful computational tool as $G(r, p, \xi_0)$, which typically involves a series of complicated and expensive computations, can be evaluated once and then repeatedly used with (4.11) to calculate the radiation obtained from different electron populations. Such repeated evaluations of equation (4.11) arise, for example, when f rather than I is considered as the unknown. This leads to an inverse problem for which measured values of I, along with calculations of G, can be used to solve for the distribution function f [104, 105]. This technique was utilised in Papers E and I.

4.3.1 Dominant particles

For bremsstrahlung and synchrotron radiation, the Green's function $G(r, p, \xi_0)$ tends to grow rapidly with both p and ξ_0, while the distribution function $f(r, p, \xi_0)$ generally shows an opposite rapidly decreasing behaviour. The integrand in equation (4.6) is therefore usually peaked in a relatively small region in momentum space, and not necessarily where most of the particles are located. To determine which particles of a given distribution function f contribute most to a radiation measurement, we maximise the product $G(r, p, \xi_0)f(r, p, \xi_0)$, and refer to this maximum as the *dominant particle* of the system.

Figure 4.4(a) shows an example avalanche distribution function, as in equation (3.16) with $(E/E_\mathrm{c} + 1)/(Z_\mathrm{tot} + 1) = 4$ and $\gamma_0 = 18\sqrt{8} \approx 51$. In panels (b) and (c), the amount of radiation

$$F(p, \xi_0) = \int G(r, p, \xi_0) f(p, \xi_0)\,\mathrm{d}r, \tag{4.12}$$

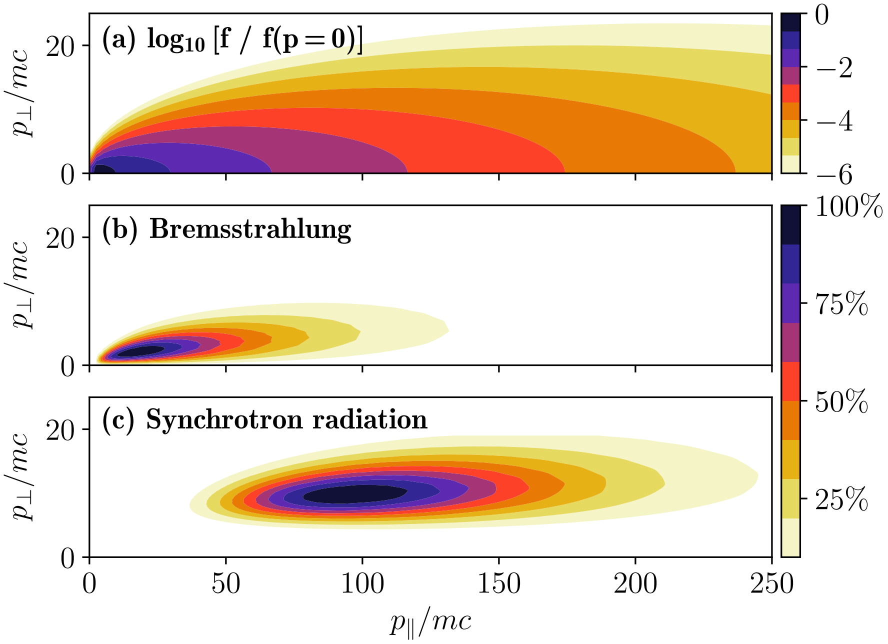

Figure 4.4: (a) A runaway electron distribution function dominated by avalanche generation and contributions to detected (b) bremsstrahlung and (c) synchrotron emission F of equation (4.12).

originating from a given region in momentum space and seen by the detector is shown for bremsstrahlung and synchrotron respectively. Figure 4.4(b) uses a Green's function G corresponding to a bremsstrahlung detector measuring photon energies in the range 511 keV-10 MeV, while figure 4.4(c) uses that of a synchrotron radiation detector measuring radiation in the wavelength range 400-800 nm. Both Green's functions have been integrated over all radii. The physical simulation parameters used to generate figure 4.4 are presented in Table 4.1.

The maxima in figures 4.4(b) and 4.4(c) correspond to the dominant particles of the distribution function. Images, spectra and other measured radiation signals from the distribution in figure 4.4(a) will have features reminiscent of signals originating purely from the dominant point of momentum space. Often, it is therefore sufficient to assume that all runaways have the same energy and pitch angle to reproduce the main features of a diagnostic signal. The particular energy and pitch angle that best matches the signal is in general, however, not representative of the actual runaway electron population. It is merely the point of momentum space that is best resolved by the diagnostic.

The location of the dominant particle in momentum space depends on both the runaway electron distribution function and the Green's function. This means that different types of radiation will be associated with different dominant particles, as evidenced in figure 4.4. It however also means that the same type of radiation, from the same distribution function, but measured at a different wavelength or originating from a different position in the device, will be associated with a different dominant particle. Therefore, multiple detectors viewing the runaways from different positions and at different radiation wavelengths may be able to probe complementary parts of the distribution function, and provide a more complete picture of the runaway dynamics.

4.4 Radiation spot shape taxonomy

Directed radiation such as bremsstrahlung and synchrotron radiation gives rise to radiation spots that can be observed using cameras. What shape the radiation spot takes depends on several parameters: the magnetic field geometry, detector properties and runaway distribution. While the relation between the radiation spot shape and the runaway pitch angle was identified already in Ref. [106], the first model for the radiation spot shape taking the magnetic field geometry into account was presented in Ref. [101]. That model accurately describes the shape of the synchrotron radiation spot from runaways with small pitch angles, but does not consider the distribution of radiation across the spot. As we show in Papers A and B, the distribution of radiation across the spot can be of great importance, particularly when the electron distribution function is taken into account and when the magnetic field is weak.

In this section we will consider SOFT simulations of camera images where the intensity recorded by each pixel corresponds to a radially integrated Green's function

$$F_{ij}(p,\xi_0) = \int G(r,p,\xi_0)f(r,p,\xi_0)\,\mathrm{d}r. \tag{4.13}$$

All simulations in this section use the simulation parameters listed in Table 4.2. Since we are concerned with the spot *shapes* due to the directed nature of bremsstrahlung and synchrotron radiation in this section, we primarily consider bremsstrahlung radiation in the cone approximation equation (4.8). This is because bremsstrahlung is independent of the magnetic field strength and particle pitch angle, meaning that for a mono-energetic population of runaways, the amount of radiation emitted from different parts of the surface-of-visibility (SoV) will be constant in a homogeneous plasma. Hence, the extent of the SoV and associated shape of the radiation spot become more apparent. In the cases where the magnetic field strength and particle pitch angle strongly influence the synchrotron radiation spot shape, this will be noted. The detector position and viewing direction is indicated in figure 4.5.

In most simulations, we use a mono-energetic and mono pitch-angle distribution function, with a uniform radial profile. This distribution function is mathematically described by

$$f(r,p,\theta_\mathrm{p}) = n_\mathrm{re}\delta\left(p-p_0\right)\delta\left(\theta_\mathrm{p}-\theta_\mathrm{p,0}\right), \tag{4.14}$$

where n_re is the radial density of runaway electrons, and p_0 and $\theta_\mathrm{p,0}$ denote the momentum and pitch-angle of all the runaways. Note that we suppress the label "(0)" on all parameters in this section for brevity. It is understood that all particle parameters are specified at the point of minimum magnetic field along the particle's orbit. Since the density of runaway electrons appears multiplicatively in the distribution function, and hence also in all radiation quantities, we normalise the simulated radiation quantities so that they do not depend on n_re.

Table 4.2: Simulation parameters used in section 4.4, unless otherwise noted.

Parameter	**Value**
Magnetic field strength (on-axis)	$2\,\mathrm{T}$
Tokamak major (R_m) / minor (r_m) radius	$1.7\,\mathrm{m}$ / $0.5\,\mathrm{m}$
Safety factor	Constant, $q = 1$
Detector vertical position	$Z = 0$
Runaway electron energy	$50m_ec^2 \approx 25\,\mathrm{MeV}$
Runaway electron pitch angle	$0.15\,\mathrm{rad}$

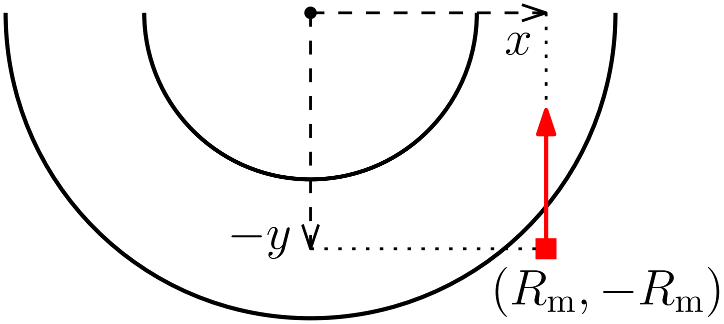

Figure 4.5: Detector setup in the simulations of this section. The detector, denoted by the red square, is located at $(x, y) = (R_\mathrm{m}, -R_\mathrm{m})$ in the midplane, where R_m is the tokamak major radius (see Table 4.2 for numerical value). It is viewing the plasma tangentially, as indicated by the red arrow.

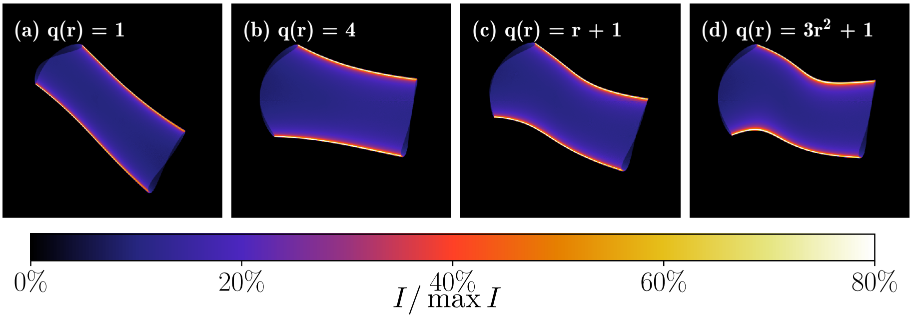

Figure 4.6: **Safety factor**. Simulated radiation images in four magnetic fields with different forms for the safety factor $q(r)$, where r is the minor radius normalised to the edge minor radius value. To emphasise the shape of the spot, the colour scale has been chosen such that white corresponds to 80% of the maximum value in any pixel of each image.

4.4.1 Magnetic field and detector placement

Both the magnetic field and detector position strongly influence the observed radiation spot shape. For the magnetic field, there is primarily one parameter influencing the spot shape. This parameter is the magnetic field safety factor q, which is a measure of how twisted the tokamak magnetic field is—it is defined as the number of toroidal turns a magnetic field line makes per poloidal turn. The safety factor determines the inclination of the radiation spot against the horizontal, as illustrated in figure 4.6. As a consequence, non-uniform safety factors cause the inclination of the radiation spot to vary, as is apparent in figures 4.6(c) & (d). In Ref. [107], the inclination angle β_{inc} between the synchrotron spot and the horizontal was related to the safety factor q, particle-detector distance D and tokamak major radius R_{m} through

$$\tan\beta_{\text{inc}} \approx \frac{D}{q(r)R_{\text{m}}}, \tag{4.15}$$

in the small pitch angle limit. Note that the radial dependence of the safety factor appears here, giving the inclination angle β_{inc} a radial dependence as well.

The magnetic field strength can also indirectly influence the observed radiation spot shape by affecting the amount of radiation emitted at different major radii. Therefore, the effect of magnetic field strength on synchrotron radiation spots can be significant, while it does not affect bremsstrahlung spots. In contrast to the safety factor, the magnetic field strength alone does not alter the geometric condition for which radiation is detected, but rather changes the distribution of radiation intensity across the radiation spot. The intensity distribution however also depends on the detector spectral range and particle momentum, and hence we postpone a discussion of this effect to the next section, where the spot shape dependence on particle parameters is discussed.

The detector properties which primarily influence the radiation spot shape are the vertical position of the detector as well as its radial distance to the plasma. The toroidal symmetry of the tokamak means that a rotation of the detector in the toroidal direction around the device will not affect the radiation spot shape. Also, since the orientation of the detector only enters through the geometric factor $\boldsymbol{n}\cdot\hat{\boldsymbol{n}}$ in equation (4.5), the orientation will be unimportant as long as the detector is not nearly-perpendicular to the incoming radiation.

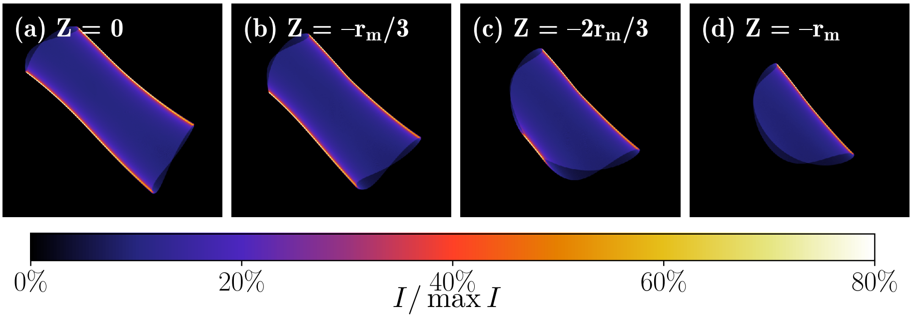

Figure 4.7: **Camera vertical placement**. Simulated radiation images with the camera located at four different heights. The height $Z = 0$ corresponds to the midplane, and r_{m} denotes the tokamak minor radius. The spot changes similarly when the detector is moved in the opposite vertical direction. To emphasise the shape of the spot, the colour scale is chosen such that white corresponds to 80% of the maximum value in any pixel.

Moving the detector along the vertical direction will alter the spot shape as shown in figure 4.7. Positioning the detector in the midplane will ensure that all particles within the detector field-of-view are visible to the detector, regardless of which flux surface they are on, or what their pitch angles are. If the detector is offset from the midplane, however, particles with small pitch angles located close to the magnetic axis will no longer radiate towards the detector. This is because radiation is emitted with an angle approximately equal to the pitch angle θ_{p} to the magnetic field lines. Close to the magnetic axis, magnetic field lines are directed almost entirely in the toroidal direction, meaning that at a distance D from the particle, radiation will be spread $\sim D\theta_{\mathrm{p}}$ from the midplane in both vertical directions. Particles with $\theta_{\mathrm{p}} < Z/D$, located close to the magnetic axis, can therefore not be observed by a detector that is offset from the midplane. The vertical dependence of the synchrotron spot shape was experimentally validated in Paper D.

The same argument can be used to reason about how the spot shape is affected when the detector is moved radially away from or towards the plasma. Let Z now instead denote the vertical position of the particle. The largest value of Z such that the particle emits at and is visible to the detector is then $Z \approx D\theta_{\mathrm{p}}$. Since the surface-of-visibility is made up of the particles that emit towards the detector, the vertical extent Δz of the radiation spot must therefore be $\Delta z \propto D\theta_{\mathrm{p}}$. Consequently, the vertical extent of the radiation spot must increase when the detector is moved further away from the plasma, similar to how it is affected by larger particle pitch angles. As is revealed by equation (4.15) however, increasing the distance D between the detector and plasma also affects the inclination of the radiation spot relative to the horizontal, since the angles between the lines-of-sight of the detector and the magnetic field change.

4.4.2 Runaway electron properties

Although the magnetic field and detector setup are important for the shape of the radiation spot, the question of primary interest to anyone studying the radiation from runaway electrons is how the motion and location of the runaways are reflected in the radiation spot. The position and velocity of an electron are fully specified by six parameters, but as discussed in Paper A and section 4.1.1, these can be reduced to a set of just three parameters in a tokamak: the outermost major radius visited by the particle along its orbit r, the electron pitch angle θ_{p} and the electron momentum p. For a given observation setup, the radiation spot characteristics can therefore at most depend on these three parameters.

Pitch angle

The first runaway parameter we consider is the pitch angle, $\theta_{\mathrm{p}} = \arccos\xi_0$. The effect of this parameter on the synchrotron spot shape has been discussed extensively in the runaway synchrotron literature [101, 102, 107], precisely because the spot shapes observed in synchrotron images are particularly sensitive to the pitch angle. As is shown in figure 4.8, at small pitch angles, the radiation spot is a thin stripe. As the pitch angle grows, the line becomes thicker and the spot grows in size in the vertical direction. The surface-of-visibility, described in section 4.2, roughly takes the shape of a cylinder in figures 4.8(a)-(e). At larger pitch angles, the vertical expansion of the spot with pitch angle slows down, and the surface-of-visibility begins to open up into two separate oval surfaces, which is best illustrated by figure 4.8(h). At pitch angles beyond $\theta_{\mathrm{p}} = 0.46\,\mathrm{rad}$, the shapes of the two oval surfaces change little, but rather they move away from each other. In the view from above the tokamak in figure 4.9, we see that the two surfaces move in opposite toroidal directions. If this behaviour continues as the pitch angle increases, we would expect one of the surfaces to eventually disappear

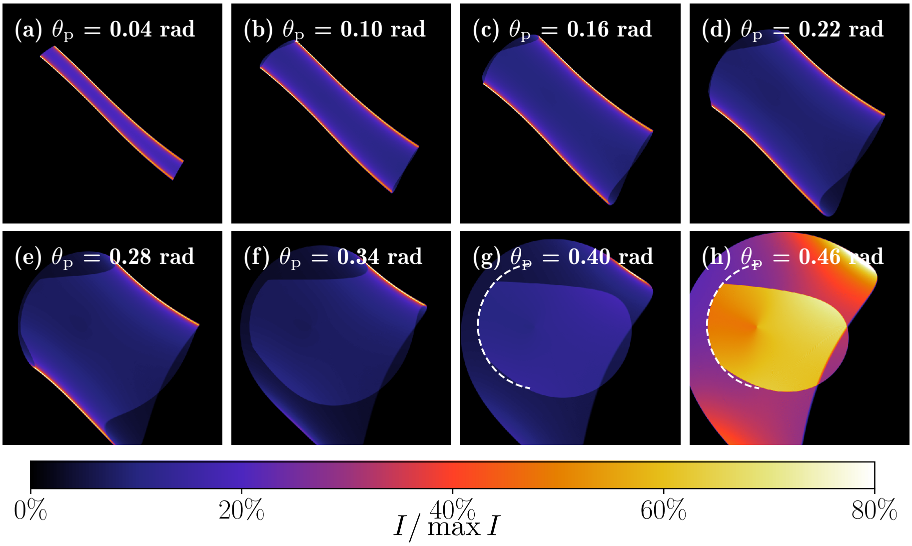

Figure 4.8: **Pitch angle.** Simulated radiation images showing how the pitch angle affects the radiation spot shape. A larger pitch angle roughly corresponds to a larger vertical extent up until some threshold pitch angle, at which point two separate spots appear and move away from each other. The dashed white lines in (g) and (h) indicate the inner part of the tokamak wall, which blocks out part of the spot. To emphasise the shape of the spot, the colour scale has been chosen such that white corresponds to 80% of the maximum value in any pixel.

behind the central column of the tokamak, and this is indeed what happens. In fact, this effect is already visible in figures 4.8(h) and 4.9(b), where the central column hides the leftmost part of the smaller spot (corresponding to the upper spot in figure 4.9(b)).

Radial location

The next parameter we consider is the maximum radial location of the particle along its orbit. If we only launch particles from a discrete set of radii, we obtain images such as those in figure 4.10. Since guiding-centres approximately follow magnetic field lines, each band of radiation in each of figures 4.10(a)-(h) originates from particles on the same flux surface. At small pitch angles, each flux surface gives rise to two bands of radiation—one to the right of the magnetic axis, and one to the left. The magnetic axis is located at the point which all bands of

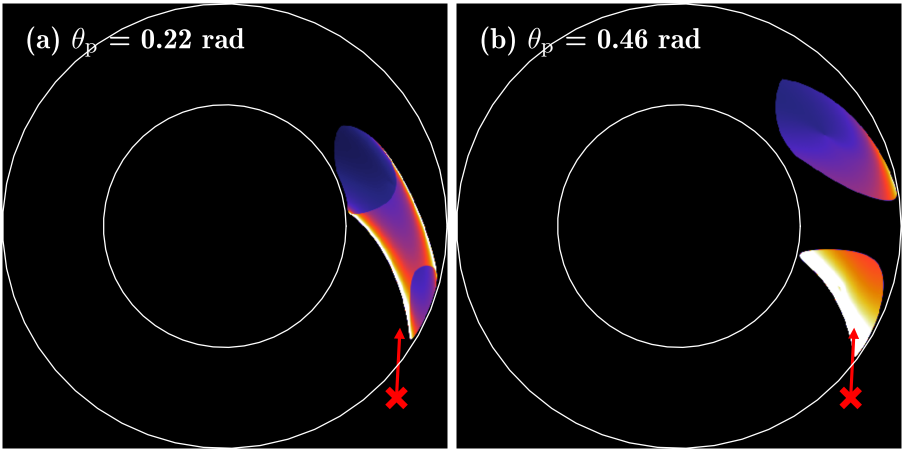

Figure 4.9: Top view of the tokamak, showing the origin of the radiation at (a) $\theta_\mathrm{p} = 0.22\,\mathrm{rad}$ (corresponding to figure 4.8(d)) and (b) $\theta_\mathrm{p} = 0.46\,\mathrm{rad}$ (corresponding to figure 4.8(h)). The camera position is indicated by the red cross, with its viewing direction designated by the red arrow. At larger pitch angles, the radiation originates from two distinct regions of space which gradually move away from each other, as exemplified in (b).

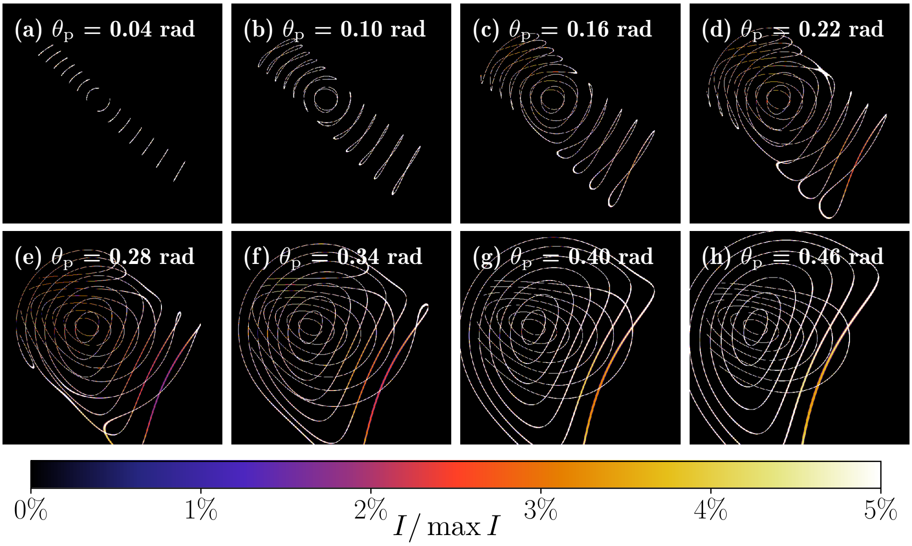

Figure 4.10: **Radial location.** Each ribbon in these images consists of radiation corresponding to a single point of the Green's function $G(r, p, \xi_0)$ of equation (4.10), for all of the pixels considered. The radii r in which these ribbons have been evaluated are distributed uniformly between 6 and 48 cm. For comparison with the spots of figure 4.8, the pitch angle is varied in each of subfigures (a)-(h). To emphasise the shape of the spot, the colour scale has been chosen such that white corresponds to 5% of the maximum value in any pixel.

radiation appear to encircle, something which is particularly noticeable in figures 4.10(b)-(d). At larger pitch angles, the bands of radiation split up and join with the corresponding bands at the same radius on the other side of the magnetic axis, as is particularly apparent in the transition between figures 4.10(c)-(g).

It is also interesting to note that each pair of radiation bands in figure 4.10 corresponds to a single point of the Green's function $G(r, p, \xi_0)$. As implied by equation (4.11), any radiation image will therefore be a linear superposition of such bands, each weighted with the corresponding value of the runaway electron distribution function.

Energy

The final phase space parameter which the radiation spot may depend on is the energy of the particle, or equivalently, its momentum p. As

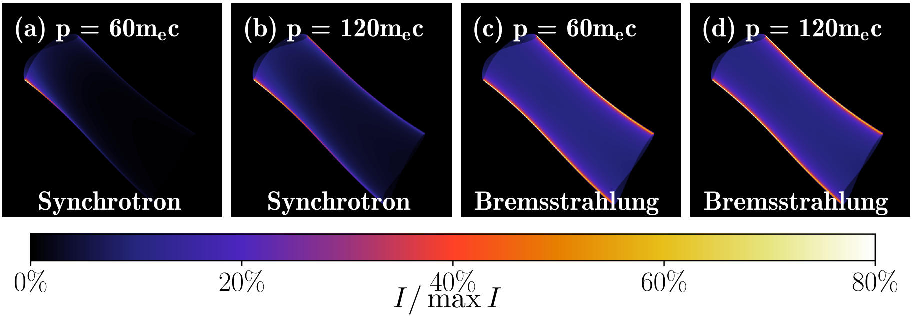

Figure 4.11: **Energy.** While the overall spot shape is not affected by the energy of the particle, the amount of emitted synchrotron radiation becomes more strongly dependent on magnetic field strength at low energies. Since bremsstrahlung is independent of the magnetic field, its radiation spot shape shows no energy dependence. All images were generated in a magnetic field with $B = 5\,\mathrm{T}$ on-axis. The camera spectral range was $\lambda \in [400, 800]\,\mathrm{nm}$ in the synchrotron case. To emphasise the shape of the spot, the colour scale has been chosen such that white corresponds to 80% of the maximum value in any pixel.

it turns out, the radiation spot shape does not in general depend on p in the ZOW limit. This is evidenced by the condition for radiation to reach the detector in the ZOW limit, equation (4.9), which is completely independent of the energy of the particle.

Despite this, the synchrotron spot shape can depend sensitively on the particle energy, something which was noted in Paper B. There, it was shown that due to the strong magnetic field dependence of the synchrotron radiation, combined with the necessarily finite spectral range of all synchrotron cameras, the amount of synchrotron radiation received from a particle at major radius R is

$$P_{\mathrm{synch}} \propto \exp\left[-\left(\frac{R}{R_{\mathrm{c}}}\right)^{3/2}\right]. \tag{4.16}$$

The critical radius R_{c} can be interpreted as the major radius length scale over which the synchrotron intensity varies significantly, and it scales as $R_{\mathrm{c}} \propto \sqrt[3]{p^2(1+p^2)}$, where p is normalised to the electron rest mass $m_e c$. It corresponds to the location in the tokamak where, for a given particle energy and pitch angle, the magnetic field is sufficiently strong for the synchrotron radiation spectrum peak to lie within the observing camera's spectral range. Note that equation (4.16) is valid only in the limit where the peak of the synchrotron spectrum lies at much longer wavelengths than the camera's spectral range, which is generally the case for visible-light cameras in today's tokamaks.

Due to the strong exponential dependence on R when $R_\mathrm{c} \ll R_\mathrm{m}$ in equation (4.16), synchrotron radiation is often mainly observed on the high field side in typical scenarios (such as in DIII-D, which has $B = 2.2\,\mathrm{T}$ on-axis under typical operating conditions). The characteristic radius R_c determines the sensitivity to R—the larger R_c is (corresponding to higher particle energies), the more evenly the radiation is distributed between the low- and high field sides of the tokamak. An example of this is shown in figures 4.11, where in figure 4.11(a) only some radiation is seen on the left side of the image, corresponding to the high field side. At twice the particle energy, in figure 4.11(b), most of the radiation spot is visible. For comparison, the corresponding bremsstrahlung emission is also given in figures 4.11(c)-(d), showing that the bremsstrahlung spot shape is independent of p.

The energy dependence can give rise to synchrotron radiation spot shapes that are vastly different from the cylindrical and oval spot shapes exemplified in figures 4.6-4.11 when the runaway electron distribution function is taken into account. When the energy of the runaways is low, so that most radiation is emitted at wavelengths that are much longer than the camera's spectral range, contributions from the high field side dominate. When the pitch angle distribution of the particles is taken into consideration, the radiation spot will have a more diffuse pattern. One example of this is shown in figure 4.12, where all particles have the same energy, but are distributed in pitch angle according to

$$f(\theta_\mathrm{p}) \propto e^{C\cos\theta_\mathrm{p}}, \tag{4.17}$$

with $C = 70$. As is shown in figure 4.12(a), the synchrotron spot takes a crescent-like shape at low energies, while at higher energies it is possible to identify the spot shape as similar to the cylindrical shape seen in, for example, figure 4.8.

It should be mentioned that for bremsstrahlung, even though the energy does not affect the radiation spot shape, the amount of emitted radiation does depend on energy. Since the runaway pitch-angle distribution typically varies with energy, the runaway electron energy distribution will always matter for the resulting radiation spot.

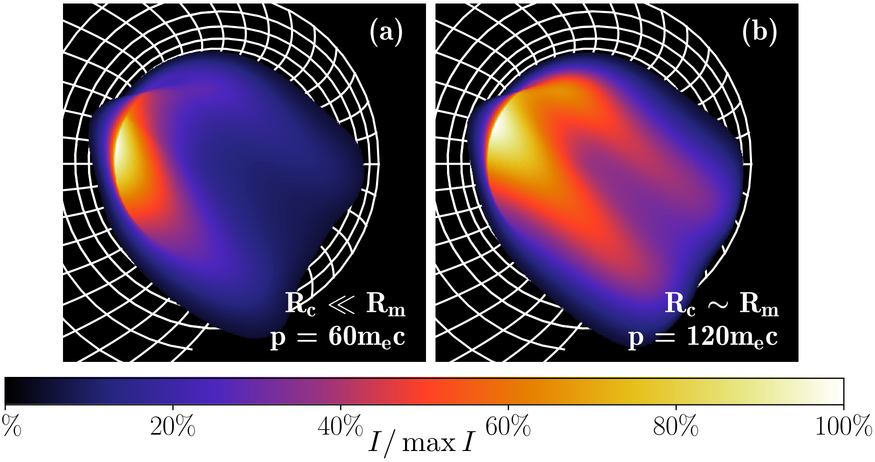

Figure 4.12: **Energy.** Synchrotron radiation images at two different energies, with particles distributed in pitch angle according to equation (4.17). In such scenarios, the synchrotron radiation spot can take a crescent-like spot shape as in (a). At higher energies, such as in (b), the radiation is distributed more evenly across the spot, and it again resembles a cylinder, as in for example, figure 4.8. The white contour lines indicate the location of the circular tokamak wall. Note that the on-axis magnetic field strength was set to $B = 5\,\mathrm{T}$ for this simulation.

Chapter 5

Concluding remarks

Runaway electrons pose a severe threat to future tokamak reactors and it is essential that their potential to do harm is mitigated or, if possible, altogether avoided. Current research efforts are geared towards developing robust avoidance and mitigation schemes for upcoming next-generation experiments such as ITER and SPARC, and this requires accurate models of the runaway dynamics. The intricate dependence and rapid variation of many background plasma parameters during a disruption, such as temperature and electric field, means that any reliable model of the runaway generation must account for the evolution of the background plasma. It is also crucial that the model gives clear predictions for already existing experiments, and that these predictions be validated against experimental measurements.

The aim of this thesis has been to develop a framework for the implementation and validation of runaway electron models. It has resulted in two numerical codes which enable simulations of the generation and observation of runaway electrons: the DREAM code provides a range of models for simulating the generation and evolution of runaway electrons in dynamic tokamak scenarios, while the SOFT code facilitates the simulation of the response of various radiation diagnostics to the runaway electron population calculated with the former code. In what follows, a brief summary of the appended papers is given, followed by a discussion about the broader context of the work and its implications for future research on the topic.

5.1 Summary of papers

The papers included in this thesis can broadly be placed into two categories, namely development of modelling tools (to which Papers A, B and G belong) and model application and validation (to which Papers C, D, E and F belong). The former three introduce the synthetic diagnostic framework SOFT and the runaway electron generation framework DREAM, while the latter papers use these codes to analyse experimental and theoretical scenarios.

In Paper A, the synthetic diagnostic framework SOFT was first introduced. It arose from a need to quantitatively study camera images of synchrotron radiation obtained in experiments, although as exemplified in the paper, the framework could also be used to study signals from other radiation diagnostics, such as spectrometers. The paper starts from the radiation diagnostic integral and reformulates it in terms of guiding-centre orbits, allowing simulations to be run for any axisymmetric magnetic field geometry, and in a computationally efficient manner. With the general framework established, a number of numerical studies proceeded, leading to the following key findings:

(i) The *cone model* is a good approximation to use for highly directed radiation, such as synchrotron radiation.

(ii) Camera images from SOFT agree qualitatively with previous, more approximate analytical results [101, 107] when the particle pitch angle is small.

(iii) The radial distribution of the runaways greatly impacts synchrotron radiation camera images.

This study was later followed up **in Paper B**, which extended the SOFT framework with a bremsstrahlung model and provided further details on the nature of directed radiation in general, and synchrotron radiation in particular. It was in Paper B that the concept of *surface-of-visibility* was introduced, providing an explanation for the separation of a synchrotron radiation spot into two spots when the particle pitch angle is large. The paper also provided a detailed explanation of the strong scaling of the measured radiation power with magnetic field strength found in experimental synchrotron images, which is enhanced by the fact that detectors only observe a finite range of wavelengths. Simulations of synchrotron and bremsstrahlung diagnostics in the DIII-D tokamak were considered in the paper, using a distribution function calculated with CODE [108, 109].

The SOFT code was subsequently applied in a series of papers, starting with Paper H and Paper I, eventually leading up to **Paper C** in which it was used to simulate the Motional Stark Effect (MSE) diagnostic of the Alcator C-Mod tokamak. The MSE diagnostic is typically used together with a perpendicular beam of injected neutrals to measure the plasma current density during normal operation, but as demonstrated experimentally in Paper C, it can also be used to directly measure the polarisation of synchrotron emission from runaway electrons. A model for a polarisation filter capable of separating light into its constituent Stokes parameters [110] was derived and implemented in SOFT. Analysis of polarised synchrotron emission subsequently conducted revealed a bifurcation in the measured polarisation angle as the runaway electron pitch angle was varied in simulations, suggesting a method for measuring the pitch angle of the runaways.

Paper D reported on observations of synchrotron radiation in the TCV tokamak while the plasma was intentionally translated vertically across the camera view. The measurements obtained validated predictions made in Paper A with the SOFT code for the dependence of the observed synchrotron spot on the camera vertical position. Additionally, the energy and pitch angle of the dominant particle were estimated and compared to predictions from a kinetic model accounting for collisions and electric field acceleration. Remarkably, the estimated parameters differed greatly from the calculated ones, corresponding to orders of magnitude differences in some plasma parameters, with the pitch angle estimated at an unusually high value of 0.5 rad. Fast radial transport was suggested to explain the differences in estimated and calculated runaway energy, while high-frequency kinetic instabilities were proposed as an explanation for the anomalously large pitch angles. Paper Q later also proposed strong pitch angle scattering due to the magnetic ripple as a potential explanation for both the differences in energy and pitch angle. The ripple pitch angle scattering should mainly affect particles near the resonant energy, which in TCV coincided with the $p \approx 50 m_\mathrm{e} c$ energy estimated from synchrotron images for the runaways that dominated synchrotron emission.

In Paper E, coupled simulations with the fluid code GO and kinetic code CODE were used to provide SOFT with a time-evolving distribution function that could be compared with experimental measurements of synchrotron radiation in the ASDEX Upgrade tokamak. The model constructed for the runaway generation assumed an instantaneous TQ in which a seed of fast electrons is born, assumed to be radially uniform, and which was manually scaled to match the measured runaway plateau current after avalanche multiplication. The background plasma and runaway generation was then evolved self-consistently through the CQ and plateau phases. The evolution seen in simulated synchrotron images was found to qualitatively resemble that observed in experiment, although a more tailored seed radial distribution was speculated to greatly improve the quantitative agreement.

The runaway electron simulations of Paper E also suggested a straightforward evolution of the runaway distribution function in the disruption. During the CQ, the seed electrons would quickly be accelerated to high energies where they would drive avalanche multiplication, leading to a final distribution function which mostly resembles an avalanche distribution, but with a "bump" of remnant seed electrons occupying the highest energies. Since the most energetic particles will typically dominate synchrotron emission, this motivated the approximation of the runaway distribution as a delta function in energy, and as $f(\xi_0) \sim \mathrm{e}^{C\xi}$ in pitch, for the purpose of constraining the radial distribution of the electrons from synchrotron camera images. Using a regularised inversion technique, the time evolution of the runaway radial distribution could be determined and shown to expand radially during a sudden transition of the synchrotron spot shape.

After a series of papers focused on synchrotron radiation and the validation of runaway electron models, attention was turned towards the development of models for runaway electron generation. In recent years, the understanding for the fundamental principles of runaway generation in tokamak disruptions has greatly improved and lead to the development of a number of advanced tools and models. **In Paper G**, our aim was therefore to bring together the state of the art of runaway generation models into a single framework. The resulting code, named DREAM, combines 1D fluid models for the background plasma with either 1D fluid, 1D1P or 1D2P bounce-averaged kinetic models for the electrons. The electrons can be divided into up to three distinct populations based on their energies, and each population can be evolved using either a fluid or kinetic model, enabling fast simulations. This also allows a runaway electron distribution function to be calculated in simulations where the bulk and mildly superthermal electrons are treated using fluid models, providing more detailed predictions of the electrons which can be used to calculate e.g. synthetic bremsstrahlung and synchrotron radiation signals.

In Ref. [63], a two-temperature model for electrons in tokamak disruptions was first introduced, which was also implemented and further developed in Dream. The model considers electrons to exist in one cold and one hot population at the onset of the disruption. The cold population is then assumed to remain in thermal equilibrium throughout the disruption, while the hot population, which is evolved using a kinetic equation expanded in the superthermal limit, partly thermalises with the cold electrons, and partly provides a seed of runaway electrons. Since collisions dominate the dynamics for $p < p_\mathrm{c}$, where p_c denotes the critical momentum for runaway acceleration, and since the hot electrons are initially in thermal equilibrium, the hot electron distribution function will remain close to isotropic during the disruption. This motivated a further reduction in Paper G of the kinetic equation, by averaging the equation over the pitch coordinate ξ_0. The resulting equation, which has one spatial and one momentum dimension, provides a new, computationally efficient and accurate model for the hot-tail runaway mechanism.

To verify the correctness of the code, a number of special scenarios were considered which could also be studied using the established codes Code and Go, yielding only small deviations which could be explained by the finite precision of the solution and the fact that some models have been improved in Dream compared to Go. By comparing Dream simulations using different models for the electrons in a disruption scenario, it was revealed that the choice of electron temperature model could have a significant impact on the resulting dynamics.

Finally, in Paper F, the radial transport of fast electrons during an idealised ITER thermal quench was studied theoretically using Dream. As impurities are inserted into the plasma, MHD instabilities are expected to grow and cause magnetic flux surfaces to break up, leading to significant radial transport of particles and heat. Employing a self-consistent treatment of these losses, Using the parallel transport model derived in Ref. [84], we scanned the magnetic field perturbation amplitude, $\delta B/B$, and the density of injected neon to find the resulting runaway electron seed current after the TQ. To avoid excessive runaway currents in the plateau, seed currents must be limited to a value which depends on the pre-disruption plasma current, which was found to set an upper limit on the amount of injected neon. Similarly, to avoid excessive heat transport to the wall, the magnetic perturbation amplitude must remain below an upper limit. With these limits accounted for, it was found that combinations of magnetic perturbation amplitudes and neon densities exist in both the standard ITER scenario, as well as modified scenarios, such that both safety limits are respected. This nuances earlier results in Ref. [111], which did not account for the fast electron transport, and which predicted intolerably large runaway currents.

The simulations in Paper F also provided insight into the runaway generation and overall TQ dynamics in the ITER scenario. In the simulations, the thermal collapse proceeded gradually from the edge to the core of the plasma. When the temperature dropped, an electric field was quickly induced locally which accelerated electrons. Due to the fast temperature drop near the edge, most runaway electrons were produced there, leading to hollow runaway current profiles. Transport primarily acts to remove fast electrons from the plasma and thus reduce the runaway current, but was also found to enhance the runaway current under certain circumstances. When the TQ was relatively slow, hot electrons from the core of the plasma could be transported towards the edge where they would be accelerated by the induced electric field, contributing to an enhanced seed current via a previously unidentified "transport hot-tail" mechanism.

5.2 Outlook

The overarching goal of present-day runaway electron and disruption studies is to provide sufficient input to the design of robust disruption mitigation systems for future tokamaks. In this thesis we have developed numerical tools and methods for simulating runaway electrons and their radiation, which can be used to conduct both interpretative simulations of experiments, as well as predictive simulations of proposed disruption mitigation schemes. While our work significantly advances our ability to model and experimentally diagnose runaway electrons, work remains on validating our models in the context of tokamak disruptions, as well as with evaluating proposed disruption mitigation systems.

Among the more pressing questions remaining is that of whether our models can robustly predict the runaway electron generation and evolution during disruptions in present-day experiments. While several authors have validated isolated aspects of runaway electron models [74, 108, 112, 113], the validation of self-consistent disruption models remains limited [114, 115]. Such validation should utilise as many plasma signals as possible, but among the key signals to compare will be the evolution of the plasma current and synchrotron radiation. The ultimate goal should be to have a model which, given only the pre-disruption state of the plasma, can accurately predict the runaway generation in multiple existing tokamaks.

Further theoretical verification is also needed of the superthermal model for the hot-tail generation originally described in Ref. [63] and implemented in DREAM. In the model, hot-cold and hot-hot electron collisions are neglected, allowing a linearised test-particle collision operator to be used. As argued in Refs. [13, 63], this should be a good approximation when the density of cold electrons is greater than that of hot electrons. However, in cases where the impurity deposition is slow or comparable to the thermal quench time, this assumption may not be satisfied. In that case a non-linear collision operator may be needed to accurately calculate the production of runaways via the hot-tail mechanism [42]. Standalone solvers for the Fokker–Planck equation utilising such a collision operator have been described previously in Refs. [116, 117], but the dynamical nature of tokamak disruptions requires the non-linear collision operator to be adopted into a self-consistent disruption simulator, such as DREAM, where background plasma parameters essential to the hot-tail generation, such as temperature and electric field, are evolved self-consistently along with the runaway electrons.

A number of gaps also remain in the physical models implemented in DREAM and similar self-consistent disruption simulators. Perhaps the most significant gap is that the radial transport of particles and heat is not calculated self-consistently along with the rest of the background plasma. While advances have been made in incorporating radial transport in one-dimensional fluid models for runaway electrons [87, 88], the transport coefficients still require external calculations. The transport is particularly important during the thermal quench, where MHD instabilities typically break up magnetic flux surfaces and give rise to significant turbulent transport, and, as shown in Paper F, play an important role in the formation of the hot-tail seed. Since the transport arises due to the break-up of magnetic flux surfaces—an inherently three-dimensional process—it will not be possible to calculate the transport self-consistently from first-principles in DREAM. By carefully studying the process in more detailed 3D MHD simulations, it might however be possible to construct a reduced or empirical model which allows the transport to be evolved self-consistently with the rest of the plasma. In case even this approach turns out to be insufficient to accurately describe the thermal quench, it would be necessary to study such effects using 3D MHD codes, including the effect of runaways [118, 119]. Codes such as DREAM could support this endeavour by identifying which runaway electron generation models are most accurate and suitable for implementation in the 3D MHD codes, and could help in verifying the correctness of such more complete models.

Another gap in the physics models of tools such as DREAM is the lack of treatment of vertical displacement events (VDE). The position of the plasma inside the electrically conducting vacuum vessel will impact the induced electric field, as will the scraping-off of runaway electrons on the plasma facing components, both of which could significantly affect the generation rate of runaway electrons [120]. A circuit-model which could potentially be integrated into a code such as DREAM was presented in Ref. [121]. An even more accurate method for treating the VDE would be to solve the Grad-Shafranov equation for the MHD equilibrium self-consistently with the rest of the DREAM equation system [122].

Finally, a topic which has not been addressed in this thesis, but which could be studied using a tool such as DREAM, is that of startup runaways. The successful initiation of a plasma discharge is absolutely essential for the operation of tokamaks, and it involves providing sufficient heat to the forming plasma for it to fully ionise and establish stable confinement. In present-day tokamaks, prescriptions for how to initialise plasma discharges have often been developed via trial-and-error. Initiation of plasmas in the larger tokamaks of the future will however need to be guided by simulations, and several studies have been conducted, using self-consistent calculations, to simulate the burn-through phase of existing, as well as future, tokamaks [123, 124]. Due to the low densities and strong electric fields usually required for successful plasma initiation, runaway electrons could potentially arise. The presence of runaway electrons would alter the discharge properties and could lead to the plasma initiation failing [125]. The physical models used to study tokamak burn-through are largely the same as those used to study tokamak disruptions, meaning that a tool such as DREAM could also be used to explore the generation of runaway electrons in startup scenarios. This could be helpful in determining whether startup runaways will be of concern to future tokamak reactors, such as ITER, and could provide insights into how startup runaway electrons could be avoided.

References

[1] IPCC. *Climate Change 2021: The Physical Science Basis. Contribution of Working Group I to the Sixth Assessment Report of the Intergovernmental Panel on Climate Change.* Cambridge, United Kingdom and New York, NY, USA, 2021. URL: `https://www.ipcc.ch/report/ar6/wg1/`.

[2] International Energy Agency. *Data & Statistics. Explore energy data by category, indicator, country or region.* Oct. 24, 2021. URL: `https://www.iea.org/data-and-statistics/data-browser/?country=WORLD&fuel=Energy%20consumption&indicator=TotElecCons`.

[3] S. Collins, J. P. Deane, K. Poncelet, E. Panos, R. C. Pietzcker, E. Delarue, and B. P. Ó Gallachóir. "Integrating short term variations of the power system into integrated energy system models: A methodological review". *Renewable and Sustainable Energy Reviews* **76** (2017), pp. 839–856. DOI: `10.1016/j.rser.2017.03.090`.

[4] International Energy Agency. *World Energy Outlook 2018.* Paris, 2018. URL: `https://www.iea.org/reports/world-energy-outlook-2018`.

[5] S. Cowley. "The quest for fusion power". *Nature Physics* **12** (May 2016), pp. 384–386. DOI: `10.1038/nphys3719`.

[6] A. Gibson and the JET Team. "Deuterium–tritium plasmas in the Joint European Torus (JET): Behavior and implications". *Physics of Plasmas* **5** (5) (1998), pp. 1839–1847. DOI: `10.1063/1.872854`.

[7] ITER Website. *What is ITER?* Nov. 9, 2021. URL: `https://www.iter.org/proj/inafewlines#1`.

[8] K. Ikeda. "Progress in the ITER Physics Basis". *Nuclear Fusion* **47** (6) (June 2007). DOI: `10.1088/0029-5515/47/6/e01`.

[9] H. R. Koslowski. “Operational Limits and Limiting Instabilities in Tokamak Machines”. *Fusion Science and Technology* **61** (2T) (2012), pp. 96–103. DOI: `10.13182/FST12-A13496`.

[10] V. D. Pustovitov, G. Rubinacci, and F. Villone. “On the computation of the disruption forces in tokamaks”. *Nuclear Fusion* **57** (12) (Oct. 2017), p. 126038. DOI: `10.1088/1741-4326/aa8876`.

[11] A. H. Boozer. “Theory of tokamak disruptions”. *Physics of Plasmas* **19** (5) (2012), p. 058101. DOI: `10.1063/1.3703327`.

[12] H. Dreicer. “Electron and ion runaway in a fully ionized gas. I”. *Physical Review* **115** (1959), p. 238. DOI: `10.1103/PhysRev.115.238`.

[13] B. N. Breizman, P. Aleynikov, E. M. Hollmann, and M. Lehnen. “Physics of runaway electrons in tokamaks”. *Nuclear Fusion* **59** (8) (June 2019), p. 083001. DOI: `10.1088/1741-4326/ab1822`.

[14] M. N. Rosenbluth and S. V. Putvinski. “Theory for avalanche of runaway electrons in tokamaks”. *Nuclear Fusion* **37** (10) (1997), p. 1355. DOI: `10.1088/0029-5515/37/10/I03`.

[15] M. Lehnen et al. “Disruptions in ITER and strategies for their control and mitigation”. *Journal of Nuclear Materials* **463** (2015), p. 39. DOI: `10.1016/j.jnucmat.2014.10.075`.

[16] C. Rea, K. J. Montes, A. Pau, R. S. Granetz, and O. Sauter. “Progress Toward Interpretable Machine Learning–Based Disruption Predictors Across Tokamaks”. *Fusion Science and Technology* **76** (8) (2020), pp. 912–924. DOI: `10.1080/15361055.2020.1798589`.

[17] O. Vallhagen. “Disruption mitigation in tokamaks with shattered pellet injection”. Master’s thesis. Chalmers University of Technology, 2021. URL: `https://hdl.handle.net/20.500.12380/302296`.

[18] L. Hesslow, O. Embréus, O. Vallhagen, and T. Fülöp. “Influence of massive material injection on avalanche runaway generation during tokamak disruptions”. *Nuclear Fusion* **59** (8) (2019), p. 084004. DOI: `10.1088/1741-4326/ab26c2`.

[19] K. Finken, S. Abdullaev, M. Jakubowski, R. Jaspers, M. Lehnen, and O. Zimmermann. “Losses of runaway electrons during ergodization”. *Nuclear Fusion* **46** (4) (Mar. 2006), S139–S144. DOI: `10.1088/0029-5515/46/4/s04`.

[20] V. Riccardo, G. Arnoux, P. Cahyna, T. C. Hender, A. Huber, S. Jachmich, V. Kiptily, R. Koslowski, L. Krlin, M. Lehnen, A. Loarte, E. Nardon, R. Paprok, and D. T. and. “JET disruption studies in support of ITER”. *Plasma Physics and Controlled Fusion* **52** (12) (Nov. 2010), p. 124018. DOI: `10.1088/0741-3335/52/12/124018`.

[21] G. Papp, M. Drevlak, G. I. Pokol, and T. Fülöp. “Energetic electron transport in the presence of magnetic perturbations in magnetically confined plasmas”. *Journal of Plasma Physics* **81** (5) (2015), p. 475810503. DOI: `10.1017/S0022377815000537`.

[22] A. H. Boozer. “Two beneficial non-axisymmetric perturbations to tokamaks”. *Plasma Physics and Controlled Fusion* **53** (8) (May 2011), p. 084002. DOI: `10.1088/0741-3335/53/8/084002`.

[23] A. J. Creely et al. “Overview of the SPARC tokamak”. *Journal of Plasma Physics* **86** (5) (2020), p. 865860502. DOI: `10.1017/S0022377820001257`.

[24] C. Paz-Soldan et al. “A novel path to runaway electron mitigation via deuterium injection and current-driven MHD instability”. *Nuclear Fusion* **61** (11) (Oct. 2021), p. 116058. DOI: `10.1088/1741-4326/ac2a69`.

[25] E. Nardon, D. Hu, M. Hoelzl, D. Bonfiglio, and the JOREK team. “Fast plasma dilution in ITER with pure deuterium shattered pellet injection”. *Nuclear Fusion* **60** (12) (Oct. 2020), p. 126040. DOI: `10.1088/1741-4326/abb749`.

[26] J. D. Jackson. *Classical electrodynamics*. 3rd ed. John Wiley & Sons, 2012.

[27] J. Killeen and K. D. Marx. “Solution of the Fokker–Planck equation for a mirror-confined plasma”. *Methods in Computational Physics* (9) (Jan. 1970), pp. 421–89.

[28] K. D. Marx. “Effects of Spatial Variations on Collisional Losses in a Mirror-Confined Plasma”. *The Physics of Fluids* **13** (5) (1970), pp. 1355–1371. DOI: `10.1063/1.1693069`.

[29] J. Killeen, G. D. Kerbel, M. G. McCoy, and A. A. Mirin. *Computational methods for kinetic models of magnetically confined plasmas*. Springer Science & Business Media, 1986.

[30] R. J. Goldston. “Fast ion diagnostic experiment on ATC: radially resolved measurements of q, Z_{eff}, $T_{i\parallel}$ and $T_{i\nparallel}$”. PhD thesis. Princeton University, 1977. URL: `https://www.proquest.com/dissertations-theses/fast-ion-diagnostic-experiment-on-atc-radially/docview/302848259/se-2?accountid=10041`.

[31] *The CQL3D code.* IAEA TCM on Advances in Simulation and Modelling of Thermonuclear Plasmas. Montreal, 1992, pp. 489–526. URL: `http://www.compxco.com/cql3d_manual.pdf`.

[32] J. Decker and Y. Peysson. *DKE: a fast numerical solver for the 3D drift kinetic equation.* Tech. rep. no. EUR-CEA-FC-1736, 2004. URL: `https://spcsrv18.epfl.ch/luke/LaTeX/Project_DKE/Doc/NoticeDKE.pdf`.

[33] J. P. Freidberg. *Plasma physics and fusion energy.* Cambridge University Press, 2008.

[34] J. Liouville. “Sur la Theorie de la Variation des constantes arbitraires”. *Journal de mathématiques pures et appliquées* **3** (1838), pp. 342–349.

[35] L. P. Pitaevskii, E. M. Lifshitz, and J. B. Sykes. *Course of Theoretical Physics: Physical Kinetics.* Elsevier, 1981.

[36] S. T. Beliaev and G. I. Budker. *Soviet Physics Doklady* **1** (1956), p. 218.

[37] B. J. Braams and C. F. F. Karney. “Differential form of the collision integral for a relativistic plasma”. *Physical Review Letters* **59** (16) (Oct. 1987), pp. 1817–1820. DOI: `10.1103/PhysRevLett.59.1817`.

[38] J. Wesson and D. J. Campbell. *Tokamaks.* 4th ed. Vol. 149. Oxford University Press, 2011.

[39] M. N. Rosenbluth, W. M. MacDonald, and D. L. Judd. “Fokker-Planck Equation for an Inverse-Square Force”. *Physical Review* **107** (1) (July 1957), pp. 1–6. DOI: `10.1103/PhysRev.107.1`.

[40] O. J. Pike and S. J. Rose. “Dynamical friction in a relativistic plasma”. *Physical Review E* **89** (5) (May 2014), p. 053107. DOI: `10.1103/PhysRevE.89.053107`.

[41] C. J. McDevitt and X.-Z. Tang. “Runaway electron generation in axisymmetric tokamak geometry”. *Europhysics Letters* **127** (4) (Sept. 2019), p. 45001. DOI: `10.1209/0295-5075/127/45001`.

[42] B. J. Braams and C. F. F. Karney. “Conductivity of a relativistic plasma”. *Physics of Fluids B: Plasma Physics* **1** (7) (1989), pp. 1355–1368. DOI: `10.1063/1.858966`.

[43] C. T. R. Wilson. “The electric field of a thundercloud and some of its effects”. *Proceedings of the Physical Society of London* **37** (1) (1924), p. 32D. DOI: `10.1088/1478-7814/37/1/314`.

[44] A. V. Gurevich and K. P. Zybin. “Runaway breakdown and electric discharges in thunderstorms”. *Physics-Uspekhi* **44** (11) (Nov. 2001), pp. 1119–1140. DOI: `10.1070/pu2001v044n11abeh000939`.

[45] M. Alaoui, G. D. Holman, J. C. Allred, and R. T. Eufrasio. “Role of Suprathermal Runaway Electrons Returning to the Acceleration Region in Solar Flares”. *The Astrophysical Journal* **917** (2) (Aug. 2021), p. 74. DOI: `10.3847/1538-4357/ac0820`.

[46] P. C. de Vries, Y. Gribov, R. Martin-Solis, A. B. Mineev, J. Sinha, A. C. C. Sips, V. Kiptily, and A. Loarte. “Analysis of runaway electron discharge formation during Joint European Torus plasma start-up”. *Plasma Physics and Controlled Fusion* **62** (12) (Nov. 2020), p. 125014. DOI: `10.1088/1361-6587/abbe34`.

[47] S. Putvinski, P. Barabaschi, N. Fujisawa, N. Putvinskaya, M. N. Rosenbluth, and J. Wesley. “Halo current, runaway electrons and disruption mitigation in ITER”. *Plasma Physics and Controlled Fusion* **39** (12B) (Dec. 1997), B157–B171. DOI: `10.1088/0741-3335/39/12b/013`.

[48] H. Dreicer. “Electron and ion runaway in a fully ionized gas. II”. *Physical Review* **117** (1960), p. 329. DOI: `10.1103/PhysRev.117.329`.

[49] J. W. Connor and R. J. Hastie. “Relativistic limitations on runaway electrons”. *Nuclear Fusion* **15** (3) (1975), p. 415. DOI: `10.1088/0029-5515/15/3/007`.

[50] J. R. Martìn-Solìs, R. Sánchez, and B. Esposito. “Experimental observation of increased threshold electric field for runaway generation due to synchrotron radiation losses in the FTU tokamak”. *Physical Review Letters* **105** (2010), p. 185002. DOI: `10.1103/PhysRevLett.105.185002`.

[51] R. S. Granetz, B. Esposito, J. H. Kim, R. Koslowski, M. Lehnen, J. R. Martin-Solis, C. Paz-Soldan, T. Rhee, J. C. Wesley, and L. Zeng. "An ITPA joint experiment to study runaway electron generation and suppression". *Physics of Plasmas* **21** (7) (2014), p. 072506. DOI: `10.1063/1.4886802`.

[52] C. Paz-Soldan, N. W. Eidietis, R. Granetz, E. M. Hollmann, R. A. Moyer, J. C. Wesley, J. Zhang, M. E. Austin, N. A. Crocker, A. Wingen, and Y. Zhu. "Growth and decay of runaway electrons above the critical electric field under quiescent conditions". *Physics of Plasmas* **21** (2) (2014), p. 022514. DOI: `10.1063/1.4866912`.

[53] Z. Popovic, B. Esposito, J. R. Martín-Solís, W. Bin, P. Buratti, D. Carnevale, F. Causa, M. Gospodarczyk, D. Marocco, G. Ramogida, and M. Riva. "On the measurement of the threshold electric field for runaway electron generation in the Frascati Tokamak Upgrade". *Physics of Plasmas* **23** (12) (2016), p. 122501. DOI: `10.1063/1.4968839`.

[54] A. Stahl, E. Hirvijoki, J. Decker, O. Embréus, and T. Fülöp. "Effective critical electric field for runaway-electron generation". *Physical Review Letters* **114** (2015), p. 115002. DOI: `10.1103/PhysRevLett.114.115002`.

[55] P. Aleynikov and B. N. Breizman. "Theory of Two Threshold Fields for Relativistic Runaway Electrons". *Physical Review Letters* **114** (15) (Apr. 2015), p. 155001. DOI: `10.1103/PhysRevLett.114.155001`.

[56] L. Hesslow, O. Embréus, G. J. Wilkie, G. Papp, and T. Fülöp. "Effect of partially ionized impurities and radiation on the effective critical electric field for runaway generation". *Plasma Physics and Controlled Fusion* **60** (7) (2018), p. 074010. DOI: `https://doi.org/10.1103/PhysRevLett.118.255001`.

[57] T. C. Hender et al. "Chapter 3: MHD stability, operational limits and disruptions". *Nuclear Fusion* **47** (6) (2007), S128. DOI: `10.1088/0029-5515/47/6/S03`.

[58] S. Putvinski, N. Fujisawa, D. Post, N. Putvinskaya, M. N. Rosenbluth, and J. Wesley. "Impurity fueling to terminate Tokamak discharges". *Journal of Nuclear Materials* **241-243** (1997), pp. 316–321. DOI: `10.1016/S0022-3115(97)80056-6`.

[59] J. R. Martìn-Solìs, A. Loarte, and M. Lehnen. “Formation and termination of runaway beams in ITER disruptions”. *Nuclear Fusion* **57** (6) (Apr. 2017), p. 066025. DOI: `10.1088/1741-4326/aa6939`.

[60] H. Smith, P. Helander, L.-G. Eriksson, D. Anderson, M. Lisak, and F. Andersson. “Runaway electrons and the evolution of the plasma current in tokamak disruptions”. *Physics of Plasmas* **13** (10) (2006), p. 102502. DOI: `10.1063/1.2358110`.

[61] T. Fehér, H. M. Smith, T. Fülöp, and K. Gál. “Simulation of runaway electron generation during plasma shutdown by impurity injection in ITER”. *Plasma Physics and Controlled Fusion* **53** (3) (Feb. 2011), p. 035014. DOI: `10.1088/0741-3335/53/3/035014`.

[62] G. Papp, T. Fülöp, T. Fehér, P. C. de Vries, V. Riccardo, C. Reux, M. Lehnen, V. Kiptily, V. V. Plyusnin, and B. A. and. “The effect of ITER-like wall on runaway electron generation in JET”. *Nuclear Fusion* **53** (12) (Nov. 2013), p. 123017. DOI: `10.1088/0029-5515/53/12/123017`.

[63] P. Aleynikov and B. N. Breizman. “Generation of runaway electrons during the thermal quench in tokamaks”. *Nuclear Fusion* **57** (4) (2017), p. 046009. DOI: `10.1088/1741-4326/aa5895`.

[64] L. Spitzer and R. Härm. “Transport Phenomena in a Completely Ionized Gas”. *Physical Review* **89** (5) (Mar. 1953), pp. 977–981. DOI: `10.1103/PhysRev.89.977`.

[65] A. Redl, C. Angioni, E. Belli, and O. Sauter. “A new set of analytical formulae for the computation of the bootstrap current and the neoclassical conductivity in tokamaks”. *Physics of Plasmas* **28** (2) (2021), p. 022502. DOI: `10.1063/5.0012664`.

[66] D. G. Whyte, T. C. Jernigan, and S. L. Luckhardt. *Energy balance, radiation and stability during rapid plasma termination via impurity pellet injections on DIII-D*. Conference GA-A22639. US-DOE Office of Energy Research, June 1997. URL: `https://www.osti.gov/biblio/513523`.

[67] L. Hesslow, O. Embréus, A. Stahl, T. C. DuBois, G. Papp, S. L. Newton, and T. Fülöp. “Effect of partially screened nuclei on fast-electron dynamics”. *Physical Review Letters* **118** (2017), p. 255001. DOI: `10.1103/PhysRevLett.118.255001`.

[68] N. A. Garland, H.-K. Chung, C. J. Fontes, M. C. Zammit, J. Colgan, T. Elder, C. J. McDevitt, T. M. Wildey, and X.-Z. Tang. “Impact of a minority relativistic electron tail interacting with a thermal plasma containing high-atomic-number impurities”. *Physics of Plasmas* **27** (4) (2020), p. 040702. DOI: `10.1063/5.0003638`.

[69] S. C. Chiu, M. N. Rosenbluth, R. W. Harvey, and V. S. Chan. “Fokker-Planck simulations mylb of knock-on electron runaway avalanche and bursts in tokamaks”. *Nuclear Fusion* **38** (11) (1998), p. 1711. DOI: `10.1088/0029-5515/38/11/309`.

[70] R. W. Harvey, V. S. Chan, S. C. Chiu, T. E. Evans, M. N. Rosenbluth, and D. G. Whyte. “Runaway electron production in DIII-D killer pellet experiments, calculated with the CQL3D/KPRAD model”. *Physics of Plasmas* **7** (11) (2000), p. 4590. DOI: `10.1063/1.1312816`.

[71] P. Helander, H. Smith, T. Fülöp, and L.-G. Eriksson. “Electron kinetics in a cooling plasma”. *Physics of Plasmas* **11** (12) (2004), pp. 5704–5709. DOI: `10.1063/1.1812759`.

[72] H. Smith, P. Helander, L.-G. Eriksson, and T. Fülöp. “Runaway electron generation in a cooling plasma”. *Physics of Plasmas* **12** (12) (2005), p. 122505. DOI: `10.1063/1.2148966`.

[73] H. M. Smith and E. Verwichte. “Hot tail runaway electron generation in tokamak disruptions”. *Physics of Plasmas* **15** (7) (2008), p. 072502. DOI: `10.1063/1.2949692`.

[74] K. Insulander Björk, G. Papp, O. Embreus, L. Hesslow, T. Fülöp, O. Vallhagen, A. Lier, G. Pautasso, A. Bock, the ASDEX Upgrade Team, and the EUROfusion MST1 Team. “Kinetic modelling of runaway electron generation in argon-induced disruptions in ASDEX Upgrade”. *Journal of Plasma Physics* **86** (4) (2020), p. 855860401. DOI: `10.1017/S0022377820000793`.

[75] I. U. A. Sokolov. ““Multiplication” of accelerated electrons in a tokamak”. *JETP Letters* **29** (1979), p. 218. URL: `http://jetpletters.ru/ps/1450/article_22066.shtml`.

[76] R. Jayakumar, H. H. Fleischmann, and S. J. Zweben. “Collisional avalanche exponentiation of runaway electrons in electrified plasmas”. *Physics Letters A* **172** (6) (1993), pp. 447–451. DOI: `10.1016/0375-9601(93)90237-T`.

[77] O. Embréus, A. Stahl, and T. Fülöp. "On the relativistic large-angle electron collision operator for runaway avalanches in plasmas". *Journal of Plasma Physics* **84** (1) (2018), p. 905840102. DOI: `10.1017/S002237781700099X`.

[78] T. Fülöp, G. Pokol, P. Helander, and M. Lisak. "Destabilization of magnetosonic-whistler waves by a relativistic runaway beam". *Physics of Plasmas* **13** (6) (2006), p. 062506. DOI: `10.1063/1.2208327`.

[79] M. Bakhtiari, G. J. Kramer, M. Takechi, H. Tamai, Y. Miura, Y. Kusama, and Y. Kamada. "Role of Bremsstrahlung Radiation in Limiting the Energy of Runaway Electrons in Tokamaks". *Physical Review Letters* **94** (21) (June 2005), p. 215003. DOI: `10.1103/PhysRevLett.94.215003`.

[80] O. Embréus, A. Stahl, and T. Fülöp. "Effect of bremsstrahlung radiation emission on fast electrons in plasmas". *New Journal of Physics* **18** (9) (2016), p. 093023. DOI: `10.1088/1367-2630/18/9/093023`.

[81] G. Bekefi. *Radiation processes in plasmas*. New York: John Wiley, 1966.

[82] E. Hirvijoki, I. Pusztai, J. Decker, O. Embréus, A. Stahl, and T. Fülöp. "Radiation reaction induced non-monotonic features in runaway electron distributions". *Journal of Plasma Physics* **81** (5) (2015), p. 475810502. DOI: `10.1017/S0022377815000513`.

[83] J. Decker, E. Hirvijoki, O. Embréus, Y. Peysson, A. Stahl, I. Pusztai, and T. Fülöp. "Numerical characterization of bump formation in the runaway electron tail". *Plasma Physics and Controlled Fusion* **58** (2) (2016), p. 025016. DOI: `10.1088/0741-3335/58/2/025016`.

[84] A. B. Rechester and M. N. Rosenbluth. "Electron Heat Transport in a Tokamak with Destroyed Magnetic Surfaces". *Physical Review Letters* **40** (1) (Jan. 1978), pp. 38–41. DOI: `10.1103/PhysRevLett.40.38`.

[85] B. Esposito, R. M. Solis, P. van Belle, O. N. Jarvis, F. B. Marcus, G. Sadler, R. Sanchez, B. Fischer, P. Froissard, J. M. Adams, E. Cecil, and N. Watkins. "Runaway electron measurements in the JET tokamak". *Plasma Physics and Controlled Fusion* **38** (12)

(Dec. 1996), pp. 2035–2049. DOI: `10.1088/0741-3335/38/12/001`.

[86] T. Hauff and F. Jenko. “Runaway electron transport via tokamak microturbulence”. *Physics of Plasmas* **16** (10) (2009), p. 102308. DOI: `10.1063/1.3243494`.

[87] K. Särkimäki, O. Embreus, E. Nardon, T. Fülöp, and JET contributors. “Assessing energy dependence of the transport of relativistic electrons in perturbed magnetic fields with orbit-following simulations”. *Nuclear Fusion* **60** (12) (Nov. 2020), p. 126050. DOI: `10.1088/1741-4326/abb9e9`.

[88] P. Svensson, O. Embreus, S. L. Newton, K. Särkimäki, O. Vallhagen, and T. Fülöp. “Effects of magnetic perturbations and radiation on the runaway avalanche”. *Journal of Plasma Physics* **87** (2) (2021), p. 905870207. DOI: `10.1017/S0022377820001592`.

[89] B. N. Breizman. “Marginal stability model for the decay of runaway electron current”. *Nuclear Fusion* **54** (7) (Apr. 2014), p. 072002. DOI: `10.1088/0029-5515/54/7/072002`.

[90] V. Bandaru, M. Hoelzl, C. Reux, O. Ficker, S. Silburn, M. Lehnen, N. Eidietis, and J. Team. “Magnetohydrodynamic simulations of runaway electron beam termination in JET”. *Plasma Physics and Controlled Fusion* **63** (3) (Jan. 2021), p. 035024. DOI: `10.1088/1361-6587/abdbcf`.

[91] C. Reux, C. Paz-Soldan, P. Aleynikov, V. Bandaru, O. Ficker, S. Silburn, M. Hoelzl, S. Jachmich, N. Eidietis, M. Lehnen, S. Sridhar, and JET contributors. “Demonstration of Safe Termination of Megaampere Relativistic Electron Beams in Tokamaks”. *Physical Review Letters* **126** (17) (Apr. 2021), p. 175001. DOI: `10.1103/PhysRevLett.126.175001`.

[92] H. W. Koch and J. W. Motz. “Bremsstrahlung cross-section formulas and related data”. *Reviews of Modern Physics* **31** (4) (1959), p. 920. DOI: `10.1103/RevModPhys.31.920`.

[93] D. C. Pace, C. M. Cooper, D. Taussig, N. W. Eidietis, E. M. Hollmann, V. Riso, M. A. Van Zeeland, and M. Watkins. “Gamma ray imager on the DIII-D tokamak”. *Review of Scientific Instruments* **87** (4) (2016), p. 043507. DOI: `10.1063/1.4945566`.

[94] C. M. Cooper, D. C. Pace, C. Paz-Soldan, N. Commaux, N. W. Eidietis, E. M. Hollmann, and D. Shiraki. “Applying the new gamma ray imager diagnostic to measurements of runaway electron Bremsstrahlung radiation in the DIII-D Tokamak (invited)”. *Review of Scientific Instruments* **87** (11) (2016), 11E602. DOI: `10.1063/1.4961288`.

[95] A. E. Shevelev, E. M. Khilkevitch, V. G. Kiptily, I. N. Chugunov, D. B. Gin, D. N. Doinikov, V. O. Naidenov, A. E. Litvinov, I. A. Polunovskii, and J.-E. Contributors. “Reconstruction of distribution functions of fast ions and runaway electrons in fusion plasmas using gamma-ray spectrometry with applications to ITER”. *Nuclear Fusion* **53** (12) (2013), p. 123004. DOI: `10.1088/0029-5515/53/12/123004`.

[96] M. Nocente et al. “MeV range particle physics studies in tokamak plasmas using gamma-ray spectroscopy”. *Plasma Physics and Controlled Fusion* **62** (1) (Nov. 2019), p. 014015. DOI: `10.1088/1361-6587/ab4f32`.

[97] A. Dal Molin, L. Fumagalli, M. Nocente, D. Rigamonti, M. Tardocchi, L. Giacomelli, E. Panontin, A. Lvovskiy, C. Paz-Soldan, N. W. Edietis, and G. Gorini. “Novel compact hard x-ray spectrometer with MCps counting rate capabilities for runaway electron measurements on DIII-D”. *Review of Scientific Instruments* **92** (4) (2021), p. 043517. DOI: `10.1063/5.0043762`.

[98] R. Jaspers, K. H. Finken, G. Mank, F. Hoenen, J. A. Boedo, N. J. Lopes Cardozo, and F. C. Schüller. “Experimental investigation of runaway electron generation in TEXTOR”. *Nuclear Fusion* **33** (12) (1993), p. 1775. DOI: `10.1088/0029-5515/33/12/I02`.

[99] Ž. Popović, E. M. Hollmann, D. del-Castillo-Negrete, I. Bykov, R. A. Moyer, J. L. Herfindal, D. Shiraki, N. W. Eidietis, C. Paz-Soldan, and A. Lvovskiy. “Polarized imaging of visible synchrotron emission from runaway electron plateaus in DIII-D”. *Physics of Plasmas* **28** (8) (2021), p. 082510. DOI: `10.1063/5.0058927`.

[100] R. E. Jaspers. “Relativistic runaway electrons in tokamak plasmas”. PhD thesis. 1995. URL: `http://inis.iaea.org/search/search.aspx?orig_q=RN:27012481`.

[101] I. M. Pankratov. "Analysis of the synchrotron radiation emitted by runaway electrons". *Plasma Physics Reports* **22** (6) (1996), p. 535.

[102] R. Jaspers, N. J. Lopes Cardozo, A. J. H. Donné, H. L. M. Widdershoven, and K. H. Finken. "A synchrotron radiation diagnostic to observe relativistic runaway electrons in a tokamak plasma". *Review of Scientific Instruments* **72** (1) (2001), p. 466. DOI: `10.1063/1.1318245`.

[103] C. Liu, H. Qin, E. Hirvijoki, Y. Wang, and J. Liu. "Conservative magnetic moment of runaway electrons and collisionless pitch-angle scattering". *Nuclear Fusion* **58** (10) (2018), p. 106018. DOI: `10.1088/1741-4326/aad2a5`.

[104] A. S. Jacobsen, L. Stagner, M. Salewski, B. Geiger, W. W. Heidbrink, S. B. Korsholm, F. Leipold, S. K. Nielsen, J. Rasmussen, M. Stejner, H. Thomsen, M. Weiland, and the ASDEX Upgrade team. "Inversion methods for fast-ion velocity-space tomography in fusion plasmas". *Plasma Physics and Controlled Fusion* **58** (4) (2016), p. 045016. DOI: `10.1088/0741-3335/58/4/045016`.

[105] M. Salewski, B. Geiger, A. S. Jacobsen, P. C. Hansen, W. W. Heidbrink, S. B. Korsholm, F. Leipold, J. Madsen, D. Moseev, S. K. Nielsen, M. Nocente, T. Odstrčil, J. Rasmussen, L. Stagner, M. Stejner, M. Weiland, and the ASDEX Upgrade team. "High-definition velocity-space tomography of fast-ion dynamics". *Nuclear Fusion* **56** (10) (2016), p. 106024. DOI: `10.1088/0029-5515/56/10/106024`.

[106] K. H. Finken, J. G. Watkins, D. Rusbüldt, W. J. Corbett, K. H. Dippel, D. M. Goebel, and R. A. Moyer. "Observation of infrared synchrotron radiation from tokamak runaway electrons in TEXTOR". *Nuclear Fusion* **30** (5) (1990), p. 859. DOI: `10.1088/0029-5515/30/5/005`.

[107] R. J. Zhou, I. M. Pankratov, L. Q. Hu, M. Xu, and J. H. Yang. "Synchrotron radiation spectra and synchrotron radiation spot shape of runaway electrons in Experimental Advanced Superconducting Tokamak". *Physics of Plasmas* **21** (6) (2014), p. 063302. DOI: `10.1063/1.4881469`.

[108] M. Landreman, A. Stahl, and T. Fülöp. “Numerical calculation of the runaway electron distribution function and associated synchrotron emission”. *Computer Physics Communications* **185** (3) (2014), p. 847. DOI: `10.1016/j.cpc.2013.12.004`.

[109] A. Stahl, O. Embréus, G. Papp, M. Landreman, and T. Fülöp. “Kinetic modelling of runaway electrons in dynamic scenarios”. *Nuclear Fusion* **56** (11) (2016), p. 112009. DOI: `10.1088/0029-5515/56/11/112009`.

[110] J. Korger, T. Kolb, P. Banzer, A. Aiello, C. Wittmann, C. Marquardt, and G. Leuchs. “The polarization properties of a tilted polarizer”. *Optics Express* **21** (22) (Nov. 2013), pp. 27032–27042. DOI: `10.1364/OE.21.027032`.

[111] O. Vallhagen, O. Embreus, I. Pusztai, L. Hesslow, and T. Fülöp. “Runaway dynamics in the DT phase of ITER operations in the presence of massive material injection”. *Journal of Plasma Physics* **86** (4) (2020), p. 475860401. DOI: `10.1017/S0022377820000859`.

[112] C. Paz-Soldan, C. M. Cooper, P. Aleynikov, D. C. Pace, N. W. Eidietis, D. P. Brennan, R. S. Granetz, E. M. Hollmann, C. Liu, A. Lvovskiy, R. A. Moyer, and D. Shiraki. “Spatiotemporal evolution of runaway electron momentum distributions in tokamaks”. *Physical Review Letters* **118** (2017), p. 255002. DOI: `10.1103/PhysRevLett.118.255002`.

[113] K. Insulander Björk, O. Vallhagen, G. Papp, C. Reux, O. Embreus, E. Rachlew, T. Fülöp, the ASDEX Upgrade team, J. contributors, and the EUROfusion MST1 team. “Modelling of runaway electron dynamics during argon-induced disruptions in ASDEX Upgrade and JET”. *Plasma Physics and Controlled Fusion* **63** (8) (2021), p. 085021. DOI: `10.1088/1361-6587/ac07b5`.

[114] O. Linder, E. Fable, F. Jenko, G. Papp, G. Pautasso, and and. “Self-consistent modeling of runaway electron generation in massive gas injection scenarios in ASDEX Upgrade”. *Nuclear Fusion* **60** (9) (Aug. 2020), p. 096031. DOI: `10.1088/1741-4326/ab9dcf`.

[115] O. Linder, G. Papp, E. Fable, F. Jenko, and G. Pautasso. “Electron runaway in ASDEX Upgrade experiments of varying core temperature”. *Journal of Plasma Physics* **87** (3) (2021), p. 905870301. DOI: `10.1017/S0022377821000416`.

[116] A. Stahl, M. Landreman, O. Embréus, and T. Fülöp. “NORSE: A solver for the relativistic non-linear Fokker-Planck equation for electrons in a homogeneous plasma”. *Computer Physics Communications* **212** (2017), pp. 269–279. DOI: `10.1016/j.cpc.2016.10.024`.

[117] D. Daniel, W. T. Taitano, and L. Chacón. “A fully implicit, scalable, conservative nonlinear relativistic Fokker–Planck 0D-2P solver for runaway electrons”. *Computer Physics Communications* **254** (2020), p. 107361. URL: `https://doi.org/10.1016/j.cpc.2020.107361`.

[118] V. Bandaru, M. Hoelzl, F. J. Artola, G. Papp, and G. T. A. Huijsmans. “Simulating the nonlinear interaction of relativistic electrons and tokamak plasma instabilities: Implementation and validation of a fluid model”. *Physical Review E* **99** (6) (June 2019), p. 063317. URL: `https://link.aps.org/doi/10.1103/PhysRevE.99.063317`. DOI: `10.1103/PhysRevE.99.063317`.

[119] C. Zhao, C. Liu, S. C. Jardin, and N. M. Ferraro. “Simulation of MHD instabilities with fluid runaway electron model in M3D-C 1”. *Nuclear Fusion* **60** (12) (Oct. 2020), p. 126017. DOI: `10.1088/1741-4326/ab96f4`.

[120] J. R. Martìn-Solìs, J. A. Mier, M. Lehnen, and A. Loarte. “Formation and termination of runaway beams during vertical displacement events in ITER disruptions”. *28th IAEA Fusion Energy Conference*. TH/P7-1102. May 14, 2021. URL: `https://conferences.iaea.org/event/214/contributions/17686/`.

[121] D. I. Kiramov and B. N. Breizman. “Model of vertical plasma motion during the current quench”. *Physics of Plasmas* **24** (10) (2017), p. 100702. DOI: `10.1063/1.4993071`.

[122] G. Pautasso et al. “Disruption mitigation by injection of small quantities of noble gas in ASDEX Upgrade”. *Plasma Physics and Controlled Fusion* **59** (1) (Nov. 2016), p. 014046. DOI: `10.1088/0741-3335/59/1/014046`.

[123] H.-T. Kim, A. C. C. Sips, and P. C. de Vries and. “Plasma burn-through simulations using the DYON code and predictions for ITER”. *Plasma Physics and Controlled Fusion* **55** (12) (Nov. 2013), p. 124032. DOI: `10.1088/0741-3335/55/12/124032`.

[124] H.-T. Kim, A. Mineev, D. Ricci, J. Lee, and Y.-S. Na. “Benchmarking of codes for plasma burn-through in tokamaks”. *Nuclear Fusion* **60** (12) (Sept. 2020), p. 126049. DOI: `10.1088/1741-4326/abb95c`.

[125] P. de Vries and Y. Gribov. “ITER breakdown and plasma initiation revisited”. *Nuclear Fusion* **59** (9) (Aug. 2019), p. 096043. DOI: `10.1088/1741-4326/ab2ef4`.